Numerical Simulation of Light Scattering of a Pendent Droplet by Statistic Vectorial Complex Ray Model

Ruiping Yang

Normandie Université

THESIS

For the degree of Doctor of Philosophy

Specialty: Physics

Prepared at the University of Rouen Normandy

Title of the thesis

Numerical Simulation of Light Scattering of a Pendent Droplet by Statistic Vectorial Complex Ray Model

Presented and defended by

Ruiping YANG

Thesis defended publicly on 12 December 2019 before the jury composed of

Fabrice LEMOINE	Professor at ENSEM LEMTA CNRS UMR 7563, University of Lorraine	Reviewer
Fabrice ONOFRI	Director of research IUSTI CNRS UMR 7343, Aix-Marseille University	Reviewer
Loïc MÉÈS	Research fellow at LMFA CNRS UMR 5509, Ecole Centrale de Lyon	Examiner
François-Xavier DEMOULIN	Professor at University of Rouen Normandie, CORIA-UMR 6614, Rouen	Examiner
Claude ROZÉ	Professor at University of Rouen Normandie, CORIA-UMR 6614, Rouen	Co-supervisor
Kuan Fang REN	Professor at University of Rouen Normandie, CORIA-UMR 6614, Rouen	Supervisor

Thesis directed by Kuan Fang REN and Claude ROZÉ, CORIA-UMR 6614

UNIVERSITÉ DE ROUEN NORMANDIE

ED PSIME

coria UMR 6614

Normandie Université

THÈSE

Pour obtenir le diplôme de doctorat

Spécialité : Physique

Préparée au sein de l'université de Rouen Normandie

Titre de la thèse

Simulation Numérique de Diffusion de la Lumière par une Goutte Pendante par Tracé de Rayons Vectoriels Complexes Statistique

Présentée et soutenue par

Ruiping YANG

Thèse soutenue publiquement le 12 Décembre, 2019
devant le jury composé de

Fabrice LEMOINE	Professeur à ENSEM LEMTA CNRS UMR 7563, Université de Lorraine	Rapporteur
Fabrice ONOFRI	Directeur de recherche IUSTI CNRS UMR 7343, Aix-Marseille Université	Rapporteur
Loïc MÉÈS	Chargé de recherche au LMFA CNRS UMR 5509, Ecole Centrale de Lyon	Examinateur
François-Xavier DEMOULIN	Professeur à l'Université de Rouen Normandie, CORIA-UMR 6614	Examinateur
Claude ROZÉ	Professeur à l'Université de Rouen Normandie, CORIA-UMR 6614	Codirect. de thèse
Kuan Fang REN	Professeur à l'Université de Rouen Normandie, CORIA-UMR 6614	Directeur de thèse

Thesis directed by Kuan Fang REN and Claude ROZÉ, CORIA-UMR 6614

UNIVERSITÉ DE ROUEN NORMANDIE

ED PSIME

coria UMR 6614

Acknowledgements

The thesis received funding from the China Scholarship Council. This work was also partially supported by the CRIANN (Centre Régional Informatique et d'Applications Numériques de Normandie).

I have to thank many people who have offered me assistance and encouragement.

First and foremost, I would like to express my heartfelt gratitude to my supervisor, Professor Kuan Fang REN, who has spent much time to reading every version of the drafts of my thesis and provided me with invaluable suggestions and excellent guidance. He taught me a effective methodology to carry out scientific research, as an example physics. It starts with having a good knowledge of the fundamental physics principles and listing systematically the research ideas. Then, it is crucial to design and debug the program according to the physical principles. After that, it is necessary to analyze the obtained simulation results and explain whether the simulation results are reasonable or not based on the physics theory. At last, it is essential to present the research results in a suitable form. With his illuminating instruction, I can achieve the initial simulation results of my program and initially finish the writing of this thesis. The experience I obtained will be of great importance to my future work and study.

Secondly, I owe my particular thanks to my co-supervisor **Professor Claude ROZÉ** for his code on the Statistic Vectorial Complex Ray Model (SVCRM) which has permitted the calculation of the scattering intensity and his software for image processing which extracts the profile of a droplet from the experimental recoded images. It is based on his code of SVCRM I could achieve the work of my thesis. His professional knowledge on SVCRM provides me with theoretical guidance to deal with the light scattering of a pendent droplet in three dimensions. He also introduced some tools that help me manage my program in order. In addition, his every recognition and encouragement gave me more confidence to continue the research of SVCRM.

Thirdly, thanks go particularly to **Driss ABDEDDAIM**, student at EsiTech, for the droplet images and the scattering patterns he recorded during his internship at CORIA in 2016 and **Romain ALLEAUME**, student at Rouen University, for the experimental results (droplet images and their scattering patterns) he recorded during his internship at CORIA in 2017. A special thanks to **Saïd IDLAHCEN**, engineer of research in CORIA, for his technical support and help in the realization of the experiment on the generation of the droplet, the design of optical system, the acquisition of the images

and the scattering patterns.

Thanks are also due to the members of the jury, Professor Fabrice LEMOINE, Dr. Fabrice ONOFRI, Dr. Loïc MÉÈS and Professor François-Xavier DEMOULIN for their patience in reading this manuscript and evaluating it.

Finally, I would like to thank my family and boyfriend for their accompany, encouragement and support. They share with me my worries, depression, and happiness, which make me feel that I am not alone.

Contents

List of Symbols and Abbreviations

Greek Symbols

α	:	size parameter of particle
ρ	:	curvature radius of particle surface
θ_i	:	incident angle
θ_r	:	reflection angle
θ_t	:	refraction angle
θ_B	:	Brewster's angle
θ_C	:	critical angle
κ	:	curvature of a wave front or of particle surface
δ	:	rotation angle of a general matrix and a diagonal matrix
ϕ	:	azimuthal angle
θ	:	polar angle
ϕ_d	:	detection azimuthal angle relative to xz plane
θ_d	:	detection angle relative to the horizontal plane
σ_0	:	initial phase of a ray
σ	:	phase of a ray
σ_F	:	phase shift duo to reflection/refraction deduced by Fresnel coefficients
σ_P	:	phase shift due to optical path
σ_f	:	phase shift due to focal lines
$\sigma_{X,p}$	:	phase of the ray of order p with X polarization
$\mathbf{\Theta}$	:	projection matrix

Romain Symbols

a	:	radius of a sphere
$\tilde{A}$	:	complex amplitude
$\mathbf{C}$	:	curvature matrix of particle surface
$\boldsymbol{E}$	:	electric field
H	:	height of droplet
l	:	distance between two successive interaction points within a particle
I	:	intensity of scattered wave with interference
I^{no}	:	intensity of scattered wave without interference
k	:	wave number
$\boldsymbol{k}$	:	wave vector of a ray
m	:	relative refractive index
m_0	:	refractive index of the surrounding medium
m_t	:	refractive index of particle
$\boldsymbol{n}$	:	unit vector normal to the particle surface
N_f	:	total number of focal lines of a ray passes through
N	:	number of emitted photons in SVCRM
O_C	:	center of droplet we set in SVCRM
o_c	:	center of laser source in droplet coordinate system
$\mathbf{Q}$	:	curvature matrix of a wave front
r	:	Fresnel reflection coefficient
r_s	:	radius of laser source
R	:	reflectivity
T	:	transmissivity
t	:	Fresnel refraction coefficient
$\boldsymbol{u}$	:	principal curvature direction of a curved surface
z_e	:	z coordinate of the equatorial plane of a pendent droplet

Superscripts and Subscripts

c	:	for center of light source
C	:	for center of droplet
s	:	for coordinates of a point on the light source plane
(i)	:	parameters for incident ray in SVCRM
(r)	:	parameters for reflection ray in SVCRM
(t)	:	parameters for transmitted ray in SVCRM
(s)	:	parameters for particle surface in SVCRM
i	:	direction perpendicular to the incident plane
j	:	direction parallel to the incident plane
1	:	principal direction parallel to the equatorial plane
2	:	principal direction perpendicular to the equatorial plane
p	:	order of a ray
X	:	polarization state (perpendicular $\perp$ or parallel $\parallel$)

Abbreviations

DDA	:	Discrete Dipole Approximation
FDTD	:	Finite Difference Time Domain
FEM	:	Finite Element Method
LMT	:	Lorenz-Mie Theory
GLMT	:	Generalized Lorenz-Mie Theory
GO	:	Geometrical Optics
GOA	:	Geometrical optics approximation
VCRM	:	Vectorial Complex Ray Model
SVCRM	:	Statistic Vectorial Complex Ray Model

List of Figures

List of Tables

Chapter 1

Introduction

The light scattering is omnipresent in our daily life, in the industrial processes and in many domains of scientific research. For instance, the wavelength dependence of the light extinction in the atmosphere permits to understand why the sky is blue and the sun looks red at sunrise and sunset [1]. The dispersion of the refractive index of water and the refraction of the light in water droplets can be used to explain the disposition of the colors in the rainbows [2]. The on-line control of the diameter of an optical fiber can be realized by simply measuring its scattering properties. We can also have access to the temperature, the sizes and the velocities of droplets in combustion chambers via the signals of light scattered by these droplets, etc. These understandings and the realizations are possible only when the relation between the morphological and material properties of the scatterers and its scattering properties is established. That is just the role of the light scattering theories and the models.

The scientists have been working on this subject for centuries and have developed various theories and models which can be classified into three categories. The first is the rigorous theories which are the exact solutions of the Maxwell equations, such as the Lorenz-Mie theory (LMT) [3, 4] and its generalizations (GLMT) [5, 6]. They are applicable only to particles of simple shapes [7], i.e. the shape of the scatterer must correspond to a mathematical coordinate system (sphere [8], spheroid [9], ellipsoid, circular [10] and elliptical infinite cylinder [11], ...). Though these theories are very limited in the shape of the scatterer, their results serve usually as reference to validate other models and methods. However, except for the homogeneous or stratified sphere and the circular infinite cylinder [12], the calculable size of these theories is often limited to some tens of wavelengths [7, 13] due to the problem of numerical calculation of the involved special functions.

The second category is the numerical methods, which solve the scattering problems numerically with help of the powerful computation resources. For example, T-Matrix [14, 15] solves the electromagnetic scattering using a transformation matrix. Sanamzadeh et al present a solution to a dielectric layered medium with random rough interfaces.

Martin [16] developed a new method for calculating T-matrix of two aspheric obstacles. The T-matrix can also be applied to the calculation of radiation forces. Reference [17] discusses the change of non-radial radiation pressure under the interaction of different chemical composition and spatial arrangement of grain with sunshine. The discrete dipole approximation (DDA) [18, 19, 20] and the finite-difference time-domain (FDTD) [21, 22, 23] can predict the scattering of particles of complex shapes. Yukin, for instance, developed ADDA [24, 20] to speed up the DDA code. But in general, the size of the particles can be calculated with the numerical methods is very limited, it does not exceed few and to a few a hundred wavelengths.

The last category is the approximate models which can be applied to deal with the scattering of particles of irregular shape, but their precision is often not sufficient. As an example, Rayleigh model [25, 26] is a good approximate model for the particles of size much smaller than the wavelength, i.e. $a \ll \lambda$ with a the radius of the particle and λ the wavelength. It predicts that the extinction factor of very small particle is proportional to $1/\lambda^4$, i.e. the extinction of the red light through the atmosphere is much smaller than the blue one, which answers the question the colors about the sky and the sunset. Conversely, the Geometrical Optics (GO) can only deal with the scattering of large particles of dimension much larger than the incident wavelength, i.e. $a \gg \lambda$. Van de Hulst [27] firstly considered the Geometrical optics approximation (GOA) for the scattering of a spherical particle illustrated by a plane wave in detail, which includes the light intensity, phases and two sets of focal lines of optics rays. Extension of geometrical-optics approximation to on-axis Gaussian beam scattering by a spherical particle [28] or a spheroidal particle with end-on incidence [29]. The light scattering of large air bubbles by Geometrical optics approximation is investigated with the relative refractive index smaller than 1 by taking the total reflection into consideration [30]. For this case, Hovenac and Lock [31] proposed that the particle diameter needs to be an order of magnitude larger than the wavelength. GOA is employed for the light scattering by absorbing spherical particles [32], considering spherical particles of different absorption properties. The agreement of scattered light with GOA and LMT is better for larger particles than smaller particles. In addition, the calculation speed of the GOA is independent of the particle size while that of LMT becomes slow with the particle size increasing, which presented GOA is more efficient than LMT for particles. In addtion, GOA has been developed to analyze the scattering of irregular particles. A geometrical-optics approach is also used to deal with the scattering of nonuniform glass microbeads illuminated by on-axis Gaussian beam and comparison of the intensity distributions has been obtained by GOA and GLMT [33]. Using the lognormal statistics to generate particles of various random shapes, Ray optics approximation is devoted to the light scattering of Gaussian random particles [34]. Generating randomly shaped particles by cutting an auxiliary random field by a hyperplane, the relation of scattering matrix elements for irregular shaped particles with scattering angle in the GOA is discussed, the differences of which between the indicatrices at infinity and at a close distance noticeably depend on both the particle shape and the distance [35]. Nevertheless, the precision of the geometrical optics is very limited and it is very difficult to take into account the divergence/convergence of a wave on the surface of the

particle.

In conclusion, none of the aforementioned theories, models or methods can deal with the light scattering of large non-spherical particles with precision. But in practice, we encounter often particles of irregular shapes, such as raindrops in nature, ligament in the atomization or liquid jets in the motor injection. In order to overcome this bottleneck problem, the Vectorial Complex Ray Model (VCRM) [36, 37, 38] for the light scattering by large particles of smooth surface and arbitrary shape has been developed. In this model, all waves are considered as bundles of vectorial complex rays with five parameters: amplitude, phase, direction of propagation, polarization and *wavefront curvature*. The ray direction and the wave divergence/convergence after each interaction of the wave with a dioptric surface as well as the phase shifts of each ray are determined by the vector Snell law and the wavefront equation according to the curvatures of the surfaces. The total scattered field is the superposition of the complex amplitudes of all orders of the rays emergent from the object. Thanks to this simple representation of shaped waves, this model is very suitable for the description of the interaction of an arbitrary wave with an object of smooth surface but complex shape. The application of the model to the scattering of a plane wave by an ellipsoidal particle has been validated numerically [39] and experimentally [40] in the cases a plane of symmetric scattering problems.

In order to extend the applications of the model, we develop algorithms for three dimension objects. VCRM permits to calculate the complex amplitude of each ray but to obtain the total scattering field we must count the contribution of all rays arriving at the same angle. This needs a 2D interpolation of irregular data which is a very difficult and costly task. To get over this obstacle, a statistic version of VCRM, called here after Statistic Vectorial Complex Ray Model (SVCRM), has been proposed and coded by Professor Claude Rozé, in which the total scattered intensity is calculated statistically by summation of the intensity of all rays/photons arriving in boxes in given direction [41]. The scattering patterns simulated by SVCRM agree well with the skeletons of the images obtained experimentally and scattering mechanisms of different orders are identified.

Nevertheless, in the initial version of SVCRM, the interference was not considered. So it cannot predict the fine structure in the scattering patterns. In order to make a complete simulation of the light scattering with SVCRM, *the phase of each ray must be counted and the complex amplitude of the scattered field has to be calculated. This is the main objective of this thesis.*

As an example of applications to demonstrate the power of the VCRM/SVCRM, we choose to study the scattering of a *water droplet*. In one hand, it is easy to be obtained, its property is stable and its surface is naturally smooth. On the other hand, its application is very broad. For instance, the electric charge of spherical water droplets is evaluated for various droplet radii in [42]. The effect of a dense surrounding medium between two approaching charged droplets was studied and the water droplets of precise volume

inside the dielectric medium can be controlled by changing the electrical forces through adjusting electrical conductivity and obtained by experiments and simulations in [43]. In experiment [44], the effects of electrical conductivity on electrospraying modes and its produced droplets are investigated. The dynamic aspects of droplet behavior under various ambient conditions are described in [45], such as charged droplets, instability of droplets, evaporation of a single droplet, droplet generation, etc. The highly heterogeneous and unstable temperature and velocity fields of the gas-vapor mixture were observed, and the aerodynamics of the evaporating droplets and the transverse and transverse dimensions of the heat trace lines were determined in [46]. The effect of overheated random Si Nanowires on impacting water droplets is presented and the effects of the surface temperature and impact velocity on the droplet behavior are also presented in [47]. The dynamic process of single water droplets striking the hot oil surface at the temperature range of 205°C to 260°C is presented in [48]. The behavior of evaporated water droplets on lubricated-impregnated nano-structural surfaces (LINS) was studied experimentally in [49]. The dynamics of non-axis symmetric evaporating droplet with metallic inclusions heated in a high-temperature gas flow is studied in [50]. The impact and freezing process of water droplets was studied experimentally and numerically in [51]. The heating and evaporation of suspended water droplets in a hot air flow are described in [52].

More specifically, we will apply in this thesis our developed model and algorithm to the scattering of the pendent droplets obtained experimentally. Its shape is sufficiently irregular, not as a sphere, a spheroid or an ellipsoid whose surface can be described with a simple mathematical function. The quality of the droplet images and the scattering patterns are sufficiently good for numerical simulation and comparison. The scattering diagrams in three dimension are also very rich in information to be explored.

Finally, we would note that the four terms may be used for the light according to the context: light, wave, ray or photon:

- **light** is very general, used when we talk about light scattering, interaction of light with particle, etc.;
- **wave** emphasizes the wave effect, for wavefront, propagation of (light/electromagnetic) wave, divergence or convergence of a wave;
- **ray** is used in GO, VCRM also in SVCRM. In GO, a ray has four properties: direction, amplitude, polarization state and phase. But it has one more property - wavefront curvature in VCRM and SVCRM.
- **photon** is used only in SVCRM, which has the same properties as **ray** (geometrical and not its quantum sense).

Therefore, we may talk about the *curvature of a ray or a photon*, that means just the wavefront curvature of the wave that is described by the ray or the photon.

The rest of the thesis is organized as follows.

1. Chapter two recalls firstly some fundamentals of Geometrical Optics(GO), including the Snell-Descartes laws and Fresnel coefficients. We then describe how to deal with the scattering of a homogeneous sphere in the framework of GO. The scattering diagrams calculated by GO are compared with the Lorenz-Mie Theory (LMT) to examine the limitation of the GO that is becoming overwhelmingly complex to deal with the scattering of non-spherical particle.

2. Chapter three presents the general principle of the Vectorial Complex Ray Model (VCRM). After that, the Statistic Vectorial Complex Ray Model (SVCRM) is described in detail, for example, how to calculate the complex amplitude of the ray, the total scattered intensity with and without interferences, which is the theoretical guidance for numerical simulation in Chapter 5.

3. Chapter four is devoted to the generation of the pendent droplets and the mathematical description of their profiles. The experimental images of the droplets and their scattering patterns are provided which serve to the numerical simulation in Chapter 5.

4. Chapter five compiles the numerical simulation of the scattering patterns of the pendent droplets under different conditions. These results have been analysed and compared with the experimentally recorded scattering patterns to verify the proposed model SVCRM and investigate the scattering mechanism of a pendent droplet. The effect of detection steps, the number of emitted photons, the size of droplets as well as the incident area of photons on the intensity distribution around the rainbow angle are discussed.

5. Chapter six shows the conclusions and perspectives of this work.

Chapter 2

Fundamentals of Geometrical Optics

Geometrical Optics (GO) is an approximate method allowing describing the propagation and interaction of light with particles when the light wavelength λ is much smaller than the dimension of the particles. In this case, the light wave is modelled as rays (pencil of light). The wave effects of the light are then ignored. The essential advantage of the GO is its simplicity and flexibility in dealing with the formation of image and the interaction of light with objects, especially when their shapes are not regular.

The Statistic Vectorial Complex Ray Model (SVCRM), an extension of the Vectorial Complex Ray Model (VCRM), developed in this thesis is fundamentally based on the geometrical optics. Therefore, we will recall the fundamentals of GO in this first chapter for two purposes: to **define the notations used in next chapters** and to **introduce the understanding and analysis of the scattering mechanics**.

In the field of theoretical and numerical research on the interaction of light with particles, the scattering of the plane wave by a spherical particle (or a circular cylinder) is the only case we can deal *fully* with the classical GO. It will be recalled in this chapter to help us to understand the newly developed SVCRM. Some numerical results will be presented also because they will be used later on for the validation of SVCRM in the following chapters.

2.1 Basis of Geometrical Optics

When light travels from one medium to another of different refractive index, reflection and refraction of the light occur. The propagation direction of the light may be deviated. The amplitudes and the phases of the reflected and the transmitted waves change. We recall the Snell-Descartes laws and the Fresnel formulas to describe the relations between

these parameters and the properties of the media. Numerical results are also given to illustrate the variation of them with the refractive index, the incident angle and the polarization state of the incident wave.

2.1.1 Snell-Descartes laws

Snell-Descartes laws [53] describe the relationship between the directions of the reflected ray and the refracted ray with that of the incident ray when light passes through a interface between two media. The Snell-Descartes laws state also that the incident ray, the reflected ray and the refracted ray are all in the incidence plane which is defined by the incident ray and the normal of the surface. They can be expressed with the following two equations:

$$\theta_r = \theta_i \tag{2.1}$$

$$m_i \sin\theta_i = m_t \sin\theta_t \tag{2.2}$$

where θ_i, θ_r and θ_t are respectively the angles of the incident ray, the reflected ray and the refracted ray relative to the normal of the interface of the two media, as shown in Fig. 2.1. m_i and m_t are the refractive indices of the first (incident) and the second (transmitted) media.

Usually, to simplify the notation, we use the relative refractive index m defined as the ratio of the refractive indices of the two media:

$$m = \frac{m_t}{m_i} \tag{2.3}$$

Then the refraction angle θ_t can be given by:

$$\sin\theta_t = \frac{1}{m}\sin\theta_i = \frac{1}{m}\sqrt{1-\cos^2\theta_i} \tag{2.4}$$

When the light passes from an optically denser medium to a optically light less dense medium, i.e. $m < 1$, the quantity $\sin\theta_i/m$ may be bigger than one. In this case, total reflection occurs. The limit of the incident angle at which total reflection occurs is called critical angle θ_C and given by:

$$\theta_C = \arcsin(m) \tag{2.5}$$

That means all rays with incident angle $\theta_i \geqslant \arcsin(m)$ are totally reflected.

2.1.2 Fresnel coefficients

When a wave is incident on an interface plane between two media, a part of the energy is reflected and the other part is transmitted. The amplitudes of the reflected wave and

the refracted wave with that of the incident wave are given by the Fresnel formulas [53].

Consider an incident wave of electric field $\boldsymbol{E}$ decomposed in two components, one perpendicular to the incident plane $E_{\perp}^{(i)}$ and the other one parallel to the incident plane $E_{\parallel}^{(i)}$ (see Fig. 2.1).

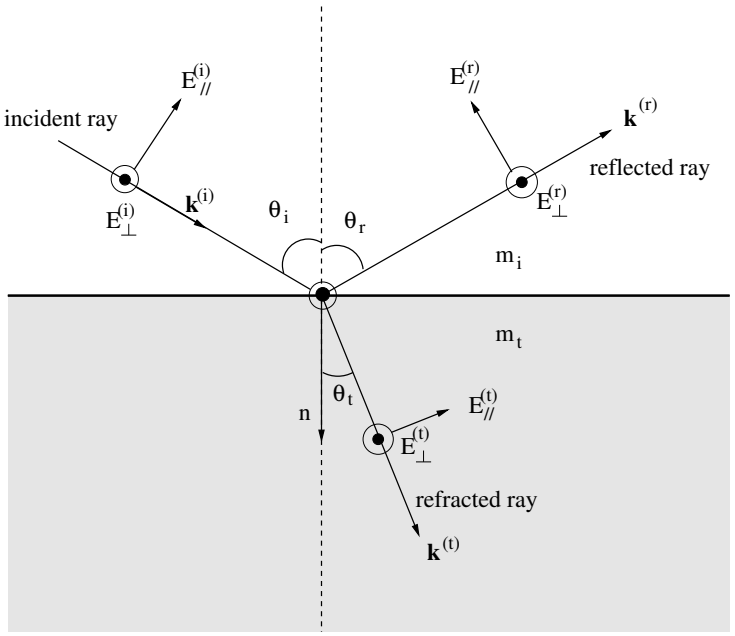

Figure 2.1: Directions and electric vectors of the rays used in Snell laws and Fresnel formulas.

We define the ratios of the electric amplitudes of the reflected wave and the transmitted wave to that of the incident wave by

$$\begin{aligned} r_X &= \frac{E_X^{(r)}}{E_X^{(i)}} \\ t_X &= \frac{E_X^{(t)}}{E_X^{(i)}} \end{aligned} \tag{2.6}$$

where $X = \perp$ or $\parallel$ stands for the polarization state of the wave. These ratios are called Fresnel coefficients and given by the Fresnel formulas for the perpendicular polarization:

$$\begin{aligned} r_\perp = \frac{E_\perp^{(r)}}{E_\perp^{(i)}} &= \frac{\cos\theta_i - m\cos\theta_t}{\cos\theta_i + m\cos\theta_t} \\ t_\perp = \frac{E_\perp^{(t)}}{E_\perp^{(i)}} &= \frac{2\cos\theta_i}{\cos\theta_i + m\cos\theta_t} \end{aligned} \tag{2.7}$$

and for the parallel polarization:

$$\begin{aligned} r_{\parallel} = \frac{E_{\parallel}^{(r)}}{E_{\parallel}^{(i)}} &= \frac{\cos\theta_t - m\cos\theta_i}{\cos\theta_t + m\cos\theta_i} \\ t_{\parallel} = \frac{E_{\parallel}^{(t)}}{E_{\parallel}^{(i)}} &= \frac{2\cos\theta_i}{\cos\theta_t + m\cos\theta_i} \end{aligned} \tag{2.8}$$

It should be noted that when the total reflection occurs, $\sin\theta_i > m$ and $\cos\theta_t$ becomes a complex numbers. In this case, the Fresnel coefficients for the total reflection can be expressed as [53]:

$$\begin{aligned} r_{\perp} &= \frac{\cos\theta_i - i\sqrt{\sin^2\theta_i - m^2}}{\cos\theta_i + i\sqrt{\sin^2\theta_i - m^2}} \\ r_{\parallel} &= \frac{i\sqrt{\sin^2\theta_i - m^2} - m^2\cos\theta_i}{i\sqrt{\sin^2\theta_i - m^2} + m^2\cos\theta_i} \end{aligned} \tag{2.9}$$

These two coefficients are complex numbers.

We would note also that the reflection coefficients may also be negative. In both cases: the reflection coefficients negative or complex, the reflected wave experiences a phase jump on reflection. This phase shift $\sigma_{F,X}$ can be calculated by the argument of the reflection coefficient:

$$\sigma_{F,X} = \arg(r_X) \tag{2.10}$$

In the case of parallel polarization, the reflection coefficient $r_{\parallel}$ is zero when $\cos\theta_t = m\cos\theta_i$. This special angle of incidence is called Brewster's angle and is given by:

$$\theta_B = \arctan(m) \tag{2.11}$$

At this angle, the reflected light is perfectly polarized in the perpendicular direction to the incident plane if the incident light is unpolarized. This property is widely used in optical devices.

2.1.3 Reflectivity and transmissivity

When a wave of light or a bundle of rays arrives on the interface between two media, the incident light generally splits two parts: one is the reflected light and the other the transmitted light. The cross section of the refracted bundle of rays is usually different from that of the incident bundle of rays due to the deviation of the propagation direction. We derive in the following the reflectivity and transmissivity which are the

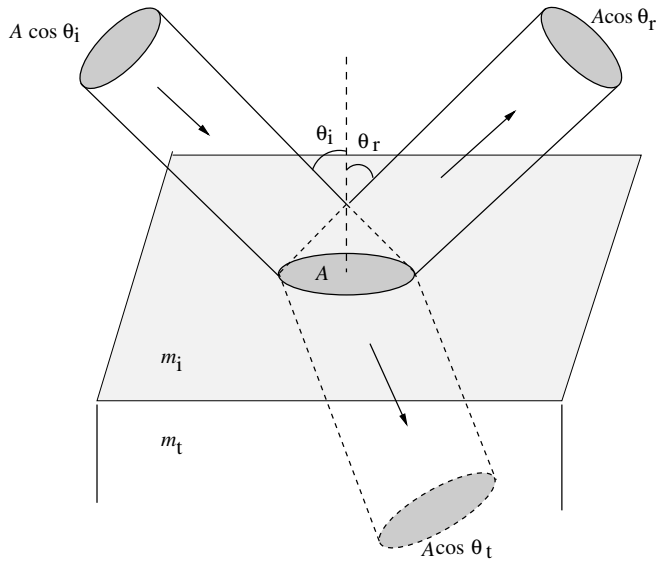

Figure 2.2: Energy flux of light during the reflection and the refraction with an oblique incidence

ratios of the reflected and transmitted energy flux to the incident one as function of the Fresnel coefficients.

Consider a bundle of rays illuminating an area A on the surface (Fig. 2.2). For a plane wave, the intensity of light being $I = ||\boldsymbol{E} \times \boldsymbol{H}|| = \sqrt{\varepsilon_0/\mu_0} m E_0^2/2$ for non-magnetic-dielectric medium (here, ε_0 is the vacuum permittivity and μ_0 is the vacuum magnetic permeability, m indicates the refractive index in the medium). The energy flux of the incident light, the reflected light and refracted light on the area are respectively

$$J^{(i)} = \frac{1}{2}\sqrt{\frac{\varepsilon_0}{\mu_0}} m_i E_0^{(i)^2} \cos\theta_i, \tag{2.12}$$

$$J^{(r)} = \frac{1}{2}\sqrt{\frac{\varepsilon_0}{\mu_0}} m_i E_0^{(r)^2} \cos\theta_r, \tag{2.13}$$

$$J^{(t)} = \frac{1}{2}\sqrt{\frac{\varepsilon_0}{\mu_0}} m_t E_0^{(t)^2} \cos\theta_t. \tag{2.14}$$

The reflectivity R_X and the transmissivity T_X are given by

$$\begin{aligned} R_X &= \frac{J^{(r)}}{J^{(i)}} = \frac{m_i \cos\theta_r}{m_i \cos\theta_i} \left| \frac{E_X^{(r)}}{E_X^{(i)}} \right|^2 = \frac{\cos\theta_r}{\cos\theta_i} |r_X|^2 \\ T_X &= \frac{J^{(t)}}{J^{(i)}} = \frac{m_t \cos\theta_t}{m_i \cos\theta_i} \left| \frac{E_X^{(t)}}{E_X^{(i)}} \right|^2 = \frac{m_t \cos\theta_t}{m_i \cos\theta_i} |t_X|^2 \end{aligned} \tag{2.15}$$

Because $\theta_r = \theta_i$ and $m_t/m_i = m$, Eq. (2.15) can be expressed as:

$$\begin{aligned} R_X &= \mid r_X \mid^2 \\ T_X &= 1 - R_X = \frac{m \cos\theta_t}{\cos\theta_i} \mid t_X \mid^2 \end{aligned} \tag{2.16}$$

The above derivation is based on the energy balance on the illuminated area and we have naturally $T_X + R_X = 1$. The transmissivity is not equal to the square of the amplitude ratio of the transmitted wave to the incident wave because the cross section of the transmitted wave is different from those of the incident and reflected waves.

2.1.4 Numerical results and discussions

In this part, numerical results on the Fresnel coefficients, the phase shifts, and the transmissivity and the reflectivity are presented as function of incident angle for different refractive indices with the simulated step of number 300. This investigation provides a concrete understanding of the properties of reflected wave and transmitted wave, and this will be very helpful for the analysis in the following chapters.

The variation of the four Fresnel coefficients are shown in Fig. 2.3 as function of the incident angle for two relative refractive indices, one larger than unit and the other less than 1.

We find that when light passes from an optically looser medium to a denser one (the relative index greater than 1, Fig. 2.3(a)), the two Fresnel coefficients of the transmitted light (red and blue curves) are always positive whatever the state of polarization, the Fresnel coefficient of reflection is always negative for the perpendicular polarization, while that of reflection for parallel polarization is positive when the incident angle is less than the Brewster angle ($\theta_B = 53.12°$ for $m = 1.333$), and negative when the incident angle is greater than the Brewster angle. This means that the phase of the reflected wave experiences a jump π when the incident angle passes the Brewster angle.

When the light passes from an optically denser medium to a looser one (the relative index less than 1, Fig. 2.3(b)), if the incident angle is greater than the critical angle ($\theta_C = 48.59°$ for $m = 0.75$), the Fresnel coefficients of reflection ($r_\perp$ and $r_\parallel$) are equal to unit and those of refraction ($t_\perp$ and $t_\parallel$) are zero, so the total reflection occurs. When the incident angle is less than the critical angle, the variation of the Fresnel coefficients are similar to those in the case $m > 1$. However, it is worth to note that the two Fresnel coefficients of refraction are both greater than 1 and the Fresnel coefficient of reflection for the parallel polarization passes from negative to positive at the Brewster angle ($\theta_B = 36.87°$) in the inverse sense to that for $m > 1$.

The phase shift due to the reflection or refraction can be deduced from the Fresnel coefficient according to Eq. (2.10). The variation of this phase shift as function of

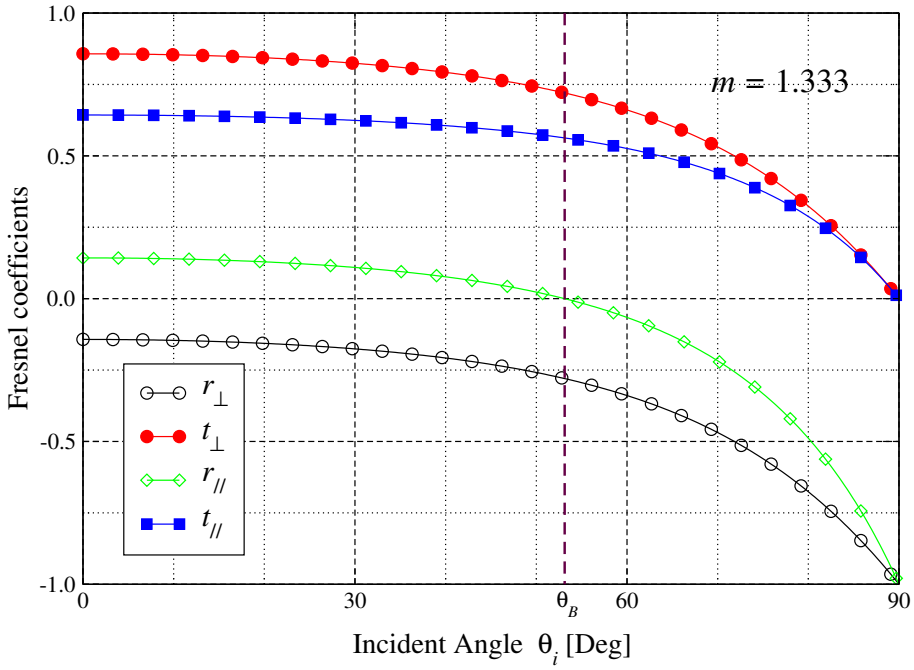

(a) $m = 1.333$

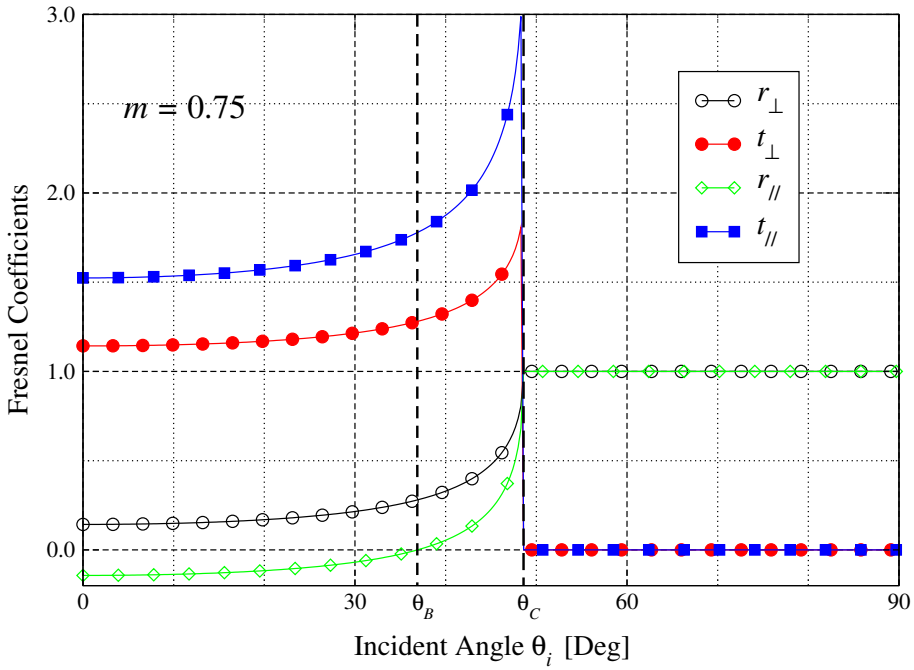

(b) $m = 0.75$

Figure 2.3: Fresnel coefficients as function of incident angle θ_i for the relative refractive index $m = 1.333$ and 0.75.

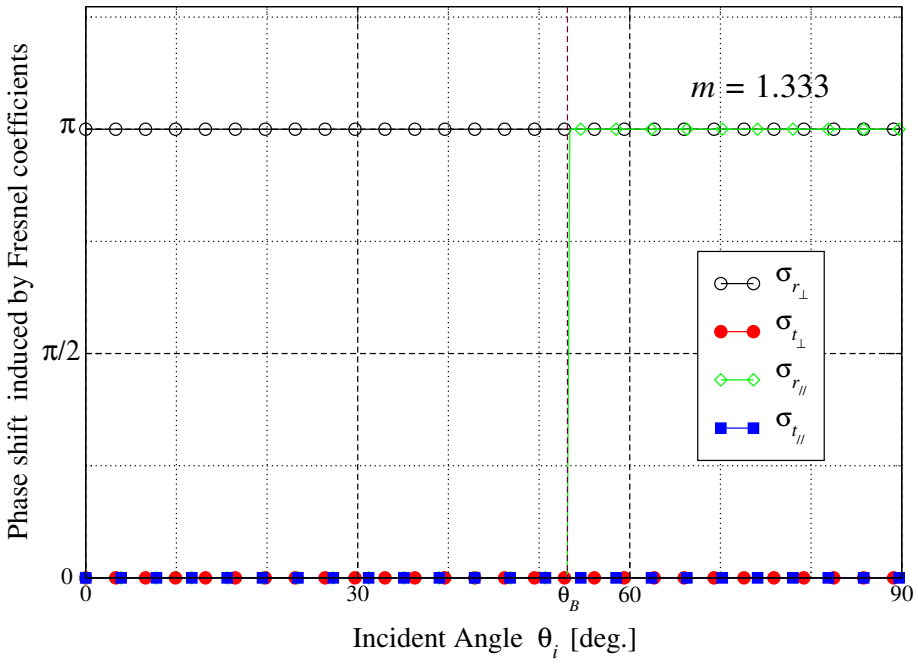

(a) $m = 1.333$

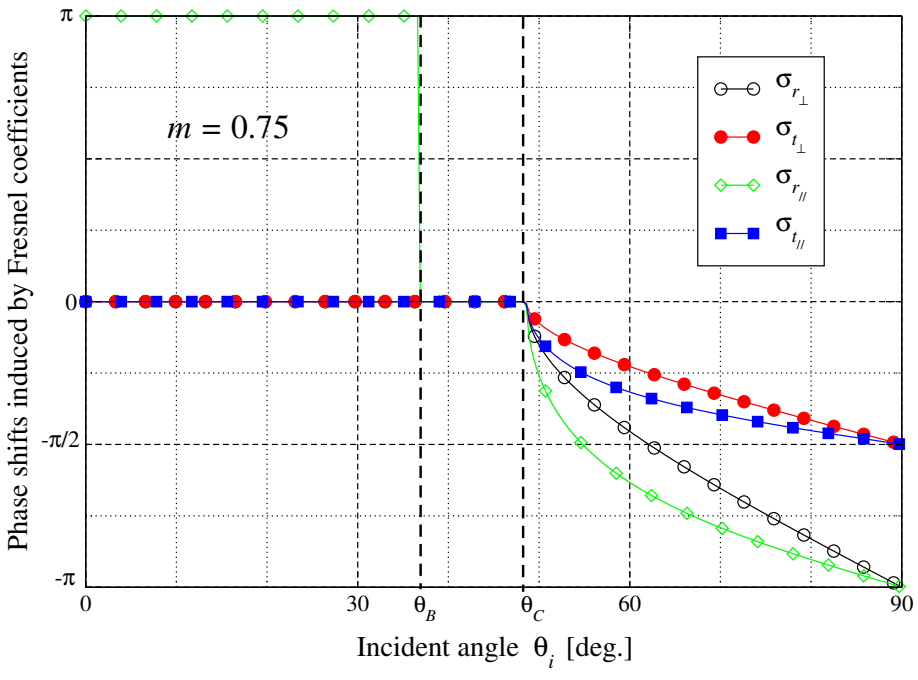

(b) $m = 0.75$

Figure 2.4: Phase shifts of the reflected and refracted rays on the surface (a): from air to water and (b): from water to air

incident angle is given in Fig. 2.4 for the two values of refractive index. When the relative refractive index is greater than 1, there is no phase shift for the refracted wave whatever the polarization. The phase shift is also 0 for the perpendicularly polarized reflected wave, while the phase of the reflected wave undergoes a phase jump at Brewster angle.

When the relative refractive index is less than 1, the phase shift is much more complicated. When the incident angle is less than the critical angle, there is no phase shift for the refracted wave and the reflected wave in perpendicular polarization. The reflected wave in parallel polarization experiences a phase jump equal to π at the Brewster angle. The phase shift varies continuously when the incident angle is greater than the critical angle, i.e. in the total reflection case, the phase shift decreases from 0 at critical angle to $-\pi/2$ for refracted wave and to $-\pi$ for reflected wave at $\theta_i = 90°$.

Finally, we show in Fig. 2.5 the reflectivity and the transmissivity as function of incident angle with also two values of relative refractive index, one greater than unit and the other less than 1. We note simply that the curves for the relative index less than 1 is similar to that for the case $m > 1$ but compressed to the region of incident angle between 0 and the critical angle. The reflectivity for the perpendicular polarization increases monotonically to 1 at 90° for $m > 1$ and at critical angle for $m < 1$, while the reflectivity for parallel polarization decreases until 0 at Brewster angle and then increases until 1.

The above analysis provides us a general view about the properties of the reflected wave and the refracted wave as function of incident angle, the state of polarization of the incident wave and the relative refractive index, especially the amplitudes and the phase shifts of the reflected and the refracted waves as well as the reflectivity and transmissivity. On this basis, we will investigate the scattering of a large homogeneous sphere with GO in the following section.

2.2 Geometrical optics for scattering of a sphere

In Geometrical optics, the divergence and the convergence of the wave on the surface of the particle is usually not taken into account. However, when dealing with the scattering of light by a sphere, we can not only deduce the four properties of each ray from the fundamental laws given in the previous section, but also obtain an analytical expression of a factor describing the divergence and convergence of a wave on the particle surface and the phase shift due to the focal lines.

This section consists of two parts. First, we will give a general description of how to deal with the scattering problem in the framework of GO, and then some numerical results will be exemplified. The advantages and the limit as well as its precision will be investigated by comparison with Lorenz-Mie theory.

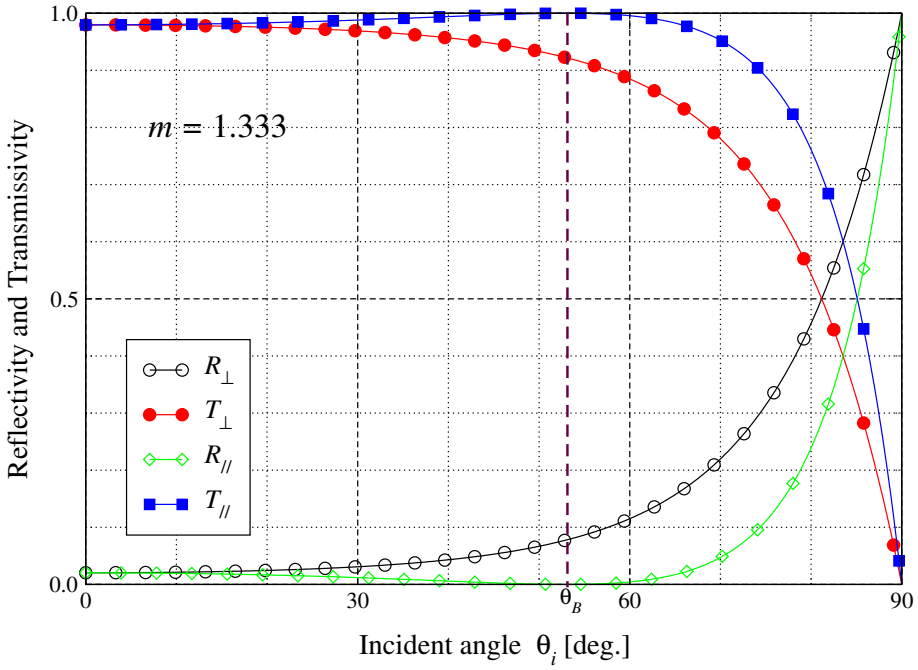

(a) $m = 1.333$

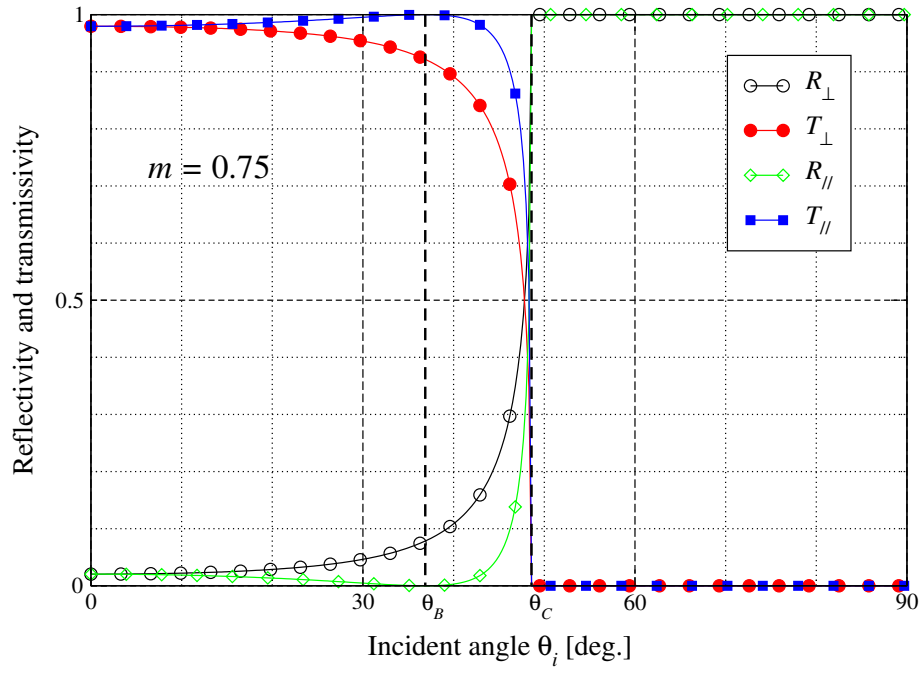

(b) $m = 0.75$

Figure 2.5: Reflectivity and transmissivity as function of incident angle θ_i for two relative relative refractive indice.

2.2.1 Description of the method

Consider a plane wave of wavelength λ propagating along z axis which illuminates a sphere of real refractive index m_t and radius a. The trajectory of a ray is given in Fig. 2.6. Its interaction position on the sphere is characterized by an angle θ_i and its distance from the axis z, which is $a\cos\tau$, where τ is the complementary angle of θ_i, i.e. angle between the particle surface and the incident ray. Each time a ray interacts with the particle surface, it is split in two parts: the reflected ray and the refracted ray. We call emergent ray of order p,the ray which exits from the particle after $p+1$ interactions with the particle surface. Thus, the rays experience a specular reflection on the outer surface of the particle are of order $p = 0$, the rays exiting after two refractions are of order $p = 1$, etc.

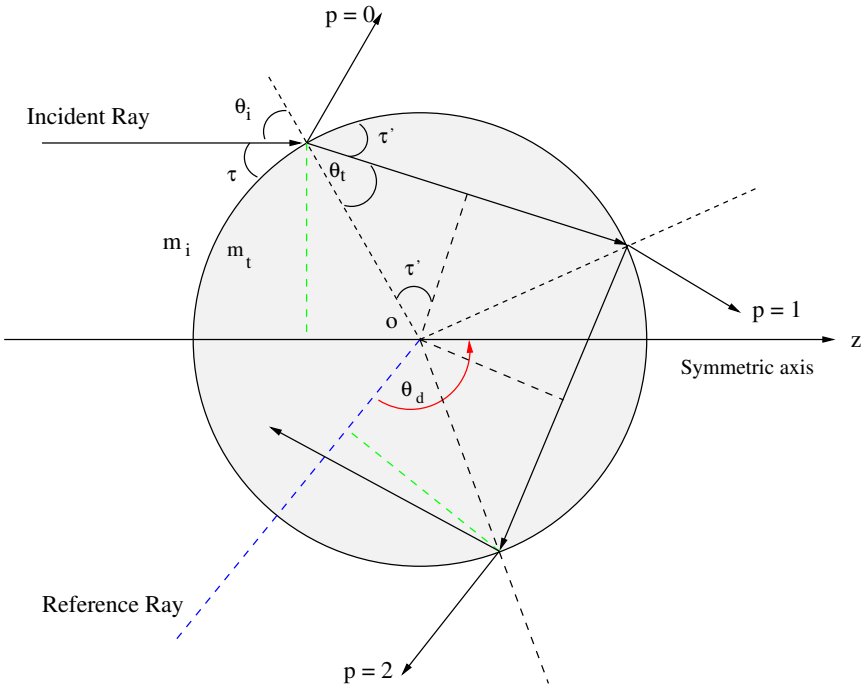

Figure 2.6: Schema of light interaction with a large sphere according to Geometrical optics

Owing to the symmetry of the sphere, the angle of any emergent rays with respect to the normal of the particle surface is constant and equal to the incident angle θ_i. The angle between any ray in the particle and the normal of the surface is also constant and equal to the refraction angle θ_t. Similarly, τ' is the complementary angle of the refraction angle[1]. The relation between the incident angle and the refraction angle, or equivalently the relation between the angles τ and τ' is given by the Snell-Descartes law Eq. (2.2):

$$\cos\tau' = \frac{1}{m}\cos\tau \tag{2.17}$$

[1]For convenience we use in this section the angles τ and τ' instead of θ_i and θ_t as in the literature on the subject[Van de hulst1981] [3].

Direction of emergent rays

Since the angles of all the emergent rays with respect to the particle surface are constant and the angles of all the rays in the particle make the same angle with the particle surface also, the deviation angle of any emergent ray can be given analytically as function of the incident angle and the refraction angle. For example, the deviation angle θ_0 of the externally reflected ray ($p = 0$) with respect to the incident direction is 2τ in counterclockwise sense. For the refracted ray, there is a $2\tau'$ deviation angle in clockwise sense for each interaction. The deviation angle θ_p of the emergent ray of order p is therefore:

$$\theta_p = 2\left(\tau - p\tau'\right) \tag{2.18}$$

However, the scattering light is generally observed in the range of $[0°, 360°]$. Particularly, for the scattering of plane wave by a sphere, the scattering angle is usually given in the interval $[0°, 180°]$ owe to the symmetry of the problem. In this case, the scattering angle of a ray of order p can be expressed as [3]:

$$\theta_{sp} = 2q_p\left(\tau - p\tau'\right) + 2k_p\pi \tag{2.19}$$

where k_p is a integer, which stands for the times that the emergent ray crosses the z axis, and q_p is $+1$ or -1.

The differentiation of the scattering angle with respect to τ gives

$$\frac{d\theta_{sp}}{d\tau} = 2\left(1 - p\frac{\tan\tau}{\tan\tau'}\right) \tag{2.20}$$

When the derivative is zero, the scattering angle reaches an extreme value which corresponds to the geometrical rainbow angle θ_{OG}:

$$\theta_{GO}(m,p) = 2\left|\arctan\left(\sqrt{\frac{m^2-1}{p^2-m^2}}\right) - p\arctan\left(p\sqrt{\frac{m^2-1}{p^2-m^2}}\right) + q\pi\right| \tag{2.21}$$

where q is a integer to be chosen so that $\theta_{OG} \in [0, \pi]$. Eq. (2.20) will also be used to calculate the divergence factor.

Amplitudes of emergent rays

The amplitude of an emergent ray is affected by two factors:

$\varepsilon_{X,p}$ due to reflection and transmission on the particle surface: this factor depends on the polarization state and the order of the rays. It is always less than 1.

D_p due to divergence and convergence of the wave: the amplitude of the emergent wave may be greater or smaller than the incident one depending on the curvature of the particle surface – concave or convex at different interaction points.

The amplitude ratios of the reflected and the transmitted waves to the incident wave at each interaction are given by the Fresnel formulas[2]:

$$\begin{aligned} r_\perp &= \frac{\sin\tau - m\sin\tau'}{\sin\tau + m\sin\tau'} \\ r_\parallel &= \frac{m\sin\tau - \sin\tau'}{m\sin\tau + \sin\tau'} \end{aligned} \tag{2.22}$$

Since the angles τ and τ' are constants for all order rays in the scattering of plane wave by a sphere, the amplitude ratio of the emergent rays of order p can be given by these two constant coefficients $r_\perp$ and $r_\parallel$. For example, for the rays of order $p = 0$, the amplitude ratio of the reflected wave to the incident one is directly the Fresnel coefficient of reflection r_X. The rays of order $p = 1$ experience two refractions (transmissions), so the amplitude ratio is given by $t_X^2 = 1 - r_X^2$. In general, the rays of order $p \geq 1$ experience two refractions (transmissions) and $p-1$ reflections on the internal surface of the particle for which the Fresnel coefficient is $-r_X$ calculated by Eq. (2.22). Therefore, the amplitude ratio of an emergent ray of order p to the incident ray is given by

$$\varepsilon_{X,p} = \begin{cases} r_X & \text{for } p = 0, \\ (-r_X)^{p-1}\left(1 - r_X^2\right) & \text{for } p > 0. \end{cases} \tag{2.23}$$

where, r_X is the Fresnel coefficients of reflection for polarization $X = \perp, \parallel$ given in Eq. (2.22).

When a wave arrives on a curved surface, its wavefront will be changed, i.e. converged or diverged, according to the curvature of the surface. Therefore, the amplitude of the emergent wave per unit surface will increase or decrease. This variation can be described by the divergence factor, which can be derived analytically by the balance of energy for the scattering of a plane wave by a sphere.

Consider a finite pencil of light illuminating the sphere. Let I_0 denote the intensity of the incident light. The illuminated area can be expressed as function of angle increments $d\phi$ and $d\tau$ such that $dS = a\cos\tau d\phi \cdot a d\tau = a^2\cos\tau d\tau d\phi$. The flux of energy in this pencil is therefore $I_0 \sin\tau dS = I_0 a^2 \sin\tau\cos\tau d\tau d\phi$. After successive interactions with the particle surface, this energy flux in area dS spreads into a solid angle $\sin\theta_{sp} d\theta_{sp} d\phi$, i.e., over an area $dS_s = r^2 \sin\theta_{sp} d\theta_{sp} d\phi$ at a large distance r from the sphere. If we

[2]These two formulas are the same as those given in section 2.1 but as function of the complementary angles of the incident and refraction angles. The two complementary angles are preferred in the study of the scattering of a plane wave by a sphere, since it simplifies the notation, especially for the deviation angle.

neglect the energy loss due to absorption and suppose that the intensity of scattered wave of order p at angle θ_{sp} is $I_x(p, \theta_{sp})$ we will have $I_0 \sin\tau dS \cdot \varepsilon_X^2 = I_X(p, \theta_{sp}) dS_s$ i.e.

$$\begin{aligned} I_X(p, \theta_{sp}) &= \frac{\varepsilon_X^2 I_0 a^2 \cos\tau \sin\tau d\tau d\phi}{r^2 \sin\theta_{sp} d\theta_{sp} d\phi} \\ &= \frac{a^2}{r^2} I_0 \varepsilon_X^2 D_s \end{aligned} \tag{2.24}$$

where D_s is called the divergence factor of the wave defined by

$$\begin{aligned} D_s &= \frac{\sin\tau\cos\tau}{\sin\theta_{sp}\left|\frac{d\theta_{sp}}{d\tau}\right|} \\ &= \frac{\sin 2\tau}{4\sin\theta_{sp}\left|1 - p\frac{\tan\tau}{\tan\tau'}\right|} \end{aligned} \tag{2.25}$$

according to the Eq. (2.20). Then, the divergence factor of the rays of order p can be expressed by the incident θ_i and refraction angles θ_t:

$$D_s = \frac{\sin 2\theta_i}{4\sin\theta_{sp}\left(p\frac{\cos\theta_i}{\cos\theta_t} - 1\right)} \tag{2.26}$$

For the rays of low orders, $\sin\theta_{sp}$ can be further expressed as function of the incident θ_i and refraction angles θ_t in simple form. For example, the divergence factor of order $p = 0$ is:

$$D_{s0} = \frac{\sin 2\theta_i}{4\sin(\pi - 2\theta_i)} = \frac{1}{4} \tag{2.27}$$

since the scattering angle $\theta_{sp} = \pi - 2\theta_i$.

Similarly, we can obtain the divergence factor for order $p = 1$:

$$D_{s1} = \frac{\sin 2\theta_i}{4\sin\left[2\left(\theta_t - \theta_i\right)\right]} \cdot \frac{m\cos\theta_t}{\cos\theta_i - m\cos\theta_t} \tag{2.28}$$

and for order $p = 2$:

$$\begin{aligned} D_{s2} &= \frac{\sin 2\theta_i}{4\sin\left[2\left(\theta_t - \theta_i\right) - \pi\right]} \cdot \frac{m\cos\theta_t}{2\cos\theta_i - m\cos\theta_t} \\ &= -\frac{\sin 2\theta_i}{4\sin\left[2\left(\theta_t - \theta_i\right)\right]} \cdot \frac{m\cos\theta_t}{2\cos\theta_i - m\cos\theta_t} \end{aligned} \tag{2.29}$$

These analytical expressions are useful to check our code and the divergence factor in VCRM.

Phase of emergent rays

When the incident wave is a plane wave, its phase is constant. The phase shift of a ray during the interaction with the particle is caused by three facts [3]:

- σ_P: phase shift due to the optical path,
- σ_F: phase shift due to reflection and refraction, which can be calculated from the Fresnel coefficients,
- σ_f: phase shift due to the focal lines.

The phase of an emergent ray is given by

$$\sigma_p = \sigma_P + \sigma_F + \sigma_f \tag{2.30}$$

Thanks to the symmetry of the sphere, all the three phase shifts can be expressed analytically as function of the incident angle and the parameters of the sphere.

1. Phase shift due to Fresnel coefficients σ_F:

   This phase shift can be calculated directly by Eq. (2.10). The variation of the phase shift as function of the incident angle has been investigated in the first section in this chapter for the relative reflective index smaller or greater than unity.

   In our case of plane wave scattering by a sphere, the total reflection can never occur on the internal surface. The Fresnel coefficients can never be complicated and the phase shift due to the Fresnel coefficient is given according to Eq. (2.23) by

   $$\sigma_F = \arg(\varepsilon_{X,p}) = \begin{cases} \arg(r_X) & \text{for } p = 0, \\ (p-1)\arg(-r_X) & \text{for } p > 0. \end{cases} \tag{2.31}$$

2. Phase shift due to optical path σ_P:

   The phase shift σ_P of a ray induced by the optical path is calculated by:

   $$\sigma_P = \frac{2\pi}{\lambda}\Delta L \tag{2.32}$$

   where ΔL is the difference of the optical path of the emergent ray and the reference ray, which is a ray would arrive at the particle center in the same direction as the incident ray and would go out in the same direction as the emergent ray as if there is no particle.

   The specularly reflected ray by the external surface of the sphere ($p = 0$) in Fig. 2.6 has a shorter path than the reference ray $\Delta L_0 = 2a\sin\tau$ and leads to

a positive phase shift $\sigma_P = 2\pi/\lambda \cdot 2a\sin\tau$. The optical path of the refracted ray of order $p \geq 1$ is longer than that of the reference ray. Therefore, it leads to a negative phase shift. The distance of two adjacent interaction points of the ray with the sphere surface is $2a\sin\tau'$. Therefore, the optical path difference of an emergent ray of order p to its corresponding reference ray is $2a(\sin\tau - 2pm\sin\tau')$. The phase shift σ_P due to the optical path difference for the rays of order p is:

$$\sigma_P = \frac{2\pi}{\lambda} 2a(\sin\tau - 2pm\sin\tau') = 2\alpha(\sin\tau - 2pm\sin\tau') \tag{2.33}$$

where $\alpha = 2\pi a/\lambda$ is the size parameter of the particle and λ the wavelength of the incident wave in the surrounding medium.

3. Phase shifts due to focal lines/points σ_f:

   According to Van de Hulst[3], the phase of wave advances by $\pi/2$ when it passes through a focal line. Thus, it is necessary to count the number of focal lines and focal points encountered along the entire path (a focal point is two perpendicular focal lines located at the same point). It is found that the rays pass $p-(1-s)/2$ focal points, which are the intersection point of two adjacent rays in scattering plane, and $-2k_p + (1-q_p)/2$ focal lines that are the intersection points of a ray with the central optical axis. The integers p, k_p and q_p are defined in Eq. (2.19) and $s = +1$ or -1 denotes the sign of the derivative $d\theta_d/d\tau$. So the total phase shift due to the focal lines σ_f is given by:

$$\sigma_f = \frac{\pi}{2}\left(p - 2k_p + \frac{s - q_p}{2}\right) \tag{2.34}$$

Finally, the total phase shift of an emergent ray of order p relative to the reference ray is given by

$$\sigma_p = \sigma_F + 2\alpha(\sin\tau - 2pm\sin\tau') + \frac{\pi}{2}\left(p - 2k_p + \frac{s - q_p}{2}\right) \tag{2.35}$$

where σ_F is given by Eq. (2.31). This Eq. (2.35) will be used in Eq. (2.36) to calculate the complex amplitudes of the emergent rays.

Scattering intensity

The incident wave being coherent, the emergent rays arriving at the same position or in the direction may interfere. Because we are interested in the scattering in far field, all the emergent rays in the same direction (θ, ϕ) will interfere. The amplitude of the resultant field should be calculated therefore by the summation of the complex amplitudes of all the emergent rays in the same direction.

The amplitude and the phase of each emergent ray have been calculated above. The complex amplitude of a ray is then given by

$$\tilde{A}_{X,i}(\theta,\phi) = \alpha A_{X,0} \mid \varepsilon_{X,i} \mid \sqrt{D_{sp}} e^{i\sigma_{X,i}} \tag{2.36}$$

where $A_{X,0}$ stands for the amplitude of the incident wave with the polarization state X: Index i denotes the i^{th} ray arriving in the direction (θ,ϕ). It should be noted that not all orders of rays arrive in all the directions and the rays from the same order may reach the same direction several times. On the other hand, the scattered wave is spherical in far field, so the factor $1/(r)^2$ in Eq. (2.24) is suppressed as a convention.

In a given direction (θ,ϕ), the total complex amplitude is calculated by the summation of the complex amplitudes of all rays arriving at the same angle:

$$\tilde{A}_X(\theta,\phi) = \sum_{i=0}^{\infty} \tilde{A}_{X,i}(\theta,\phi) \tag{2.37}$$

The total intensity is therefore

$$I(\theta,\phi) = \mid \tilde{A}_{\perp}(\theta,\phi) \mid^2 + \mid \tilde{A}_{\parallel}(\theta,\phi) \mid^2 \tag{2.38}$$

Numerical simulation of the scattering diagrams of a plane wave by a sphere will be presented in the next subsection and compared to the results of the Lorenz-Mie theory in order to evaluate the accuracy and the applicability of the geometrical optics in the light scattering.

2.2.2 Simulation results and discussions

The method of GO on the scattering of a plane wave by a spherical particle will be applied to calculate the scattering diagrams in this section. We suppose that the absorption inside the particle is negligible, so the relative refractive index is real. In this section, the number of ray is 500.

We present first in Fig. 2.7 the ray tracing in and out of a sphere. For clarity, only the above half of the sphere is illuminated (in cyan color). The reflected rays ($p = 0$ in green) spread in all directions. The refracted rays ($p = 1$ in red) are confined in the forward directions and experience a focal point outside of the particle (passing by the symmetric axis) and the rays far from the axis may have a focal line inside the particle. The rays of second order $p = 2$ (in blue) and third order $p = 3$ (in dark green) have each of them a extreme deviation angle, about 138° for $p = 2$ and 127° for $p = 3$, where the scattered intensity predicted by GO tends to infinity. These are the so called geometrical rainbow angles.

Then the intensity of the emergent rays of different orders as well as the total scattered intensity calculated by GO are shown in Fig. 2.8. The minimum value of the order of

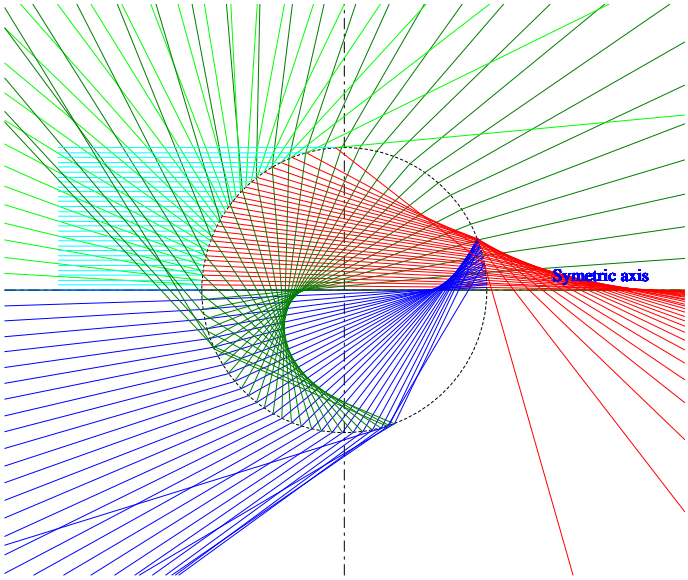

Figure 2.7: Ray tracing by GO for a sphere ($m = 1.333$) illuminated by a plane wave. For clarity, only the above half of the sphere is considered with $p = 3$.

ray is 0 and the maximum value of that is 4. The interference is taken into account for the total intensity but not for the individual orders. The intensity of the individual order is determined by the two factors: the Fresnel coefficients and the divergence factor. For example, the intensity of the rays of order $p = 0$ decreases monotonically as function of scattering angle for the perpendicular polarization but tends to zero at 74° for the parallel polarization the later corresponds to the Brewster angle $\theta_B = 53.12°$ because the scattering angle is related to the incident angle by $\theta_s = 2\tau = 2(90° - \theta_i)$ for $p = 0$. Similarly, the minimum intensity for the parallel polarization in the other orders are all due to the Brewster angle.

At the same time we observe that all the peaks are located at the same angles for the two polarization. These are due to the divergence factor, which are independent of the polarization and can be predicted by the formulas given in the previous section.

To evaluate the accuracy of the GO, we will compare the scattered intensities calculated by the GO and the LMT for a particle of radius illuminated by a plane wave. For a complete comparison, the diffraction must be taken into account. This can be done by considering the sphere as a opaque disk of the same section. The amplitude of the diffracted field is given by

$$A_d(\theta) = \alpha \frac{J_1(\alpha\theta)}{\alpha\theta} \tag{2.39}$$

where, J_1 is the first-order Bessel function of the first kind. $A_d(\theta)$ is added into Eq. (2.37) The scattered diagrams calculated by the two methods for a particle of a large particle ($a = 100$ μm, $m = 1.333$) are given in Fig. 2.9. The minimum value of the order of ray is 0 and the maximum value of that is 12 in scattered intensity with GO. We find that the agreement is very satisfactory in general. However, a discrepancy

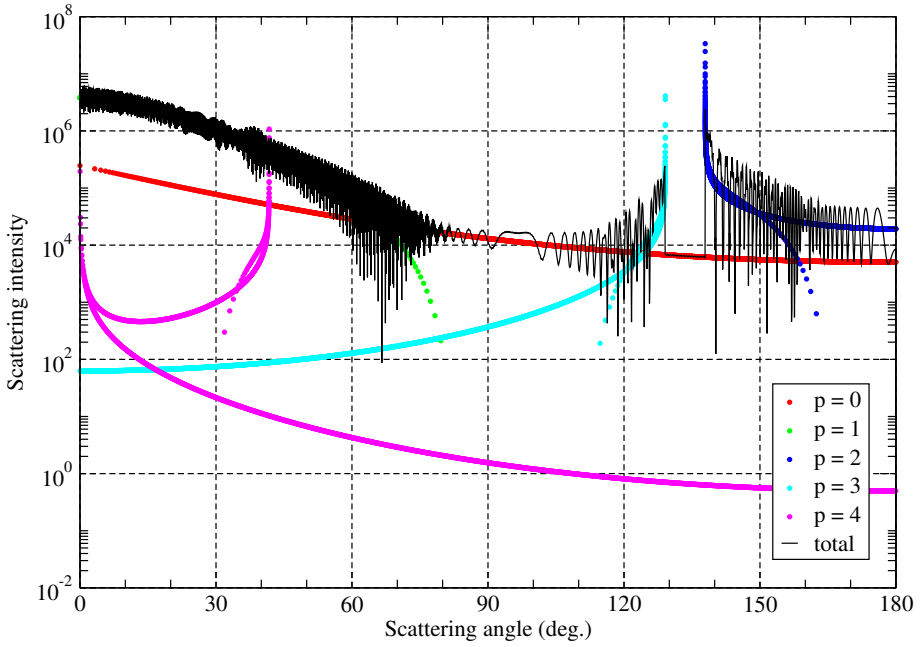

(a) Perpendicular polarization

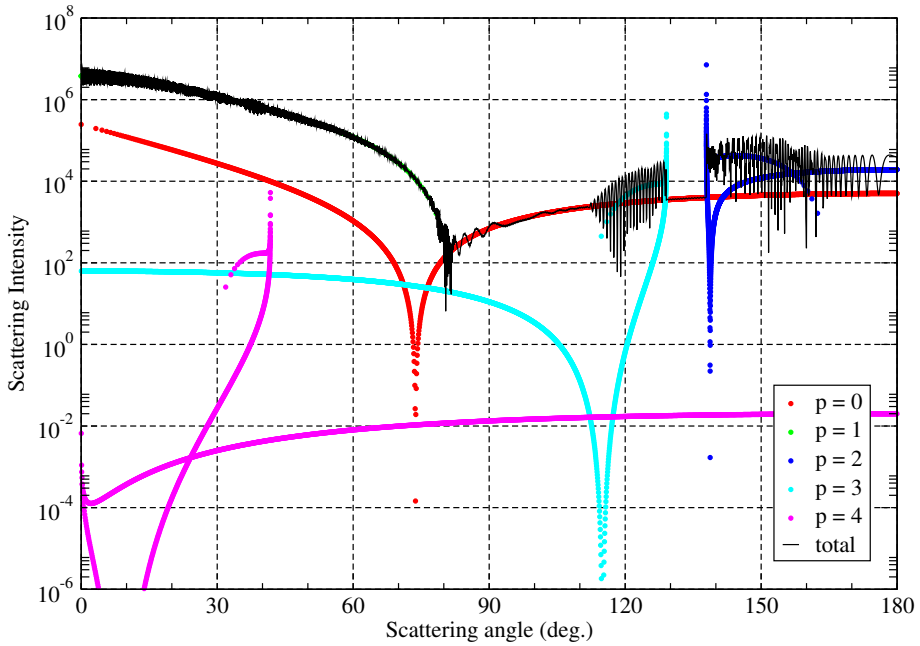

(b) Parallel polarization

Figure 2.8: Scattered intensity of each order of rays and the total intensity (plane wave $\lambda = 0.6328$ μm, sphere: $m = 1.333$ and $a = 100$ μm).

is clearly visible near the rainbow angles and around 90°, especially for the parallel polarization.

We would note also that the first and the second rainbows are less remarkable for the parallel polarization than for the perpendicular polarization. This can be explained by the fact that minimum reflection at Brewster angle is near the rainbow angles, notably for the first rainbow (cf. Fig. 2.9 (b)).

To examine the lower limit of the GO, we compare in Fig. 2.10 the scattering diagrams calculated by the GO and LMT for a particle of radius 20 μm. The order of the ray, the refractive index of the particle and the wavelength are the same as in Fig. 2.9. The discrepancy is evidently more important but the agreement is not so bad. If we focus our attention to the structure of the first rainbow for the perpendicular polarization out of the Alexander region, the fine structure of the GO is in very good agreement with that of the LMT. This is important for the refractometry of rainbow.

2.3 Conclusion

In this chapter, some fundamentals of geometrical optics are recalled. The formulation of the classic geometrical optics (GO) for the light scattering of a plane wave by a sphere is presented in details. Then, the ray tracing and the scattered intensity of individual order of ray are given to understand the mechanism of the light scattering. By the comparison of the scattering diagrams calculated by GO with LMT, we have shown that the GO permits to deal with the scattering of large particles (diameter larger than about 50 times the wavelength) and the accuracy is sufficiently good in general if the size of the sphere is large enough. In certain cases (depending on the polarization state, scattering region ...), the accuracy may be almost perfect or not good enough.

However, the formalism of GO for the scattering of a sphere can not be extended to a non-spherical particle. For an irregularly shaped particle, the incident angle (so the refraction angle) and the curvature of the particle surface change at each interaction. The Fresnel coefficients are to be calculated at each interaction point. And especially, it is very difficult to take into account the divergence/convergence of a wave on the particle surface.

The new models presented in the next chapter: Vectorial Complex Ray Model(VCRM) and Statistic Vectorial Complex Ray Model(SVCRM), are aimed to overcome this difficulty. It will be used latter for the scattering of a plane wave by a pendent droplet in three dimensions in chapter 5.

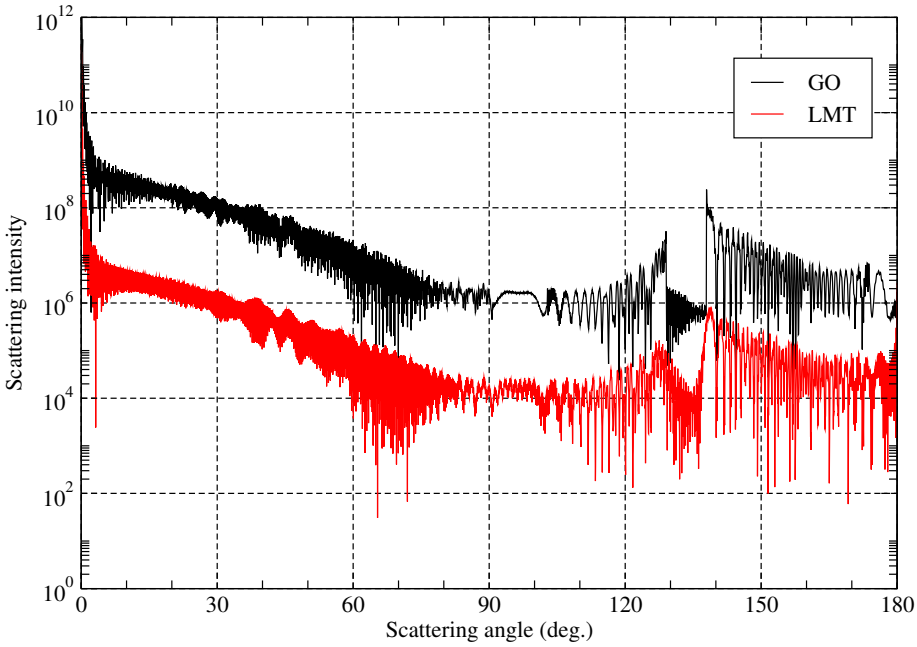

(a) Perpendicular polarization.

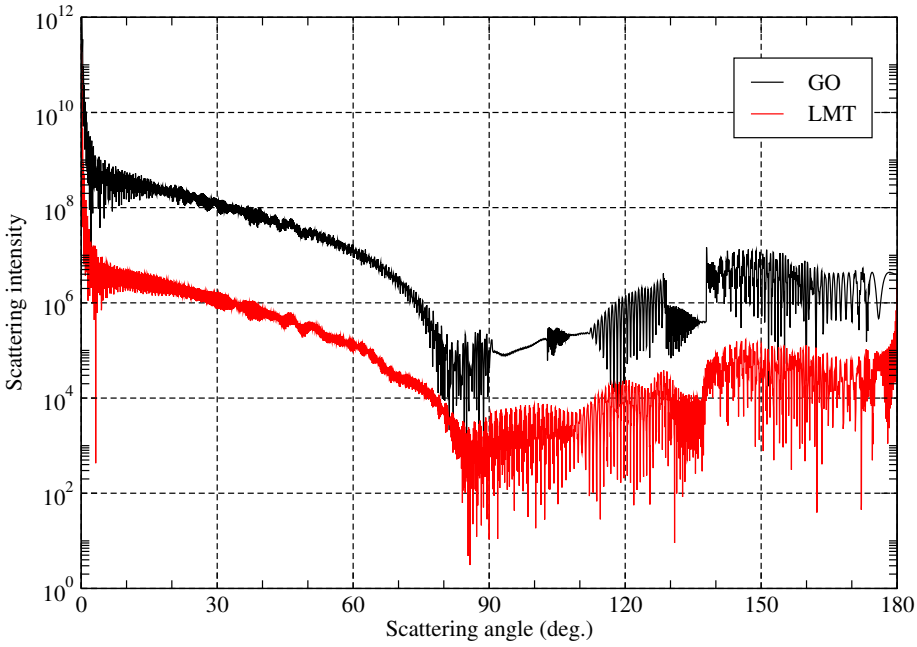

(b) Parallel polarization.

Figure 2.9: Scattering diagrams simulated by GO for a sphere ($m = 1.333$ and $a = 100\ \mu$m) by a plane wave of wavelength $\lambda = 0.6328\ \mu$m with various polarization states

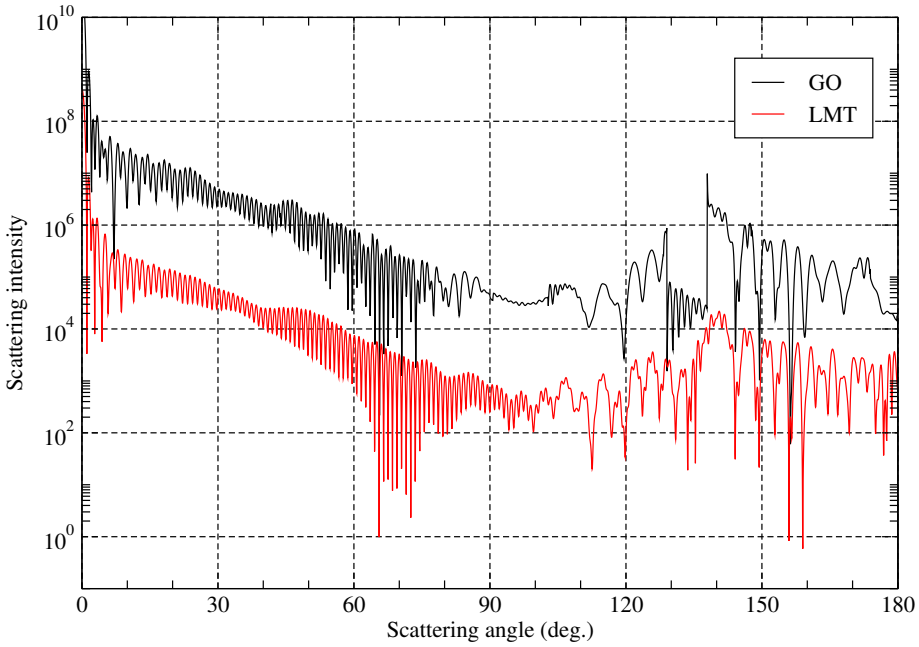

(a) Perpendicular polarization.

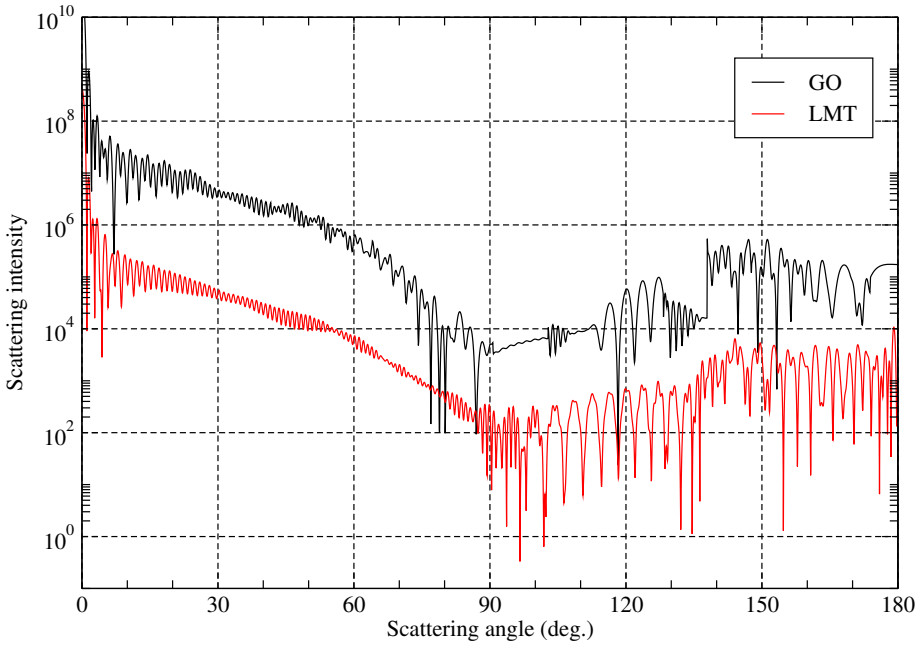

(b) Parallel polarization.

Figure 2.10: Scattering diagrams simulated by GO for a sphere ($m = 1.333$ and $a = 20\ \mu$m) by a plane wave of wavelength $\lambda = 0.6328\ \mu$m with various polarization states

Chapter 3

Vectorial Complex Ray Model and Statistic Vectorial Complex Ray Model

We have shown in the previous chapter that the Geometrical optics (GO) can predict the scattering of plane wave by a large sphere. But it is very difficult or impossible to extent to the scattering of the particles that have no circular or spherical symmetry because the divergence factor and the phase shift due to the focal lines cannot be calculated analytically. In fact, there is no parameter in the classical GO to describe the divergence or convergence of a wave. In order to solve this problem, the Vectorial Complex Ray Model (VCRM)[36, 54, 55] has been developed in our laboratory, in which the wave front curvature is introduced to describe this wave property. Furthermore, the rays in VCRM are expressed in vectors, which facilitates considerably the calculation.

The VCRM has been validated numerically [39] and experimentally [40] in the case of scattering of a plane wave by an ellipsoidal particle in a symmetric plane. In principle, VCRM can be applied to the scattering of a particle of any shape with smooth surface, if the function describing the particle surface is derivable to the second order so that the curvature exists. And it is not difficult to calculate the complex amplitude of each emergent ray. The problem is that the directions of the emergent rays are not regularly distributed along the scattering angles (θ, ϕ). To calculate the complex amplitude of the total scattered field at a given direction, we must know the complex amplitude of each ray arriving in that direction. This can be realized by a two dimension interpolation from a irregular distributed data, even if it is not an easy task.

To get over this obstacle, we develop an alternative algorithm for scattering of the three-dimensional non-spherical particles. Instead of the calculation of the complex amplitude in a given direction, we count statistically the complex amplitude of all the emergent rays in a small box, this algorithm is called hereafter Statistic Vectorial Complex Ray Model (SVCRM) [41].

In this chapter, we will present firstly the principle of VCRM, and then give a detailed description of the SVCRM.

3.1 Vectorial Complex Ray Model

In VCRM, all waves are described by bundles of rays where each ray is characterized by its propagation direction $\hat{\boldsymbol{k}}$, its polarization X, its phase σ_p, its amplitude $A_{X,p}$ as well as its wave front curvature matrix $\mathbf{Q}$ [36, 56].

3.1.1 Directions of rays and Fresnel formulas

The propagation direction of a ray is described by its wave vector. It is much more convenient for the numerical calculation for the scattering of particles of any shape since only four basic operations are necessary to determine the directions of reflected and refracted rays, and the Fresnel coefficients.

The Snell-Descartes law is written in vector form in VCRM [36]:

$$(\boldsymbol{k'} - \boldsymbol{k}) \times \hat{\boldsymbol{n}} = 0 \tag{3.1}$$

where $\boldsymbol{k'}$ and $\boldsymbol{k}$ are respectively the wave vectors before and after interaction of the ray with the particle surface, and $\hat{\boldsymbol{n}}$ is the normal of the surface.

In fact, Eq. (3.1) reveals simply that the tangent component of the wave vector on the interface of a particle is continuous [38]. This means that the Snell-Descartes law can be written explicitly as:

$$k'_\tau = k_\tau \tag{3.2}$$

where the subscript τ indicates the tangent component of the vector. So Eq. (3.2) can be further expressed as

$$k_\tau^{(i)} = k_\tau^{(r)} = k_\tau^{(t)} \tag{3.3}$$

The normal component of the wave vector [38], which is not continuous, can be obtained simply by

$$\begin{aligned} k_n^{(r)} &= -\sqrt{{k^{(r)}}^2 - {k_\tau^{(i)}}^2} \\ k_n^{(t)} &= \sqrt{{k^{(t)}}^2 - {k_\tau^{(i)}}^2} \end{aligned} \tag{3.4}$$

where $k_n^{(r)}$ is the normal component of the reflected wave vector, the minus sign means that the normal component of the reflected ray is in the opposite direction of the

incident ray. $k_n^{(t)}$ is the normal component of the refracted wave vector. The propagation directions of the emerging rays [57] are given by:

$$\begin{aligned} \boldsymbol{k^{(r)}} &= k_\tau^{(r)}\hat{\boldsymbol{\tau}} + k_n^{(r)}\hat{\boldsymbol{n}} \\ \boldsymbol{k^{(t)}} &= k_\tau^{(t)}\hat{\boldsymbol{\tau}} + k_n^{(t)}\hat{\boldsymbol{n}} \end{aligned} \tag{3.5}$$

To be convenient and consistent with VCRM, the Fresnel formulas are written as functions of the normal components of the wave vectors of the incident, the reflected and the refracted waves [58]:

$$\begin{aligned} r_\parallel &= \frac{m^2 k_n^{(i)} - k_n^{(r)}}{m^2 k_n^{(i)} + k_n^{(r)}} \\ r_\perp &= \frac{k_n^{(i)} - k_n^{(r)}}{k_n^{(i)} + k_n^{(r)}} \\ t_\parallel &= \frac{2m k_n^{(i)}}{m^2 k_n^{(i)} + k_n^{(t)}} \\ t_\perp &= \frac{2k_n^{(i)}}{k_n^{(i)} + k_n^{(t)}} \end{aligned} \tag{3.6}$$

with $k_n^{(r)} = k_n^{(i)} = \boldsymbol{k}^{(i)} \cdot \hat{\boldsymbol{n}} = k_0 \cos\theta_i$, $k_n^{(t)} = \boldsymbol{k}^{(t)} \cdot \hat{\boldsymbol{n}} = m k_0 \cos\theta_t$. Here, θ_i is the incident angle and θ_t the refraction angle.

When the tangent component of the incident wave vector is greater than the wave number of the refracted wave (when a ray goes from an optically denser medium to an optically looser medium), the total reflection occurs. In this case, the normal component of the wave becomes a pure imaginary number if the two media are both transparent. The Fresnel reflection coefficients can be written as [59]

$$\begin{aligned} r_\parallel &= \frac{m^2 k_n^{(i)} - i\sqrt{{k_\tau^{(i)}}^2 - {k^{(r)}}^2}}{m^2 k_n^{(i)} + i\sqrt{{k_\tau^{(i)}}^2 - {k^{(r)}}^2}} \\ r_\perp &= \frac{k_n^{(i)} - i\sqrt{{k_\tau^{(i)}}^2 - {k^{(r)}}^2}}{k_n^{(i)} + i\sqrt{{k_\tau^{(i)}}^2 - {k^{(r)}}^2}} \end{aligned} \tag{3.7}$$

They become complex numbers. The phase shifts of the rays due to the reflection and refraction vary with the incident angle of the rays.

3.1.2 Wave front equation

When a wave propagates, it can be diverging, converging or plane. Two curvatures along on the final directions can be associated with this wave. When a wave interacts

with a particle, the reflected/refracted wave will be converged or diverged according to the curvature of the particle surface. To describe this property, the wave front curvature is introduced in VCRM as a new property of a ray [36, 55, 54].

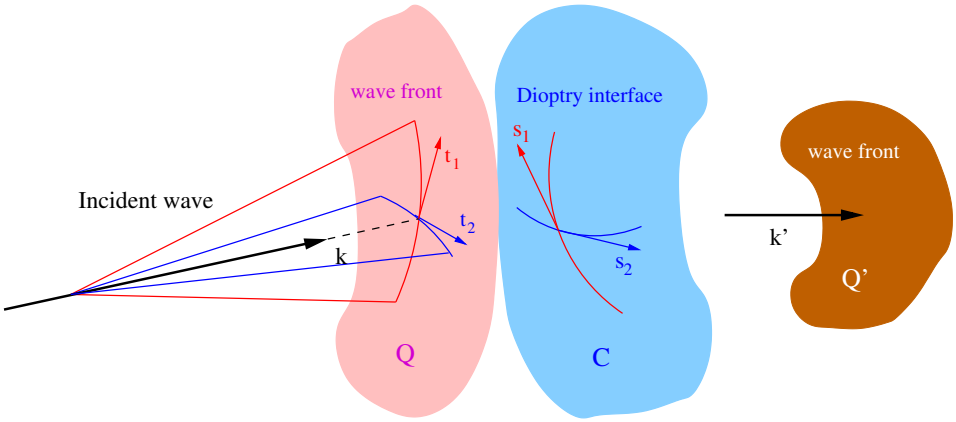

Figure 3.1: Schematic diagram of the wave fronts of the waves before and after interaction and the dioptry particle surface

In terms of mathematics, the structure of any smooth surface in the vicinity of a given point can be described by a 2×2 matrix [56]. The curvature matrix of a surface is defined as follows. Let $\boldsymbol{t_1}$ and $\boldsymbol{t_2}$ be an orthonormal basis of the tangent plane at a surface point. $\boldsymbol{n}$ is the normal vector at the surface point. $\boldsymbol{t}$ is any direction in the tangent plane: $\boldsymbol{t} = \alpha_1 \boldsymbol{t_1} + \alpha_2 \boldsymbol{t_2}$, the curvature along $\boldsymbol{t}$ is the second derivative of the curve $x(t)$ in the plane $(\boldsymbol{n}, \boldsymbol{t})$. The curvature matrix is

$$\mathbf{Q} = \begin{bmatrix} \kappa_{11} & \kappa_{12} \\ \kappa_{21} & \kappa_{22} \end{bmatrix} \tag{3.8}$$

defined by

$$\kappa_p(t) = \begin{bmatrix} \alpha_1 \\ \alpha_2 \end{bmatrix}^T \begin{bmatrix} \kappa_{11} & \kappa_{12} \\ \kappa_{21} & \kappa_{22} \end{bmatrix} \begin{bmatrix} \alpha_1 \\ \alpha_2 \end{bmatrix} \tag{3.9}$$

If $\boldsymbol{t_1}$ and $\boldsymbol{t_2}$ are the principal directions, $\mathbf{Q}$ is diagonal. Definition of wave curvature is similar, by using wave front instead of the surface.

Considering an arbitrary wave whose wave front curvature at the incident point is described by the curvature matrix $\mathbf{Q}$ in the basis $(\boldsymbol{t_1}, \boldsymbol{t_2})$, the curvature matrix of the dioptric surface $\mathbf{C}$ in basis $(\boldsymbol{s_1}, \boldsymbol{s_2})$ and the curvature matrix of the refraction or reflection wave $\mathbf{Q'}$ in basis $(\boldsymbol{t'_1}, \boldsymbol{t'_2})$, the evolution of the wave front curvature at each interaction point can be described by the wave front equation [36]:

$$(\boldsymbol{k'} - \boldsymbol{k}) \cdot \boldsymbol{n}\mathbf{C} = k' \boldsymbol{\Theta'}^{\boldsymbol{T}} \mathbf{Q'} \boldsymbol{\Theta'} - k \boldsymbol{\Theta}^{\boldsymbol{T}} \mathbf{Q} \boldsymbol{\Theta} \tag{3.10}$$

where $\boldsymbol{n}$ is the normal of the dioptric surface, $\boldsymbol{k}$ and $\boldsymbol{k'}$ are the wave vectors of the rays before and after interaction, k and k' are the corresponding wave numbers. The index T denotes the transposition of the matrix. In addition, $\boldsymbol{\Theta}$ and $\boldsymbol{\Theta'}$ are the projection matrices of the basis $(\boldsymbol{t_1}, \boldsymbol{t_2})$ and $(\boldsymbol{t'_1}, \boldsymbol{t'_2})$ on the basis $(\boldsymbol{s_1}, \boldsymbol{s_2})$ respectively, which can be expressed as:

$$\begin{aligned} \boldsymbol{\Theta} &= \begin{bmatrix} \boldsymbol{s_1} \cdot \boldsymbol{t_1} & \boldsymbol{s_1} \cdot \boldsymbol{t_2} \\ \boldsymbol{s_2} \cdot \boldsymbol{t_1} & \boldsymbol{s_2} \cdot \boldsymbol{t_2} \end{bmatrix} \\ \boldsymbol{\Theta'} &= \begin{bmatrix} \boldsymbol{s_1} \cdot \boldsymbol{t'_1} & \boldsymbol{s_1} \cdot \boldsymbol{t'_2} \\ \boldsymbol{s_2} \cdot \boldsymbol{t'_1} & \boldsymbol{s_2} \cdot \boldsymbol{t'_2} \end{bmatrix} \end{aligned} \tag{3.11}$$

When $(\boldsymbol{t_1}, \boldsymbol{t_2})$ and $(\boldsymbol{t'_1}, \boldsymbol{t'_2})$ are the principal curvature directions of the wave front before and after interaction and $(\boldsymbol{s_1}, \boldsymbol{s_2})$ are the principal curvature directions of the dioptric surface, the corresponding curvature matrix is diagonal.

If the scattering takes place in a symmetric plane and one of the principal direction of the incident wave front as well as those of the reflected and refracted waves are in the direction perpendicular to the symmetric plane, the matrices $\mathbf{Q}$, $\mathbf{Q'}$ and $\mathbf{C}$ are diagonal and may be written as:

$$\begin{aligned} \mathbf{Q} &= \begin{bmatrix} \dfrac{1}{R_1} & 0 \\ 0 & \dfrac{1}{R_2} \end{bmatrix} \\ \mathbf{Q'} &= \begin{bmatrix} \dfrac{1}{R'_1} & 0 \\ 0 & \dfrac{1}{R'_2} \end{bmatrix} \\ \mathbf{C} &= \begin{bmatrix} \dfrac{1}{\rho_1} & 0 \\ 0 & \dfrac{1}{\rho_2} \end{bmatrix} \end{aligned} \tag{3.12}$$

where R_1, R_2 and R'_1, R'_2 are the principal curvature radii of the wave front before and after interaction and ρ_1, ρ_2 are the principal curvature radii of the particle surface at the interaction point.

Supposed that $\boldsymbol{s_2}$ and $\boldsymbol{t_2}$ are in the incident plane. It means $\boldsymbol{s_1} \cdot \boldsymbol{t_1} = 1$ and $\boldsymbol{s_2} \cdot \boldsymbol{t_2} = \cos\theta_i$. Similar relations can be applied to the refracted wave. The wave front equation (3.10) is simplified to two scalar equations. The relation between the curvature radii in the plane perpendicular to the incident plane is given by:

$$\frac{k'}{R'_1} = \frac{k}{R_1} + \frac{k'_n - k_n}{\rho_1} \tag{3.13}$$

and the relation of the curvature radii in the incident plane is expressed as:

$$\frac{k_n'^{\,2}}{k' R_2'} = \frac{k_n^2}{R_2} + \frac{k_n' - k_n}{\rho_2} \tag{3.14}$$

It is important to note that if ρ_1 is not infinite the wave front curvature in the direction perpendicular to the scattering plane evolves also at each interaction with the particle surface.

3.1.3 Amplitude of a ray

The amplitude of a ray may change during the propagation due to the convergence and divergence of the waves. In the scattering of a plane wave by a sphere, the divergence factor has been obtained analytically to describe the variation of the amplitude of the ray. In the framework of VCRM, the divergence factor can be calculated step by step according to the wave front curvature for particle of any shape [58].

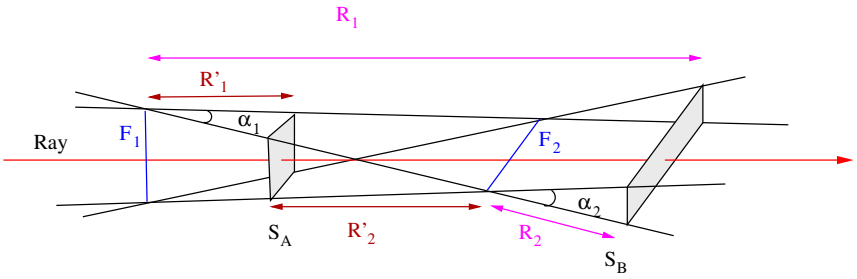

Figure 3.2: Variation of pencil cross section

Consider a wave propagating from point A to point B (Fig. 3.2). Suppose that two orthogonal focal lines are F_1 and F_2. Then the curvature radii at A and B corresponding to F_1 are, respectively, R_1' and R_1 and the curvature radii at A and B relative to F_2 are, respectively, R_2' and R_2. The relation between the intensities at points A and B along a ray can be deduced from the energy conservation, i.e. the energy flux passing through the surface $S_A = R_1'\alpha_1 R_2'\alpha_2$ is equal to that through the surface $S_B = R_1\alpha_1 R_2\alpha_2$. That is $I_A R_1'\alpha_1 R_2'\alpha_2 = I_B R_1\alpha_1 R_2\alpha_2$. Consequently we obtain the relation between the intensities at A and B:

$$\frac{I_B}{I_A} = \left| \frac{R_1' R_2'}{R_1 R_2} \right| \tag{3.15}$$

which indicates that the ratio of the intensities at two successive points A and B is proportional to ratio of their Gauss curvature (the product of the two principal curvatures) of the wave front.

Now, we consider the variation of the intensity in the scattering of a particle. The intensity of the reflected wave by the external surface (the first interaction) is the

product of the intensity of the incident wave I_0 and the reflectivity $\mid r_{X,0} \mid^2$. The two radii of the reflected wave front at the reflection point are noted by R'_{10} and R'_{20}, and those of the reflected wave at distance r are $(r - R'_{10})$ and $(r - R'_{20})$. Then the scattered intensity at distance r can be expressed as:

$$I(r) = I_0 \mid r_{X,0} \mid^2 \left| \frac{R'_{10} R'_{20}}{(r - R'_{10})\,(r - R'_{20})} \right| \tag{3.16}$$

Similarly, the intensity of the scattered light of order $p = 1$ can be calculated by:

$$I(r) = I_0 \mid t_{X,0} t_{X,1} \mid \left| \frac{R'_{10} R'_{20}}{R_{11} R_{21}} \cdot \frac{R'_{11} R'_{21}}{(r - R'_{11})\,(r - R'_{21})} \right| \tag{3.17}$$

where $t_{X,0}$ and $t_{X,1}$ are the Fresnel coefficients of refraction for the order $p = 0$ and $p = 1$.

Generally, the two curvature radii of the incident wave front at q^{th} interaction point are noted by R_{1q} and R_{2q}. R'_{1q} and R'_{2q} are the corresponding curvature radii of the refracted ray. Then, the intensity of the emergent ray after q interactions with the particle surface can be expressed as:

$$I(r) = I_0 \mid \varepsilon_{X,p} \mid^2 \mid \mathfrak{D}_v \mid \tag{3.18}$$

where $p = q - 1$, $\mathfrak{D}_v$ is the divergence factor defined by

$$\mathfrak{D}_v = \frac{R'_{10} R'_{20}}{R_{11} R_{21}} \cdot \frac{R'_{11} R'_{21}}{R_{12} R_{22}} \cdots \frac{R'_{1p} R'_{2p}}{(r - R'_{1p})(r - R'_{2p})} \tag{3.19}$$

$\varepsilon_{X,p}$ is the amplitude ratio of the p^{th} order ray and the incident ray for polarization X and given as function of the Fresnel coefficients by:

$$\varepsilon_{X,p} = \begin{cases} r_{X,0} & p = 0 \\ t_{X,0} t'_{X,p} \displaystyle\prod_{n=1}^{p-1} r_{X,n} & p \geq 1 \end{cases} \tag{3.20}$$

It should be noted that the reflection coefficient $r_{X,0}$ is for the first external reflection while the $r_{X,n}$ is for the internal reflection.

In our study, we are interested only in the scattering in far field. The term $(r - R'_{1p})(r - R'_{2p})$ in Eq. (3.19) tends to r^2 in far field and often omitted in the calculation of scattering diagrams and we note $\mathfrak{D}_v = D_v / r^2$. Thus, the complex amplitude of an emergent ray of order p with X polarization is calculated by

$$\tilde{A}_{X,p} = \sqrt{\mid D_v \mid} A_{0,X} \mid \varepsilon_{X,p} \mid e^{i\sigma_{X,p}} \tag{3.21}$$

where the divergence factor D_v is given by:

$$D_v = \frac{R'_{10} R'_{20}}{R_{11} R_{21}} \cdot \frac{R'_{11} R'_{21}}{R_{12} R_{22}} \cdots R'_{1p} R'_{2p} \tag{3.22}$$

The calculation of the phase $\sigma_{X,p}$ will be discussed in the following section.

3.1.4 Phase of a ray

The phase of rays plays a critical role in counting the wave effect in the light scattering diagrams by taking the interference phenomenon into consideration, such as the fringes in the (rain)bows of each order or the interference structure near different kinds of caustics. The phase σ of a ray in VCRM is easy to count.

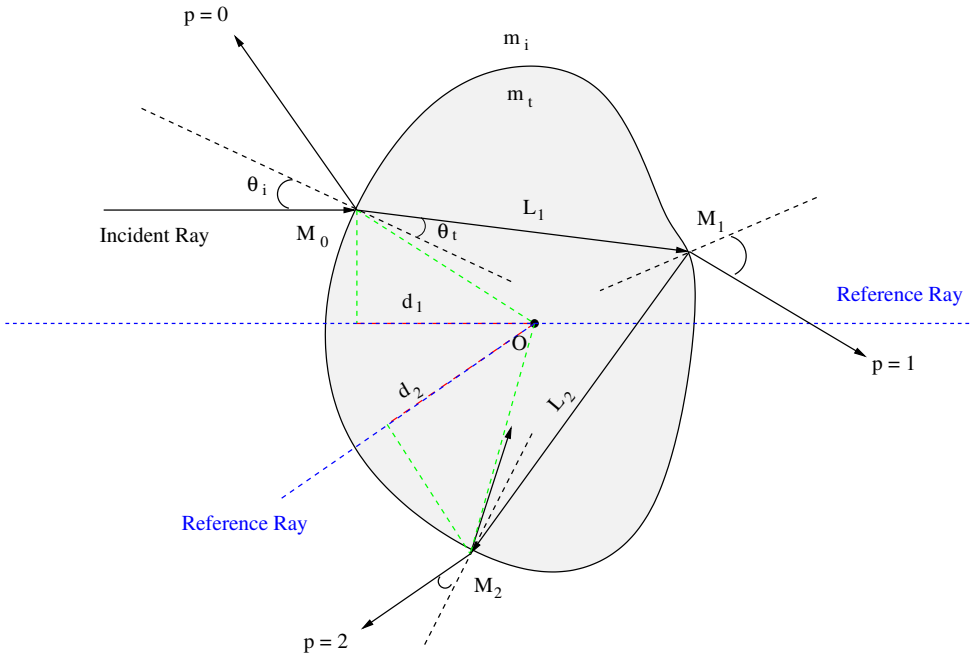

Figure 3.3: Schematic diagram of interactions between a ray and an irregular particle.

The phase of an emergent ray consists of four parts:

- Phase of the incident ray $\sigma_{X,0}$

  The first part concerns the phase of the incident wave, which is determined by the properties of the incident wave. In the scattering of a plane wave by a pendent droplet, the phase of the incident rays is constant and we take $\sigma_{X,0} = 0$ in the calculation.

- Phase shifts induced by Fresnel coefficients $\sigma_{F,X,p}$

  The phase shift due to the reflection/refraction is calculated directly according to the Fresnel coefficient as described in the previous chapter. For a transparent particle, if no total reflection occurs, only a phase shift π is to be added to the reflected ray for the perpendicular polarization at any incident angle and for the parallel polarization if the incident angle is larger than the Brewster angle. There is no phase shift for the refracted ray whatever the polarization state. When the total reflection occurs, the phase shifts of the reflection/refraction ray depend on the incident angle and to be calculated by Eq. (2.10) to both polarizations.

- Phase shift due to optical path $\sigma_{P,p}$

  The phase shift due to the optical path is computed directly according to the optical path relative to a reference ray arriving at the center of the particle in the same direction as the incident ray and outgoing in the same direction as the emergent ray.

  Let $\boldsymbol{r}_q$ and $\hat{\boldsymbol{k}}_q$ be respectively the position vector of q^{th} interaction point of the ray with the particle surface and the normalized wave vector of the emergent ray from that point, the phase due to the optical path of a ray after q interactions with the particle is given by

$$\sigma_{P,p} = -k_0 \left(\hat{\boldsymbol{k}}_i \cdot \boldsymbol{r}_1 - \hat{\boldsymbol{k}}_q \cdot \boldsymbol{r}_q \right) - k_p \sum_{q=1}^{p} \hat{\boldsymbol{k}}_{q-1} \cdot (\boldsymbol{r}_q - \boldsymbol{r}_{q-1}) \tag{3.23}$$

  where $\hat{\boldsymbol{k}}_i$ is the normalized wave vector of the incident ray. The first part in this equation is the phase shift of the due to the path difference outside of the particle and the second part is the total optical path inside the particle.

- Phase shift due to focal lines/points

  As for the phase shift due to the focal lines, it is easy to be calculated in VCRM, because we need only to count the number of the changes of the signs of the wave front curvature radii N_f during its successive interactions of a ray with the particle surface until emergent to infinite. The phase shift due to focal lines is then

$$\sigma_f = \frac{\pi}{2} \cdot N_f \tag{3.24}$$

  This phase shift is dependent of the polarization state of the incident wave.

Finally, the phase of a X polarized ray of order p can be expressed as:

$$\sigma_{X,p} = \sigma_{X,0} + \sigma_{F,X,p} + \sigma_{P,p} + \sigma_{f,p} \tag{3.25}$$

This is essential to predict the interference of the scattered wave when the particle is illuminated by a coherent light.

3.1.5 Scattering intensity

Knowing the amplitude and the phase of each emergent ray, we can calculate the complex amplitude of each emergent ray in the same manner as in the GO for the scattering of a plane wave by a sphere, i.e.

$$\tilde{A}_{X,i}(\theta, \phi) = A_{X,0} \mid \varepsilon_{X,i} \mid \sqrt{\mid D_v \mid} e^{i\sigma_{X,i}} \tag{3.26}$$

where $A_{X,0}$ stands for the amplitude of the incident wave with the polarization state X. The index i denotes the i^{th} ray arriving in the direction (θ, ϕ). It should be noted that D_{sp} is replaced by D_v and there is no size parameter in Eq. (3.26) (compared to Eq. (2.37), since we cannot define precisely a size parameter for a particle of arbitrary shape and the dimension of the particle is included already in the divergence factor. The remarks after Eq. (2.37) concerning (1) the number of rays, (2) the prefactor $1/(kr)^2$, (3) calculation of the total complex amplitude in a given direction and (4) the total scattered intensity for spherical particle are valid also for an arbitrarily shaped particle in VCRM.

As stated at the beginning of this chapter, it is very difficulty to calculate the total complex amplitude at a given direction according to Eq. (2.37) since a two dimension interpolation on irregular data is necessary. The Statistic Vectorial Complex Ray Model permits to get around this obstacle and will be presented in details in the following section.

3.2 Statistic Vectorial Complex Ray Model

In the Statistic Vectorial Complex Ray Model (SVCRM), the light wave is presented by photons having the same properties of rays in VCRM [41]. It is more vividly to represent the physical properties in statistics by inducing the concept of photons. The phase of each photon is calculated in the same manner as in VCRM. The ratio of the amplitude of the scattered wave to the incident one due to the reflection and the refraction, i.e. the factor ε_X, is calculated step by step according to Eq. (3.20), while the variation of the amplitude of the scattered wave due to divergence and convergence by the curvature of the particle surface will not be calculated by the divergence factor but taken into account by the number of photons arriving in a collection unit. The calculation of the wave front is still necessary to count the phase shift due to the focal lines.

3.2.1 Four coordinate bases

In the scattering of light by a particle of arbitrary shape, the direction of the incident plane, the polarization state of a wave, the principal directions of the particle surface and those of the wave front change at each interaction. To describe these properties we need to define four basis, i.e. four normalized orthogonal basis at a given interaction point.

We note the normal of the particle surface at a given interaction point by $\hat{\boldsymbol{n}}$, which is oriented from the incident medium to the medium where the transmission takes place. The incidence plane is the plane defined by the propagation direction of the incident

wave $\boldsymbol{k}^{(i)}$ and the normal to the surface $\hat{\boldsymbol{n}}$. Then, four basis will be introduced, and the propagation directions of the reflected/refracted waves and the polarization states will be expressed in these basis.

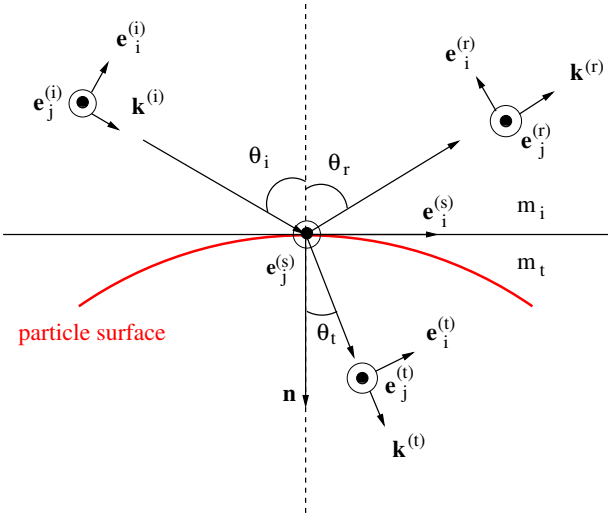

Figure 3.4: Definition of the direction of various components in Snell-Descartes Laws

- Basis of particle surface

  First, we define the unit vector $\hat{\boldsymbol{e}}_{\boldsymbol{j}}^{(\boldsymbol{s})}$ perpendicular to the incidence plane, which can be expressed by the wave vector of the incident wave $\hat{\boldsymbol{k}}^{(\boldsymbol{i})}$ and the normal to the particle surface $\hat{\boldsymbol{n}}$:

$$\hat{\boldsymbol{e}}_{\boldsymbol{j}}^{(\boldsymbol{s})} = \frac{\hat{\boldsymbol{n}} \times \hat{\boldsymbol{k}}^{(\boldsymbol{i})}}{\left\| \hat{\boldsymbol{n}} \times \hat{\boldsymbol{k}}^{(\boldsymbol{i})} \right\|} \tag{3.27}$$

  Then the unit vector $\hat{\boldsymbol{e}}_{\boldsymbol{i}}^{(\boldsymbol{s})}$ parallel to the incident plane and perpendicular to $\hat{\boldsymbol{e}}_{\boldsymbol{j}}^{(\boldsymbol{s})}$ is given by:

$$\hat{\boldsymbol{e}}_{\boldsymbol{i}}^{(\boldsymbol{s})} = \frac{\hat{\boldsymbol{e}}_{\boldsymbol{j}}^{(\boldsymbol{s})} \times \hat{\boldsymbol{n}}}{\left\| \hat{\boldsymbol{e}}_{\boldsymbol{j}}^{(\boldsymbol{s})} \times \hat{\boldsymbol{n}} \right\|} \tag{3.28}$$

  So the basis of the particle surface is defined by $(\hat{\boldsymbol{e}}_{\boldsymbol{i}}^{(\boldsymbol{s})}, \hat{\boldsymbol{e}}_{\boldsymbol{j}}^{(\boldsymbol{s})}, \hat{\boldsymbol{n}})$.

- Basis of incident rays

  Then, the basis of the incident ray is defined according to the normalized wave vector of the incident wave $\hat{\boldsymbol{k}}^{(i)}$ and the normal of the incident plane $\hat{\boldsymbol{e}}_{\boldsymbol{j}}^{(\boldsymbol{s})}$, but noted here by $\hat{\boldsymbol{e}}_{\boldsymbol{j}}^{(\boldsymbol{i})}$ for convenience. The third basis vector is defined by

$$\hat{\boldsymbol{e}}_{\boldsymbol{i}}^{(\boldsymbol{i})} = \frac{\hat{\boldsymbol{e}}_{\boldsymbol{j}}^{(\boldsymbol{i})} \times \hat{\boldsymbol{k}}^{(\boldsymbol{i})}}{\left\| \hat{\boldsymbol{e}}_{\boldsymbol{j}}^{(\boldsymbol{i})} \times \hat{\boldsymbol{k}}^{(\boldsymbol{i})} \right\|} \tag{3.29}$$

The basis of incident ray is therefore $(\hat{\boldsymbol{e}}_{\boldsymbol{i}}^{(\boldsymbol{i})}, \hat{\boldsymbol{e}}_{\boldsymbol{j}}^{(\boldsymbol{i})}, \hat{\boldsymbol{k}}^{(\boldsymbol{i})})$.

- Basis of reflected rays

  Similarly, the basis of the reflected ray is defined according to the normalized wave vector of reflected ray $\hat{\boldsymbol{k}}^{(r)}$ and the normal of the incident plane $\hat{\boldsymbol{e}}_{\boldsymbol{j}}^{(\boldsymbol{s})}$, also noted by $\hat{\boldsymbol{e}}_{\boldsymbol{j}}^{(\boldsymbol{r})}$ for convenience. The third basis vector is defined by

$$\hat{\boldsymbol{e}}_{\boldsymbol{i}}^{(\boldsymbol{r})} = \frac{\hat{\boldsymbol{e}}_{\boldsymbol{j}}^{(\boldsymbol{r})} \times \hat{\boldsymbol{k}}^{(\boldsymbol{r})}}{\left\| \hat{\boldsymbol{e}}_{\boldsymbol{j}}^{(\boldsymbol{r})} \times \hat{\boldsymbol{k}}^{(\boldsymbol{r})} \right\|} \tag{3.30}$$

  The basis of the reflected ray is then $(\hat{\boldsymbol{e}}_{\boldsymbol{i}}^{(\boldsymbol{r})}, \hat{\boldsymbol{e}}_{\boldsymbol{j}}^{(\boldsymbol{r})}, \hat{\boldsymbol{k}}^{(\boldsymbol{r})})$.

- Basis of refracted rays

  Finally, the basis of the refracted ray $(\hat{\boldsymbol{e}}_{\boldsymbol{i}}^{(\boldsymbol{t})}, \hat{\boldsymbol{e}}_{\boldsymbol{j}}^{(\boldsymbol{t})}, \boldsymbol{k}^{(\boldsymbol{t})})$ is defined in the same manner, where $\hat{\boldsymbol{e}}_{\boldsymbol{j}}^{(\boldsymbol{t})} = \hat{\boldsymbol{e}}_{\boldsymbol{j}}^{(\boldsymbol{s})}$ and

$$\hat{\boldsymbol{e}}_{\boldsymbol{i}}^{(\boldsymbol{t})} = \frac{\hat{\boldsymbol{e}}_{\boldsymbol{j}}^{(\boldsymbol{t})} \times \boldsymbol{k}^{(\boldsymbol{t})}}{\left\| \hat{\boldsymbol{e}}_{\boldsymbol{j}}^{(\boldsymbol{t})} \times \boldsymbol{k}^{(\boldsymbol{t})} \right\|} \tag{3.31}$$

These four basis will be used in the following calculation.

3.2.2 Curvature matrix

In general, at an interaction point of a ray with the particle surface, the curvature matrix of the dioptric surface $\mathbf{C}$, the wave front curvature matrix of the incident wave $\mathbf{Q}^{(\boldsymbol{i})}$, the reflected wave $\mathbf{Q}^{(\boldsymbol{r})}$ and the refracted $\mathbf{Q}^{(\boldsymbol{t})}$ are not diagonal and can be expressed by 2×2 matrices, respectively, as:

$$\begin{aligned}
\mathbf{C} &= \begin{bmatrix} \kappa_{ii}^{(s)} & \kappa_{ij}^{(s)} \\ \kappa_{ij}^{(s)} & \kappa_{jj}^{(s)} \end{bmatrix} \\
\mathbf{Q}^{(\boldsymbol{i})} &= \begin{bmatrix} \kappa_{ii}^{(i)} & \kappa_{ij}^{(i)} \\ \kappa_{ij}^{(i)} & \kappa_{jj}^{(i)} \end{bmatrix} \\
\mathbf{Q}^{(\boldsymbol{r})} &= \begin{bmatrix} \kappa_{ii}^{(r)} & \kappa_{ij}^{(r)} \\ \kappa_{ij}^{(r)} & \kappa_{jj}^{(r)} \end{bmatrix} \\
\mathbf{Q}^{(\boldsymbol{t})} &= \begin{bmatrix} \kappa_{ii}^{(t)} & \kappa_{ij}^{(t)} \\ \kappa_{ij}^{(t)\prime} & \kappa_{jj}^{(t)} \end{bmatrix}
\end{aligned} \tag{3.32}$$

A curvature matrix is diagonal when it is given in its principal direction basis. The two elements in the diagonal are the two curvatures and their inverses are the two curvature radii. That means to find the curvature radii, the four curvature matrices in Eqs. (3.32) must be diagonalized. In that case, the four curvature matrices can be expressed, respectively, as:

$$\begin{aligned}
\mathbf{C} &= \begin{bmatrix} \kappa_1^{(s)} & 0 \\ 0 & \kappa_2^{(s)} \end{bmatrix} \\
\mathbf{Q^{(i)}} &= \begin{bmatrix} \kappa_1^{(i)} & 0 \\ 0 & \kappa_2^{(i)} \end{bmatrix} \\
\mathbf{Q^{(r)}} &= \begin{bmatrix} \kappa_1^{(r)} & 0 \\ 0 & \kappa_2^{(r)} \end{bmatrix} \\
\mathbf{Q^{(t)}} &= \begin{bmatrix} \kappa_1^{(t)} & 0 \\ 0 & \kappa_2^{(t)} \end{bmatrix}
\end{aligned} \tag{3.33}$$

Because the principal directions of the incident wave, of the surface, of the reflected wave and of the transmitted wave are not the same, a reference basis must be chosen to calculate the curvature evolution at surface interaction. We choose to define the ray by its two curvature $\kappa_1^{(i)}$ and $\kappa_2^{(i)}$ in its principal directions.

We choose also to compute the wave curvature evolution (Eq. (3.10)) in the basis of the incident plane $(\hat{\boldsymbol{e}}_{\boldsymbol{i}}^{(\boldsymbol{i})}, \hat{\boldsymbol{e}}_{\boldsymbol{j}}^{(\boldsymbol{i})}, \hat{\boldsymbol{k}}^{(\boldsymbol{i})})$. A rotation matrix is then used to computed $\mathbf{C}$ and $\mathbf{Q}$ is this reference basis. $\mathbf{Q}^{'}$ is then obtained for the reflected and the transmitted wave, as shown in Fig. 3.5.

Then, the two curvature radii R_1, R_2 of an emergent wave at a given interaction point can be calculated when their corresponding principal curvatures are known. The curvature radii R_1', R_2' of the incident wave at the next interaction point can be deduced from the distance l between the two successive points and these two curvature radii:

$$R_1' = R_1 - l \tag{3.34}$$

$$R_2' = R_2 - l \tag{3.35}$$

The curvature matrix of the incident wave at the new point obtained in such way is diagonal and expressed in its principal directions. After that, a series of matrix rotation start again, which are used to deal with the interaction between the incident ray and the object in the new incident plane.

Therefore, the mutual transformation between the matrices in Eq. (3.32) and those in Eq. (3.33) is a crucial operation in SVCRM and detailed discussion of matrix rotation is given in Appendix B.

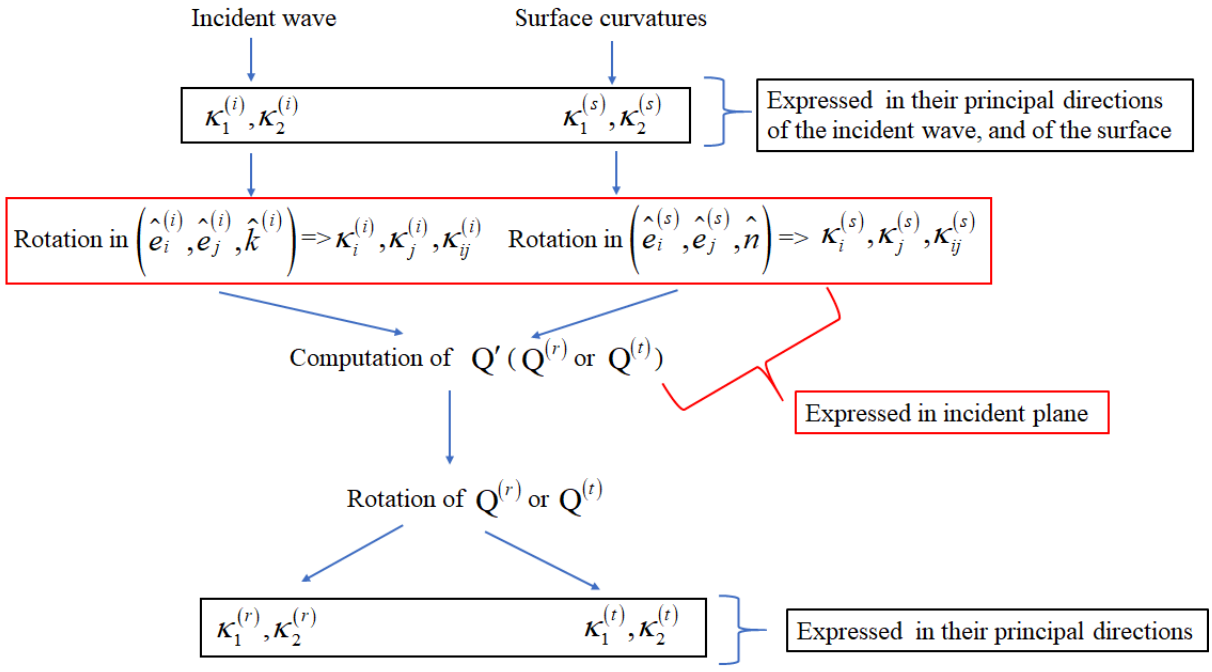

Figure 3.5: Conversion of matrices between different bases

3.2.3 Projection matrix

In order to establish the relation of waves and the particle surface, projection matrices of the incident wave $\boldsymbol{\Theta}^{(i)}$ with basis $(\hat{\boldsymbol{e}}_{\boldsymbol{i}}^{(\boldsymbol{i})}, \hat{\boldsymbol{e}}_{\boldsymbol{j}}^{(\boldsymbol{i})})$ and the reflection wave $\boldsymbol{\Theta}^{(\boldsymbol{r})}$ with basis $(\hat{\boldsymbol{e}}_{\boldsymbol{i}}^{(\boldsymbol{r})}, \hat{\boldsymbol{e}}_{\boldsymbol{j}}^{(\boldsymbol{r})})$ or the refraction wave $\boldsymbol{\Theta}^{(\boldsymbol{t})}$ with basis $(\hat{\boldsymbol{e}}_{\boldsymbol{i}}^{(\boldsymbol{t})}, \hat{\boldsymbol{e}}_{\boldsymbol{j}}^{(\boldsymbol{t})})$ on the particle surface with basis $(\hat{\boldsymbol{e}}_{\boldsymbol{i}}^{(\boldsymbol{s})}, \hat{\boldsymbol{e}}_{\boldsymbol{j}}^{(\boldsymbol{s})})$ are considered in incident plane respectively:

$$
\begin{aligned}
\boldsymbol{\Theta} &= \begin{bmatrix} \hat{\boldsymbol{e}}_{\boldsymbol{i}}^{(\boldsymbol{i})} \cdot \hat{\boldsymbol{e}}_{\boldsymbol{i}}^{(\boldsymbol{s})} & \hat{\boldsymbol{e}}_{\boldsymbol{i}}^{(\boldsymbol{i})} \cdot \hat{\boldsymbol{e}}_{\boldsymbol{j}}^{(\boldsymbol{s})} \\ \hat{\boldsymbol{e}}_{\boldsymbol{j}}^{(\boldsymbol{i})} \cdot \hat{\boldsymbol{e}}_{\boldsymbol{i}}^{(\boldsymbol{s})} & \hat{\boldsymbol{e}}_{\boldsymbol{j}}^{(\boldsymbol{i})} \cdot \hat{\boldsymbol{e}}_{\boldsymbol{j}}^{(\boldsymbol{s})} \end{bmatrix} = \begin{bmatrix} \cos\theta_i & 0 \\ 0 & 1 \end{bmatrix} \\
\boldsymbol{\Theta}^{(\boldsymbol{r})} &= \begin{bmatrix} \hat{\boldsymbol{e}}_{\boldsymbol{i}}^{(\boldsymbol{r})} \cdot \hat{\boldsymbol{e}}_{\boldsymbol{i}}^{(\boldsymbol{s})} & \hat{\boldsymbol{e}}_{\boldsymbol{i}}^{(\boldsymbol{r})} \cdot \hat{\boldsymbol{e}}_{\boldsymbol{j}}^{(\boldsymbol{s})} \\ \hat{\boldsymbol{e}}_{\boldsymbol{j}}^{(\boldsymbol{r})} \cdot \hat{\boldsymbol{e}}_{\boldsymbol{i}}^{(\boldsymbol{s})} & \hat{\boldsymbol{e}}_{\boldsymbol{j}}^{(\boldsymbol{r})} \cdot \hat{\boldsymbol{e}}_{\boldsymbol{j}}^{(\boldsymbol{s})} \end{bmatrix} = \begin{bmatrix} \cos\theta_r & 0 \\ 0 & 1 \end{bmatrix} \\
\boldsymbol{\Theta}^{(\boldsymbol{t})} &= \begin{bmatrix} \hat{\boldsymbol{e}}_{\boldsymbol{i}}^{(\boldsymbol{t})} \cdot \hat{\boldsymbol{e}}_{\boldsymbol{i}}^{(\boldsymbol{s})} & \hat{\boldsymbol{e}}_{\boldsymbol{i}}^{(\boldsymbol{t})} \cdot \hat{\boldsymbol{e}}_{\boldsymbol{j}}^{(\boldsymbol{s})} \\ \hat{\boldsymbol{e}}_{\boldsymbol{j}}^{(\boldsymbol{t})} \cdot \hat{\boldsymbol{e}}_{\boldsymbol{i}}^{(\boldsymbol{s})} & \hat{\boldsymbol{e}}_{\boldsymbol{j}}^{(\boldsymbol{t})} \cdot \hat{\boldsymbol{e}}_{\boldsymbol{j}}^{(\boldsymbol{s})} \end{bmatrix} = \begin{bmatrix} \cos\theta_t & 0 \\ 0 & 1 \end{bmatrix}
\end{aligned}
\tag{3.36}
$$

3.2.4 Wave front equation

The relation between the wave front curvatures of the wave before and after interaction with the particle surface, i.e. the incident wave and the reflected/refracted wave is

given in VCRM by the wave front equation (Eq. (3.10)). We describe here in details how to determine the wave front curvature of the wave after the interaction according to the properties of the incident wave and that of the particle surface.

- Reflected ray

  The wave front equation (3.10) for the reflected ray can be rewritten as

$$k^{(r)}\mathbf{\Theta^{(r)T}}\mathbf{Q^{(r)}}\mathbf{\Theta^{(r)}} = k^{(i)}\mathbf{\Theta^{(i)T}}\mathbf{Q^{(i)}}\mathbf{\Theta^{(i)}} + \left(k^{(r)}\cos\theta_r - k^{(i)}\cos\theta_i\right)\mathbf{C} \tag{3.37}$$

  We know $k^{(r)} = k^{(i)}$ and according to the Snell-Descartes law, we have $\theta_r = \pi - \theta_i$ and $\cos\theta_r = \cos(\pi - \theta_i) = -\cos\theta_i$. Eq. (3.37) can then be simplified to:

$$k^{(r)}\mathbf{\Theta^{(r)T}}\mathbf{Q^{(r)}}\mathbf{\Theta^{(r)}} = k^{(i)}\mathbf{\Theta^{(i)T}}\mathbf{Q^{(i)}}\mathbf{\Theta^{(i)}} - 2k^{(i)}\cos\theta_i\mathbf{C} \tag{3.38}$$

  which can be written explicitly as

$$\begin{aligned}\begin{bmatrix} \kappa_{ii}^{(r)}\cos^2\theta_i & -\kappa_{ij}^{(r)}\cos\theta_i \\ -\kappa_{ij}^{(r)}\cos\theta_i & \kappa_{jj}^{(r)} \end{bmatrix} = &\begin{bmatrix} \kappa_{ii}^{(i)}\cos^2\theta_i & \kappa_{ij}^{(i)}\cos\theta_i \\ \kappa_{ij}^{(i)}\cos\theta_i & \kappa_{jj}^{(i)} \end{bmatrix} \\ &- 2\cos\theta_i \begin{bmatrix} \kappa_{ii}^{(s)} & \kappa_{ij}^{(s)} \\ \kappa_{ij}^{(s)} & \kappa_{jj}^{(s)} \end{bmatrix}\end{aligned} \tag{3.39}$$

  Consequently, the curvature matrix of the reflected wave front $\mathbf{Q^{(r)}}$ can be calculated according to the properties of particle surface and the wave front of the incident wave:

$$\mathbf{Q^{(r)}} = \begin{bmatrix} \kappa_{ii}^{(r)} & \kappa_{ij}^{(r)} \\ \kappa_{ij}^{(r)} & \kappa_{jj}^{(r)} \end{bmatrix} \tag{3.40}$$

  with

$$\begin{cases} \kappa_{ii}^{(r)} = \kappa_{ii}^{(i)} - \dfrac{2}{\cos\theta_i}\kappa_{ii}^{(s)} \\ \kappa_{ij}^{(r)} = -\kappa_{ij}^{(i)} + 2\kappa_{ii}^{(s)} \\ \kappa_{jj}^{(r)} = \kappa_{jj}^{(i)} - 2\cos\theta_i\kappa_{jj}^{(s)} \end{cases} \tag{3.41}$$

  In order to obtain the curvature radii and the principal directions of the wave front of the reflected ray, we need to diagonalize the matrix $\mathbf{Q^{(r)}}$ by looking for a rotation matrix $\mathbf{P_r^{-1}}$ with a rotation angle δ_r:

$$\mathbf{P_r^{-1}} = \begin{bmatrix} \cos\delta_r & -\sin\delta_r \\ \sin\delta_r & \cos\delta_r \end{bmatrix} \tag{3.42}$$

such that $\mathbf{P_r Q^{(r)} P_r^{-1}}$ is diagonal, i.e.

$$\begin{aligned}\mathbf{P_r Q^{(r)} P_r^{-1}} &= \begin{bmatrix} \cos\delta_r & \sin\delta_r \\ -\sin\delta_r & \cos\delta_r \end{bmatrix} \begin{bmatrix} \kappa_{ii}^{(r)} & \kappa_{ij}^{(r)} \\ \kappa_{ij}^{(r)} & \kappa_{jj}^{(r)} \end{bmatrix} \begin{bmatrix} \cos\delta_r & -\sin\delta_r \\ \sin\delta_r & \cos\delta_r \end{bmatrix} \\ &= \begin{bmatrix} \kappa_{11}^{(r)} & \kappa_{12}^{(r)} \\ \kappa_{21}^{(r)} & \kappa_{22}^{(r)} \end{bmatrix} = \begin{bmatrix} \kappa_1^{(r)} & 0 \\ 0 & \kappa_2^{(r)} \end{bmatrix}\end{aligned} \tag{3.43}$$

with

$$\kappa_{11}^{(r)} = \kappa_{ii}^{(r)} \cos^2\delta_r + 2\kappa_{ij}^{(r)} \sin\delta_r \cos\delta_r + \kappa_{jj}^{(r)} \sin^2\delta_r = \kappa_1^{(r)} \tag{3.44}$$

$$\kappa_{12}^{(r)} = \kappa_{21}^{(r)} = (\kappa_{jj}^{(r)} - \kappa_{ii}^{(r)}) \sin\delta_r \cos\delta_r + \kappa_{ij}^{(r)} (\cos^2\delta_r - \sin^2\delta_r) = 0 \tag{3.45}$$

$$\kappa_{22}^{(r)} = (\kappa_{jj}^{(r)} - \kappa_{ii}^{(r)}) \sin\delta_r \cos\delta_r + \kappa_{ij}^{(r)} (\cos^2\delta_r - \sin^2\delta_r) = \kappa_2^{(r)} \tag{3.46}$$

The condition in Eq. (3.45) may be satisfied in three cases:

1. $\kappa_{ii}^{(r)} = \kappa_{jj}^{(r)}$ and $\kappa_{ij}^{(r)} = 0$: i, j are the two principal directions of the wave front of the reflected wave. In this case, $\kappa_1^{(r)} = \kappa_2^{(r)} = \kappa_{ii}^{(r)} = \kappa_{jj}^{(r)}$ and $\hat{\boldsymbol{e}}_{\mathbf{1}}^{(\boldsymbol{r})} = \hat{\boldsymbol{e}}_{\boldsymbol{i}}^{(\boldsymbol{r})}$, $\hat{\boldsymbol{e}}_{\mathbf{2}}^{(\boldsymbol{r})} = \hat{\boldsymbol{e}}_{\boldsymbol{j}}^{(\boldsymbol{r})}$.
2. $\kappa_{ii}^{(r)} = \kappa_{jj}^{(r)}$ and $\kappa_{ij}^{(r)} \neq 0$: in this case if $\cos^2\delta_r - \sin^2\delta_r = \cos 2\delta_r = 0$, i.e. $\delta_r = \pm\dfrac{\pi}{4}$ the matrix is diagonal.
3. $\kappa_{ii}^{(r)} - \kappa_{jj}^{(r)} \neq 0$: we can find from Eq. (3.45) that when

$$\tan 2\delta_r = \frac{2\kappa_{ij}^{(r)}}{\kappa_{ii}^{(r)} - \kappa_{jj}^{(r)}} \tag{3.47}$$

$\kappa_{12} = \kappa_{21} = 0$. The rotation angle δ_r is then given by:

$$\delta_r = \frac{1}{2} \arctan \frac{2\kappa_{ij}^{(r)}}{\kappa_{ii}^{(r)} - \kappa_{jj}^{(r)}} \tag{3.48}$$

Thus, the principal curvatures of the reflected wave are calculated with the rotation angle δ_r found above according to Eqs. (3.44) and (3.46). The principale directions are given by

$$\begin{aligned}\kappa_1^{(r)} = \kappa_{11}^{(r)} &= \kappa_{ii}^{(r)} \cos^2\delta_r + 2\kappa_{ij}^{(r)} \sin\delta_r \cos\delta_r + \kappa_{jj}^{(r)} \sin^2\delta_r \\ \kappa_2^{(r)} = \kappa_{11}^{(r)} &= \kappa_{ii}^{(r)} \sin^2\delta_r - 2\kappa_{ij}^{(r)} \sin\delta_r \cos\delta_r + \kappa_{jj}^{(r)} \cos^2\delta_r\end{aligned} \tag{3.49}$$

and the corresponding directions of the unit vectors are:

$$\begin{aligned}\hat{\boldsymbol{e}}_{\mathbf{1}}^{(\boldsymbol{r})} &= \cos\delta_r \hat{\boldsymbol{e}}_{\boldsymbol{i}}^{(\boldsymbol{r})} + \sin\delta_r \hat{\boldsymbol{e}}_{\boldsymbol{j}}^{(\boldsymbol{r})} \\ \hat{\boldsymbol{e}}_{\mathbf{2}}^{(\boldsymbol{r})} &= -\sin\delta_r \hat{\boldsymbol{e}}_{\boldsymbol{i}}^{(\boldsymbol{r})} + \cos\delta_r \hat{\boldsymbol{e}}_{\boldsymbol{j}}^{(\boldsymbol{r})}\end{aligned} \tag{3.50}$$

The two components of the amplitudes $A_1^{(r)}$, $A_2^{(r)}$ in the new coordinate system $(\hat{\boldsymbol{e}}_{\mathbf{1}}^{(\boldsymbol{r})}, \hat{\boldsymbol{e}}_{\mathbf{2}}^{(\boldsymbol{r})})$ can be expressed by the two components of the amplitudes $A_i^{(r)}$, $A_j^{(r)}$ in the coordinate system $(\hat{\boldsymbol{e}}_{\boldsymbol{i}}^{(\boldsymbol{r})}, \hat{\boldsymbol{e}}_{\boldsymbol{j}}^{(\boldsymbol{r})})$:

$$\begin{aligned} A_1^{(r)} &= \cos\delta_r A_i^{(r)} + \sin\delta_r A_j^{(r)} \\ A_2^{(r)} &= -\sin\delta_r A_i^{(r)} + \cos\delta_r A_j^{(r)} \end{aligned} \tag{3.51}$$

- Refracted ray

  For refracted ray, the wave front Eq. (3.10) can be rewritten as:

$$k^{(t)}\boldsymbol{\Theta}^{(\boldsymbol{t})\boldsymbol{T}}\mathbf{Q}^{(\boldsymbol{t})}\boldsymbol{\Theta}^{(\boldsymbol{t})} = k^{(i)}\boldsymbol{\Theta}^{(\boldsymbol{i})\boldsymbol{T}}\mathbf{Q}^{(\boldsymbol{i})}\boldsymbol{\Theta}^{(\boldsymbol{i})} + \left(\boldsymbol{k}^{(\boldsymbol{t})}\cos\theta_t - \boldsymbol{k}^{(\boldsymbol{i})}\cos\theta_i\right)\mathbf{C} \tag{3.52}$$

  Because of $k^{(i)}/k^{(t)} = n^{(i)}/n^{(t)} = 1/m$, the Eq. (3.52) can be simplified to:

$$\boldsymbol{\Theta}^{(\boldsymbol{t})\boldsymbol{T}}\mathbf{Q}^{(\boldsymbol{t})}\boldsymbol{\Theta}^{(\boldsymbol{t})} = \frac{1}{m}\boldsymbol{\Theta}^{(\boldsymbol{i})\boldsymbol{T}}\mathbf{Q}^{(\boldsymbol{i})}\boldsymbol{\Theta}^{(\boldsymbol{i})} + (\cos\theta_t - \frac{1}{m}\cos\theta_i)\mathbf{C} \tag{3.53}$$

  which can be expressed explicitly as

$$\begin{aligned} \begin{bmatrix} \kappa_{ii}^{(t)}\cos^2\theta_t & \kappa_{ij}^{(t)}\cos\theta_t \\ \kappa_{ij}^{(t)}\cos\theta_t & \kappa_{jj}^{(t)} \end{bmatrix} &= \frac{1}{m}\begin{bmatrix} \kappa_{ii}^{(i)}\cos^2\theta_i & \kappa_{ij}^{(i)}\cos\theta_i \\ \kappa_{ij}^{(i)}\cos\theta_i & \kappa_{jj}^{(i)} \end{bmatrix} \\ &\quad + (\cos\theta_t - \frac{1}{m}\cos\theta_i)\begin{bmatrix} \kappa_{ii}^{(s)} & \kappa_{ij}^{(s)} \\ \kappa_{ij}^{(s)} & \kappa_{jj}^{(s)} \end{bmatrix} \end{aligned} \tag{3.54}$$

  Let $\gamma = \cos\theta_t - \dfrac{1}{m}\cos\theta_i$, we can obtain the curvature matrix of the transmitted wave:

$$\mathbf{Q}^{(\boldsymbol{t})} = \begin{bmatrix} \kappa_{ii}^{(t)} & \kappa_{ij}^{(t)} \\ \kappa_{ij}^{(t)} & \kappa_{jj}^{(t)} \end{bmatrix} \tag{3.55}$$

  with

$$\begin{aligned} \kappa_{ii}^{(t)} &= \frac{1}{m}\frac{\cos^2\theta_i}{\cos^2\theta_t}\kappa_{ii}^{(i)} + \frac{\gamma}{\cos^2\theta_t}\kappa_{ii}^{(s)} \\ \kappa_{ij}^{(t)} &= \frac{1}{m}\frac{\cos\theta_i}{\cos\theta_t}\kappa_{ij}^{(i)} + \frac{\gamma}{\cos\theta_t}\kappa_{ii}^{(s)} \\ \kappa_{jj}^{(t)} &= \frac{1}{m}\kappa_{jj}^{(i)} + \gamma\kappa_{jj}^{(s)} \end{aligned} \tag{3.56}$$

  An operation similar as for the reflected ray has to be done to diagonalize the matrix $\mathbf{Q}^{(\boldsymbol{t})}$. Let the rotation matrix be $\mathbf{P}_{\boldsymbol{t}}$ with a rotation angle δ_t:

$$\mathbf{P}_{\boldsymbol{t}} = \begin{bmatrix} \cos\delta_t & -\sin\delta_t \\ \sin\delta_t & \cos\delta_t \end{bmatrix} \tag{3.57}$$

and

$$\begin{aligned}\mathbf{P_t Q_{(t)} P_t^{-1}} &= \begin{bmatrix} \cos\delta_t & \sin\delta_t \\ -\sin\delta_t & \cos\delta_t \end{bmatrix} \begin{bmatrix} \kappa_{ii}^{(t)} & \kappa_{ij}^{(t)} \\ \kappa_{ij}^{(t)} & \kappa_{jj}^{(t)} \end{bmatrix} \begin{bmatrix} \cos\delta_t & -\sin\delta_t \\ \sin\delta_t & \cos\delta_t \end{bmatrix} \\ &= \begin{bmatrix} \kappa_{11}^{(t)} & \kappa_{12}^{(t)} \\ \kappa_{21}^{(t)} & \kappa_{22}^{(t)} \end{bmatrix} = \begin{bmatrix} \kappa_1^{(t)} & 0 \\ 0 & \kappa_2^{(t)} \end{bmatrix}\end{aligned} \tag{3.58}$$

with

$$\kappa_{11}^{(t)} = \kappa_{ii}^{(t)} \cos^2\delta_t + 2\kappa_{ij}^{(t)} \sin\delta_t \cos\delta_t + \kappa_{jj}^{(t)} \sin^2\delta_t = \kappa_1^{(t)} \tag{3.59}$$

$$\kappa_{12}^{(t)} = \kappa_{21}^{(t)}(\kappa_{jj}^{(t)} - \kappa_{ii}^{(t)}) \sin\delta_t \cos\delta_t + \kappa_{ij}^{(t)}(\cos^2\delta_t - \sin^2\delta_t) = 0 \tag{3.60}$$

$$\kappa_{22}^{(t)} = \kappa_{ii}^{(t)} \sin^2\delta_t - 2\kappa_{ij}^{(t)} \sin\delta_t \cos\delta_t + \kappa_{jj}^{(t)} \cos^2\delta_t = \kappa_2^{(t)} \tag{3.61}$$

Similar to the reflected ray, the curvature matrix of the refracted ray is diagonalized by a rotation angle δ_t given bellow:

$$\delta_t = \begin{cases} 0 & \text{if } \kappa_{ii}^{(r)} = \kappa_{jj}^{(r)} \text{ and } \kappa_{ij}^{(r)} = 0, \\ \pm\dfrac{\pi}{4} & \text{if } \kappa_{ii}^{(r)} = \kappa_{jj}^{(r)} \text{ and } \kappa_{ij}^{(r)} \neq 0, \\ \dfrac{1}{2}\arctan\dfrac{2\kappa_{ij}^{(t)}}{(\kappa_{ii}^{(t)} - \kappa_{jj}^{(t)})} & \text{if } \kappa_{ii}^{(t)} - \kappa_{jj}^{(t)} \neq 0. \end{cases} \tag{3.62}$$

Finally, the principal curvatures of the refracted wave are calculated by

$$\begin{aligned}\kappa_1^{(t)} &= \kappa_{ii}^{(t)} \cos^2\delta_t + 2\kappa_{ij}^{(t)} \sin\delta_t \cos\delta_t + \kappa_{jj}^{(t)} \sin^2\delta_t \\ \kappa_2^{(t)} &= \kappa_{ii}^{(t)} \sin^2\delta_t - 2\kappa_{ij}^{(t)} \sin\delta_t \cos\delta_t + \kappa_{jj}^{(t)} \cos^2\delta_t\end{aligned} \tag{3.63}$$

and the corresponding principal directions of the wave front of the refracted wave are given by:

$$\begin{aligned}\hat{\boldsymbol{e}}_{\mathbf{1}}^{(\boldsymbol{t})} &= \cos\delta_t \hat{\boldsymbol{e}}_{\boldsymbol{i}}^{(\boldsymbol{t})} + \sin\delta_t \hat{\boldsymbol{e}}_{\boldsymbol{j}}^{(\boldsymbol{t})} \\ \hat{\boldsymbol{e}}_{\mathbf{2}}^{(\boldsymbol{t})} &= -\sin\delta_t \hat{\boldsymbol{e}}_{\boldsymbol{i}}^{(\boldsymbol{t})} + \cos\delta_t \hat{\boldsymbol{e}}_{\boldsymbol{j}}^{(\boldsymbol{t})}\end{aligned} \tag{3.64}$$

In this new coordinate system, the two components of the amplitude $A_1^{(t)}, A_2^{(t)}$ in coordinate system $(\hat{\boldsymbol{e}}_{\mathbf{1}}^{(\boldsymbol{t})}, \hat{\boldsymbol{e}}_{\mathbf{2}}^{(\boldsymbol{t})})$, can be expressed by the two components of the amplitudes $A_i^{(t)}, A_j^{(t)}$ in coordinate system $(\hat{\boldsymbol{e}}_{\boldsymbol{i}}^{(\boldsymbol{t})}, \hat{\boldsymbol{e}}_{\boldsymbol{j}}^{(\boldsymbol{t})})$ according to:

$$\begin{aligned}A_1^{(t)} &= \cos\delta_t A_i^{(t)} + \sin\delta_t A_j^{(t)} \\ A_2^{(t)} &= -\sin\delta_t A_i^{(t)} + \cos\delta_t A_j^{(t)}\end{aligned} \tag{3.65}$$

Therefore, at a given interaction point of a ray with the particle surface, we know the curvature matrix of the particle surface, and the curvature of the incident wave front, the wave front of the reflected and the refracted waves can be obtained according to the wave front equation by the procedure described above.

3.2.5 Phase of a ray

The phases of the rays play a critical role in the study of interference phenomenon. In SVCRM, three kinds of phase shift are considered in the scattering of the plane wave by particle.

1. Phase shift due to reflection

This can be calculated directly from the Fresnel coefficients (seen the previous section).

2. Phase shift due to optical path

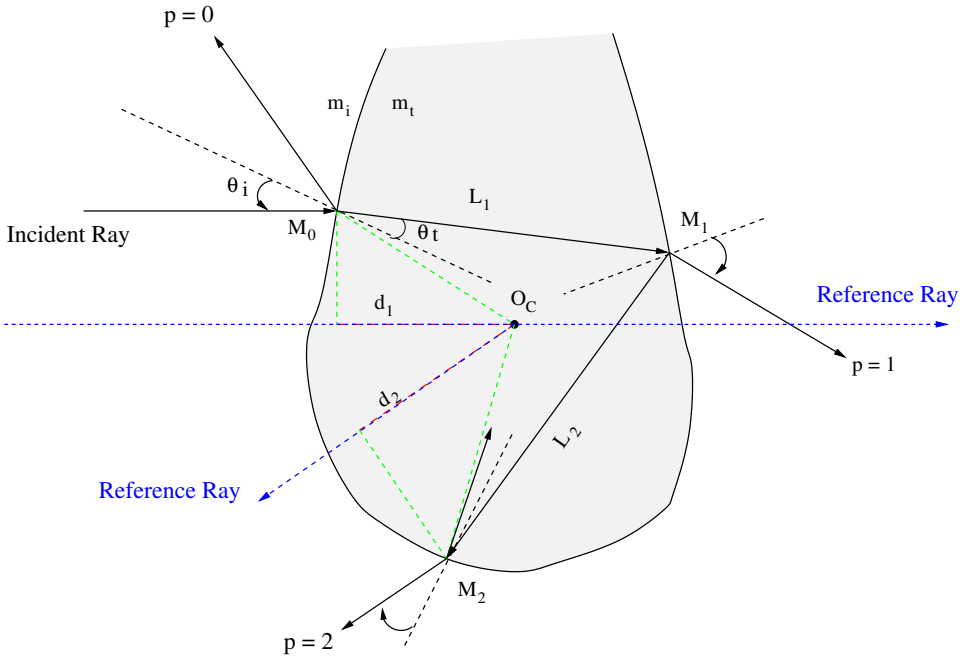

Figure 3.6: Path of a light ray through a non-spherical particle

The optical path is computed in respect to a reference, which arrives at the point O_C (not necessarily the center of the particle) in the same direction as the incident ray and goes out in the same directions as the emergent ray as if there is no particle. Fig. 3.6 presents the trajectory of a ray that interacts with a non-spherical particle. The optical path of the emergent ray of order $p = 2$ is given by

$$\Delta L_2 = m(l_1 + l_2) - (d_1 + d_2) \tag{3.66}$$

where

$$\begin{aligned} d_1 &= \overrightarrow{M_0 O_C} \cdot \hat{\boldsymbol{k}}^{(i)} \\ d_2 &= \overrightarrow{O_C M_2} \cdot \hat{\boldsymbol{k}}^{(t)} \end{aligned} \tag{3.67}$$

In general, let l_i be the distance between two successive points of i^{th} and $(i+1)^{th}$ interactions of a ray with the particle surface, the optical path of the ray of order p can be calculated by

$$\Delta L_p = m \sum_{i=1}^{p} l_i - (d_1 + d_p) \tag{3.68}$$

where d_p is

$$d_p = \overrightarrow{O_C M_p} \cdot \hat{\boldsymbol{k}}^{(\boldsymbol{t})} \tag{3.69}$$

The phase shift induced by optical path is therefore given by

$$\sigma_{P,p} = \frac{2\pi}{\lambda} \Delta L_p \tag{3.70}$$

3. Phase shift due to focal lines/points

At the passage of any focal line the phase advances by $\pi/2$, thus we must count the number of focal lines (a focal point is a crossing of two focal lines at the same point) encountered along the entire path. To this end, we use the following convention for the sign of the wave front curvature (or radius):

If the focal line is before the interaction point M, the curvature radius is negative in Fig. 3.7(a), else it is positive in Fig. 3.7 (b). According to this convention, we can obtain the number of the focal lines of a ray during its interaction with the particle surface by counting the changes of sign of the curvature radii. For example, in the case shown in Fig. 3.7(c), the sign of the curvature radius R at M is positive while the curvature radius R' at the point M' is negative, so the signs of curvature radii change between the two successive interactions. For the case shown in Fig. 3.7(d). the two curvatures radii R and R' respectively at M and M' are both positive, so no sign change of the curvature radii. The relation of the curvature radii of the wave front between two successive interactions can be expressed as :

$$R' = R - l \tag{3.71}$$

where $l = \overline{MM}'$ is the distance between the two points.

The method described above permits to count the number of focal lines inside the particle step by step according to the sign changes of the curvature radii of the wave front between two successive interactions. It is possible that the focal lines are located outside of the particle. They must also be counted since we are interested the scattered wave in far field (infinitely far from the particle). Known that the total number of focal lines of a ray pass through, the phase shift due to the focal lines is calculated with Eq. (3.24)

Finally, the total phase shifts of a emergent ray of order p is calculated by

$$\sigma_{X,p} = \sigma_{F,X,p} + \sigma_{P,p} + \sigma_{f,p} \tag{3.72}$$

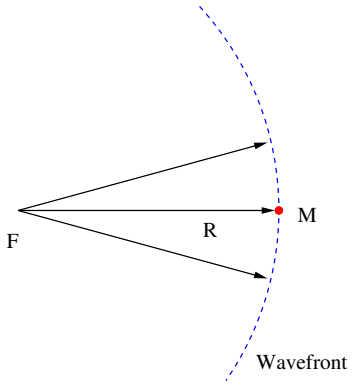

(a) R is negative

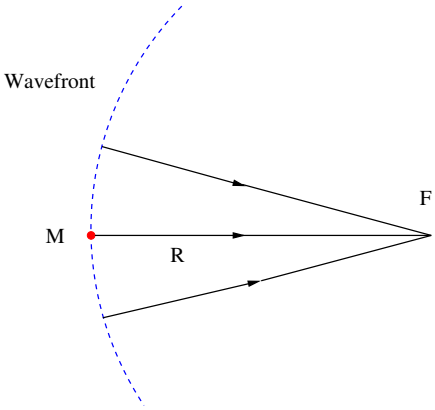

(b) R is positive

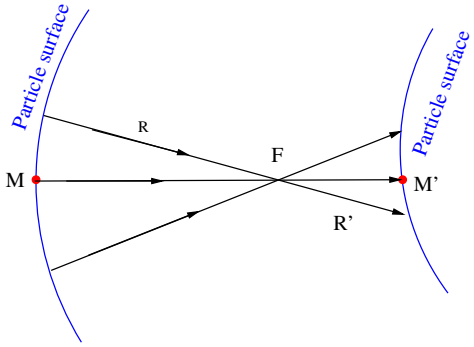

(c) The signs of curvature radii change.

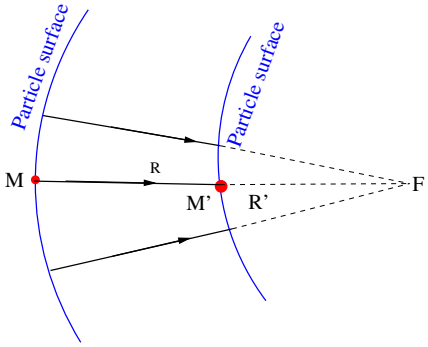

(d) The signs of the curvature radii do not change.

Figure 3.7: Definition of the signs of the curvature radii

The initial phase of a plane wave is constant, it does place role in the calculation.

3.2.6 Calculation of scattered intensity

In SVCRM, the light source, plane wave in our study, is simulated by a homogenously distributed photons and the total scattered intensity in a given direction is calculated by the summation of the contribution of all the photons arriving in a small region $\Delta\theta \cdot \Delta\phi$ in that direction. Here the photons are equivalent to the rays in VCRM and have the same properties – phase and amplitude. However, the complex amplitude of each photon is calculated in a little different manner and given by the following equation:

$$\tilde{A}_{X,p} = A_{0,X} \mid \varepsilon_{X,p} \mid e^{i\sigma_{X,p}} \tag{3.73}$$

The density of the photons is related to the property of the divergence or convergence of the emergent wave, so the divergence factor D_v in the VCRM (cf Eq. (3.21)) is not included in the calculation of the complex amplitude of a photon.

In Eq. (3.73), X stands for the polarization state relative to the last incident plane. To calculate the summation of the complex amplitudes of all the photons, we need to express them in the scattering plane – plane defined by the direction of the incident wave and the observation point. Let $\hat{\boldsymbol{e}}_\perp$ and $\hat{\boldsymbol{e}}_\parallel$ be the unit vectors perpendicular and parallel to the scattering plane, the two components of the amplitude of a photon can then be expressed in this basis by

$$\begin{aligned} \tilde{A}_{\parallel,p} &= \tilde{A}_{i,p}\hat{\boldsymbol{e}}_{\boldsymbol{i},\boldsymbol{p}} \cdot \hat{\boldsymbol{e}}_\parallel + \tilde{A}_{j,p}\hat{\boldsymbol{e}}_{\boldsymbol{j},\boldsymbol{p}} \cdot \hat{\boldsymbol{e}}_\parallel \\ \tilde{A}_{\perp,p} &= \tilde{A}_{i,p}\hat{\boldsymbol{e}}_{\boldsymbol{i},\boldsymbol{p}} \cdot \hat{\boldsymbol{e}}_\perp + \tilde{A}_{j,p}\hat{\boldsymbol{e}}_{\boldsymbol{j},\boldsymbol{p}} \cdot \hat{\boldsymbol{e}}_\perp \end{aligned} \tag{3.74}$$

The two components of the total complex amplitudes in a given detection direction can be calculated therefore

$$\begin{aligned} \tilde{A}_\parallel &= \sum_{i=0}^{N}\sum_{p=0}^{\infty} \tilde{A}_{\parallel,p} \\ \tilde{A}_\perp &= \sum_{i=0}^{N}\sum_{p=0}^{\infty} \tilde{A}_{\perp,p} \end{aligned} \tag{3.75}$$

here, N is the number of photons and the p is the order of ray.

Let the collection box be defined by two angle steps $\Delta\theta$ and $\Delta\phi$. The scattered intensity is the total energy flux collected by the box divided by the solid angle of the box $\Delta\Omega$:

$$\Delta\Omega = \Delta\theta \cdot \Delta\phi \cdot \sin\theta \tag{3.76}$$

The energy flux with interference is calculated statistically by the total complex amplitudes of each ray of all orders in given direction. The intensity with interference in a given direction can be calculated:

$$I(\theta,\phi) = \frac{\tilde{A}_{\parallel}\cdot\tilde{A}^{*}_{\parallel} + \tilde{A}_{\perp}\cdot\tilde{A}^{*}_{\perp}}{\Delta\Omega} \tag{3.77}$$

It should be noted that we deal with the scattering of large particle by using the SVCRM. Since the phase of the photons varies very rapidly as function of the direction (θ,ϕ), the collection box must be sufficiently small such that the phase of the photons coming from the same order are almost constant. This problem will be examined in details in the next chapter.

If the light source is incoherent, we need to calculated the total intensity without interference, i.e. only the summation of the intensity of each photon

$$I^{no} = \frac{\sum_{i=0}^{N}\sum_{p=0}^{\infty}\left(\tilde{A}_{\parallel,p}\cdot\tilde{A}^{*}_{\parallel,p} + \tilde{A}_{\perp,p}\cdot\tilde{A}^{*}_{\perp,p}\right)}{\Delta\Omega} \tag{3.78}$$

In this calculation, the collection box may be much larger than that for the calculation with interference by using Eq. (3.77)

3.3 Conclusion

In this chapter, the Vectorial Complex Ray Model has been presented. In order to get over the obstacle of the two dimension interpolation of irregularly distributed data, Statistic Vectorial Complex Ray Model is also introduced for the light scattering of large three-dimensional irregular particles. In this method, the light source is simulated by large number of photons and the total scattered intensity is calculated by the summation of the complex amplitudes of all photons arriving in a small collection box in a given direction. The SVCRM will be applied in the next chapter to simulate the scattering of a plane by a pendent droplet of water.

Chapter 4

Pendent droplet and its scattering patterns

To apply the Statistic Vectorial Complex Ray Model (SVCRM) to the scattering of a non-spherical particle, we must provide a description of the particle surface. In this thesis, we choose the pendent droplet for four reasons:

1. Its shape is sufficiently irregular, compared to a sphere, a spheroid or an ellipsoid whose surface can be described with simple mathematical function.
2. It is easy to obtain experimentally and stable. This is important to get high quality image and the scattering pattern to compare with numerical simulations.
3. The scattering diagrams in three dimension are very rich in information. Thus, this is a challenging case.
4. It is encountered in many applications related, for example, to research of evaporation, measurement of the surface tension, etc.

In this chapter, we will present our experimental setup to generate a pendent droplet, to register the particle image and the scattering patterns simultaneously. Then we give a detailed description of the procedure to extract the profile of the droplet and to obtain a mathematical function of the surface. These results will be used in the next chapter for the numerical simulation of the scattering diagrams of the pendent droplets.

4.1 Generation of a droplet

The SVCRM can deal with the scattering of a particle of any shape with smooth surface. The particle surface can be given by a mathematical function or obtained from

experimental image. A liquid droplet is ideal because its surface is naturally smooth and its shape depends on the condition of generation. For the pendent droplet we can register the particle image, extract its profile by image processing and to obtain an empiric function of the surface by using the Least Squares Fitting-Polynomial (LSFP).

We present firstly the experimental setup of scattering by droplet in order to obtain the profile of the pendent droplet and its scattering patterns.

4.1.1 Experimental setup

The experimental setup [59] is built up in the laboratory (Fig. 4.1), to permit to register the droplet image and scattering pattern simultaneously. The schematic of the system is shown in Fig. 4.2.

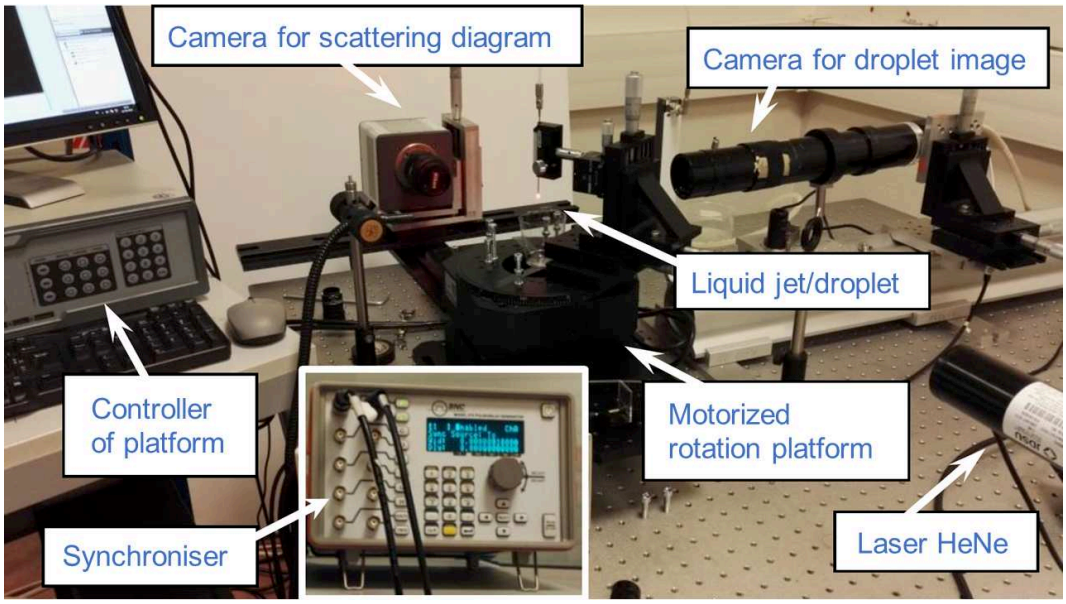

Figure 4.1: Experimental setup systems

The system is composed of a high quality He-Ne laser emitting a beam of diameter $w_0 = 0.7$ mm at wavelength $\lambda = 0.6328$ μm of red color (He-Ne JDSU Laser, Model 1145P, class 3B) followed by a polarizer and a half-wave plate. The latter is used to control the polarized state and direction of the beam emitted by the laser. Then, the inclinations of two mirrors can be adjusted to reflect the beam so that it illuminates the pendent droplet. After that, a beam expander is used to enlarge the diameter of the beam (Here, it will be multiplied by a factor of 20). This beam expander is followed by a slit-shaped diaphragm to have a rectangular shaped beam that can illuminates a part of the pendent droplet. Two convergent lenses of focal length of 300 mm for $L1$ and 200 mm for $L2$ are installed to achieve a so-called $4f$ system, which is used here to attenuate the diffraction phenomenon created by the slit diaphragm.

The system was built up for both the scattering of a water droplet and a liquid jet (generated with a circular tube of different diameters under pressure of 1 to 10 bars). To stabilize the flow, a large tank (10 litres) is used. We would note that it is very delicate to obtain a very stable droplet with a wanted form. The shape of the pendent droplet generated with this system can be adjusted easily but is not very stable. So the synchronization of the camera for the particle image and that for the scattering pattern is necessary.

The profile of the drop is recorded by Camera A, a CCD camera JAI 10−bit model TM−4200CL resolution 2048 × 2048 pixels. The scattering pattern is registered by Camera B, A HAMAMATSU 14−bit model $C9100-02$ CDD camera with a resolution of 1000×1000 pixels. A white screen is used to obtain the scattering pattern. The two cameras are connected to a BNC pulse generator synchronizer to simultaneously record images by both cameras.

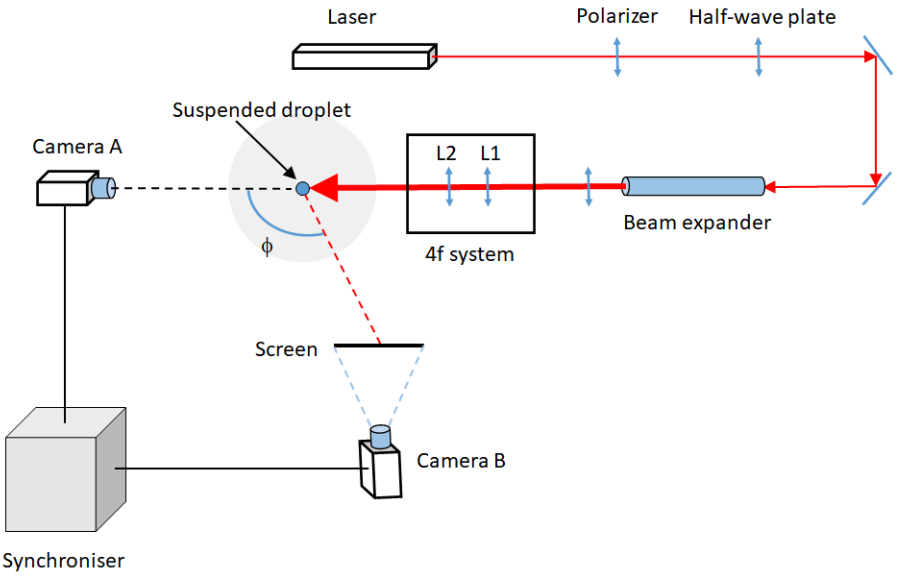

Figure 4.2: Schematic diagram of the experimental setup systems

4.1.2 Typical scattering patterns

Four scattering patterns of a pendent droplet near the first order and the second order rainbows are shown in Fig. 4.3. We find that at the very beginning of falling, the droplet is almost spherical (Fig. 4.3a, top left) and the scattering pattern is similar to that of a sphere, i.e. the fringes in the first order and the second order rainbows are almost parallel. When the droplet becomes larger, also longer (Fig. 4.3b, top right) the fringes in the second order rainbow are clearly distorted. If the droplet continues to grow (Fig. 4.3c, bottom left) the second order rainbow is more distorted and its intensity is evidently stronger than the first order rainbow. When the droplet sufficiently large

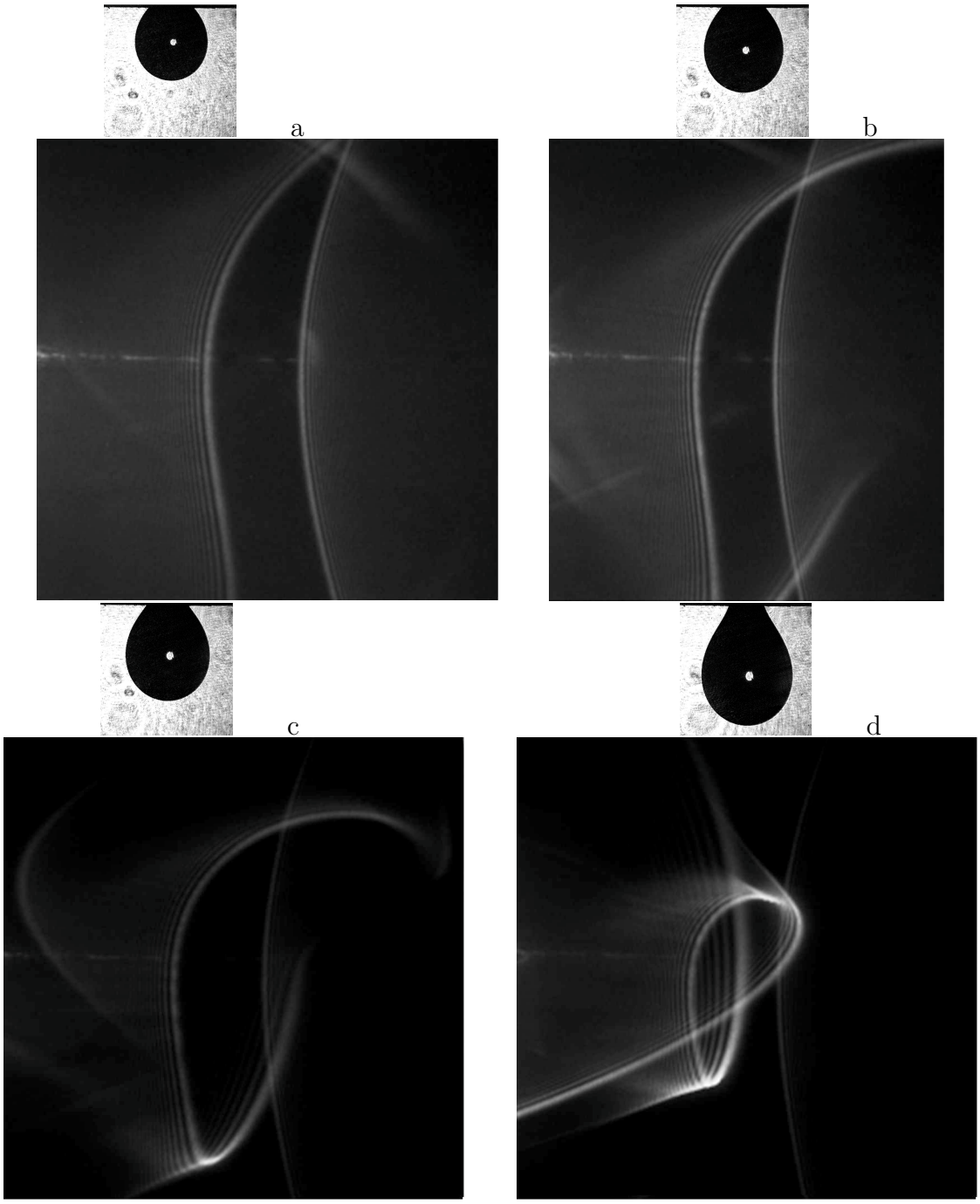

Figure 4.3: Experimental images of four pendent droplets and their scattering patterns around the rainbow angles with a perpendicularly polarized plane wave ($\lambda = 0.6328$ μm). Detection angle in horizontal direction is about $[70°, 170°]$ and that in vertical direction is about $[-40°, 40°]$.

and long (Fig.4.3d, bottom right) the second order rainbow is completely twisted and its intensity is dominant. If we observe attentively we can find that the shape of the first order rainbow evolve also when the morphology of the droplet changes, but the variation is much less visible [60]. And the heights and radii of these four droplets will be given in the following section of this chapter.

Thanks to the 4f system we can illuminate only a horizontal zone of the droplet and observe the corresponding scattering pattern in order to identify the contribution of the origin of the scattering [61]. The top part of Fig. 4.4 illustrates the total scattering patterns can be composed with the contribution of the scattering patterns from eight horizontal zones. The two pairs of figures in the lower part of Fig. 4.4 show individual scattering patterns of the zone 5 and zone 6.

The scattering pattern in the forward direction is shown in Fig. 4.5 for a droplet relatively long [62]. The clear spot in the figure is the spot of the incident light, i.e. exact forward direction at 0°. We find two straight bright lines in the above part and an arc at the bottom. If we zoom on these bright lines or arc, we observe surprisingly very clear fringes, which are similar to those in the rainbow patterns. The origin of these phenomena is curious and worth to be examined.

4.2 Description of droplet contour

In order to obtain a mathematical function to describe the profile of the droplet from the experimentally registered images, we need first to extract the contour of the image and then to fit the data to obtain an empirical function.

4.2.1 Contour of a droplet

The code of Claude Rozé will be used to extract the profile data of a image, which reads a series of experimental images and store the successive contours of droplets.

We take the droplet of Fig. 4.3d as an example. The droplet being symmetric, half of its profile is sufficient. It is extracted from the experimental image and is given in Cartesian coordinate systems (y, z), as shown in Fig.4.6.

The pendent droplet is assumed to be axis-symmetric around vertical axis z. A polar coordinate system is chosen in the following to describe the droplet profile $(\theta, r(\theta))$.

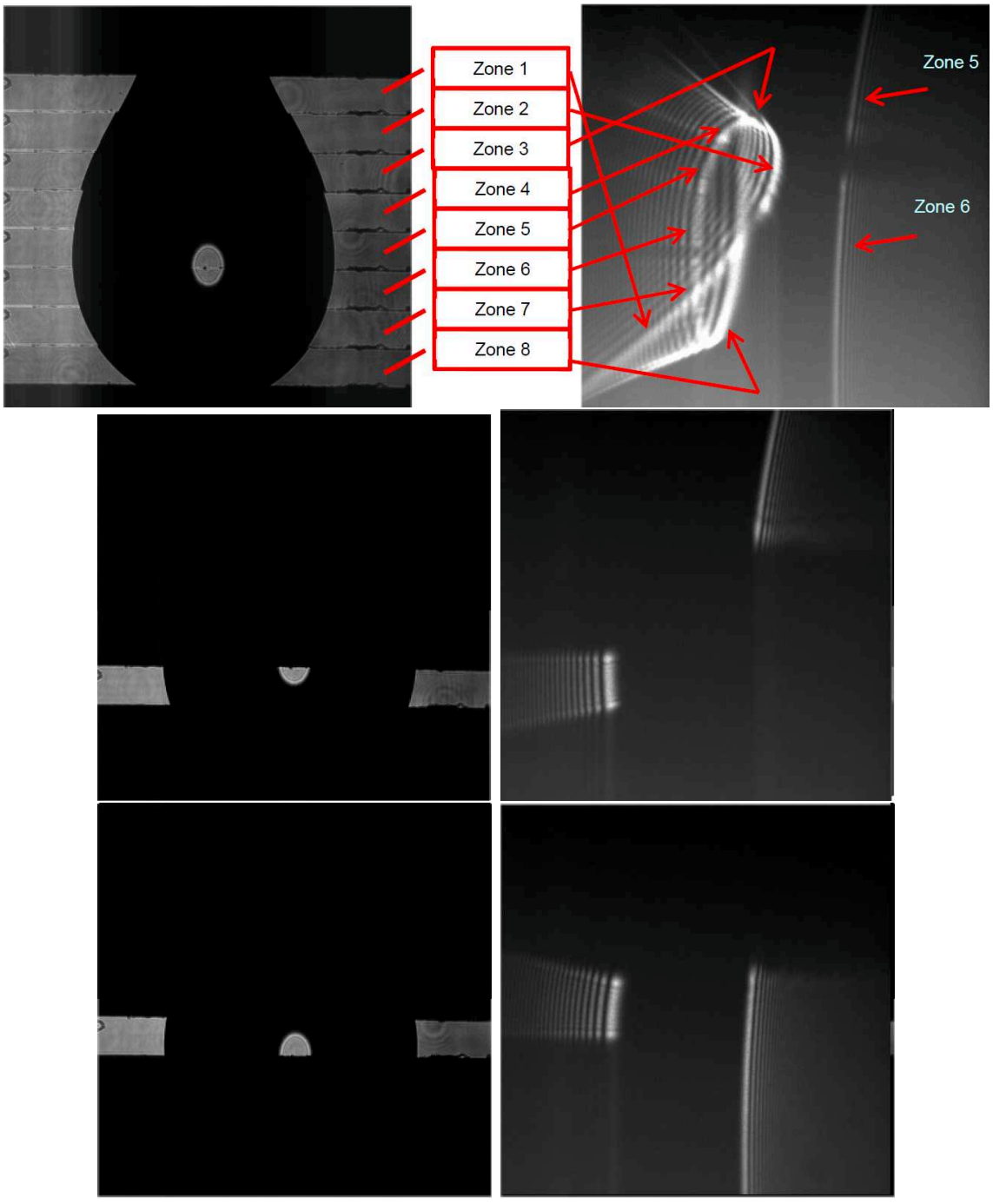

Figure 4.4: Scattering pattern (zones) of a pendent droplet with a perpendicularly polarized plane wave ($\lambda = 0.6328$ μm). Detection angle in horizontal direction is about $[110°, 150°]$ and that in vertical direction is about $[-20°, 20°]$.

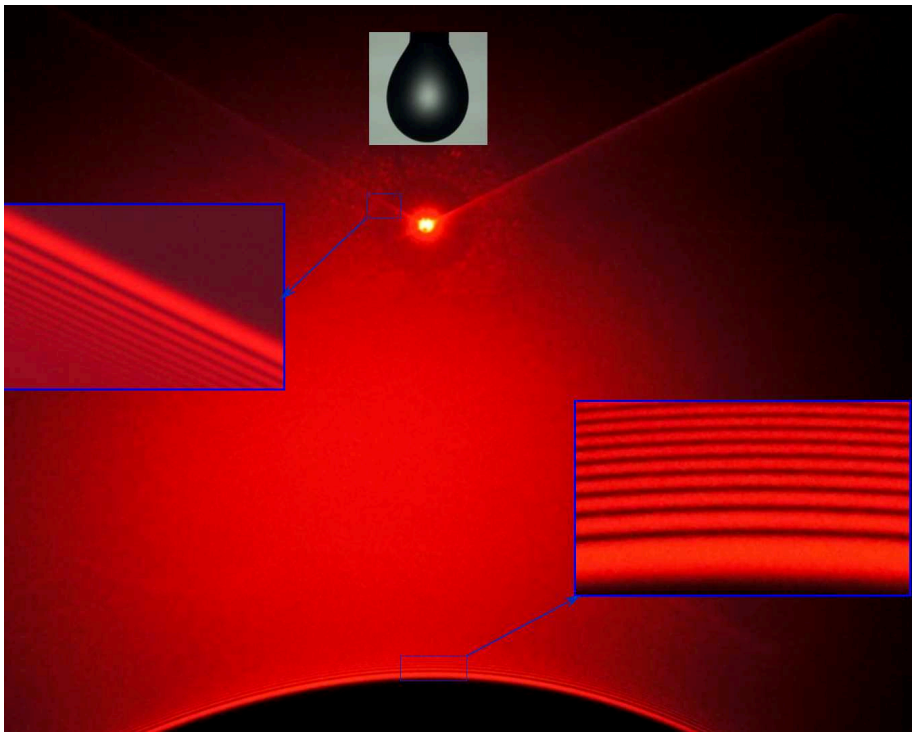

Figure 4.5: Forward scattering pattern of a pendent droplet with a perpendicularly polarized plane wave ($\lambda = 0.6328$ μm). Detection angle in horizontal direction and in vertical direction are both about $[-30°, 30°]$.

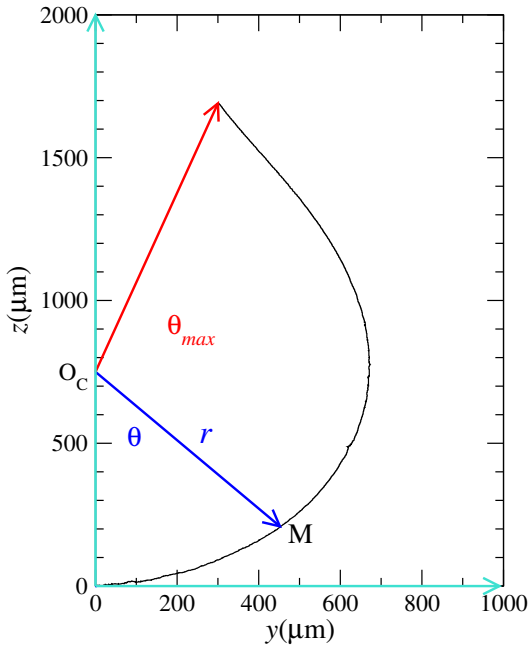

Figure 4.6: Half of the pendent droplet profile in Cartesian coordinate system.

4.2.2 Fitting contour of droplets

To obtain a mathematical function to describe the profile of the droplet surface in a polar coordinate system, we choose a center (y_C, z_C) at $(0, z_C)$. The choice of z_C is somewhat arbitrary but a good choice will make the function more stable. Let $M(y, z)$ the Cartesian coordinates of a point on the droplet surface. Then its polar coordinates are:

$$\begin{aligned} r(\theta) &= \sqrt{y^2 + (z - z_C)^2} \\ \theta &= \arccos \frac{z - z_C}{r(\theta)} \end{aligned} \tag{4.1}$$

where $r(\theta)$ is the distance between the center of the droplet to the point M on the contour of droplet and θ is the angle of $r(\theta)$ relative to the negative direction of the $z-$axis.

The droplet profile extracted from the image $r_e(\theta)$ is given in the polar coordinate system in Fig.4.7 (black curve). It is not so smooth because of the experimental and numerical noise. In order to obtain a smooth curve, a Least Squares Fitting—Polynomial is applied.

Suppose that the profile $r(\theta)$ is expressed in a polynomial function:

$$r(\theta) = a_0 + a_1\theta + a_2\theta^2 + \cdots + a_k\theta^k + \cdots + a_n\theta^n = \sum_{k=0}^{N} a_k\theta^k \tag{4.2}$$

Then, the coefficients of the polynomial $a_k\theta^k$ can be determined by minimizing the object function in a least square sense:

$$\Delta = \sum_{i=1}^{i=N_e} \left[r(\theta_i) - r_e(\theta_i)\right]^2 \tag{4.3}$$

where N_e are the total number of point of the experimental data $r_e(\theta_i)$. And the fitted curved is obtained with a least square method (detail information seen in Appendix A).

By our experience, we find that a 10^{th} order polynomial is good enough to meet our acquirement. The fitted curved is shown in Fig. 4.7 (the red curve).

We apply the same procedure to three other experimental images of droplets in Fig. 4.3. The contours extracted from the experimental images of the four droplets are shown in Fig. 4.8 in Cartesian coordinate system.

For each droplet, a 10^{th} degree polynomial is used for $r(\theta)$, the coefficients are determined by the least-square fitting of the data extracted from the contour of the particle image. The original and fitted profiles of the four droplets are shown in the polar coordinate system in Fig. 4.9. The coefficients of the polynomials of the four droplets are given in Tab. 4.1.

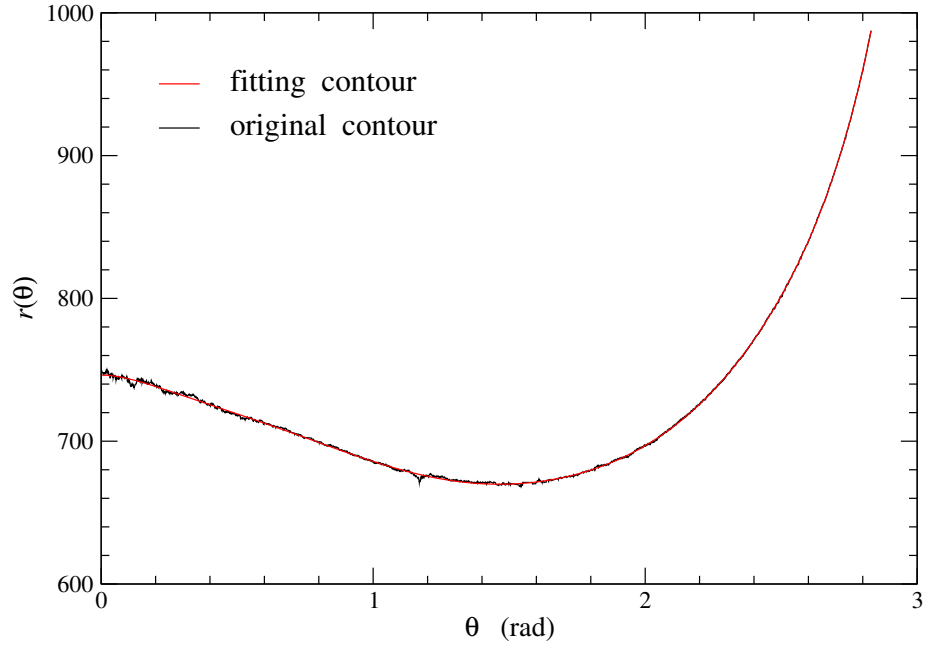

Figure 4.7: Half of the pendent droplet profile before and after fitted by Least Squares Fitting-Polynomial in polar coordinate system

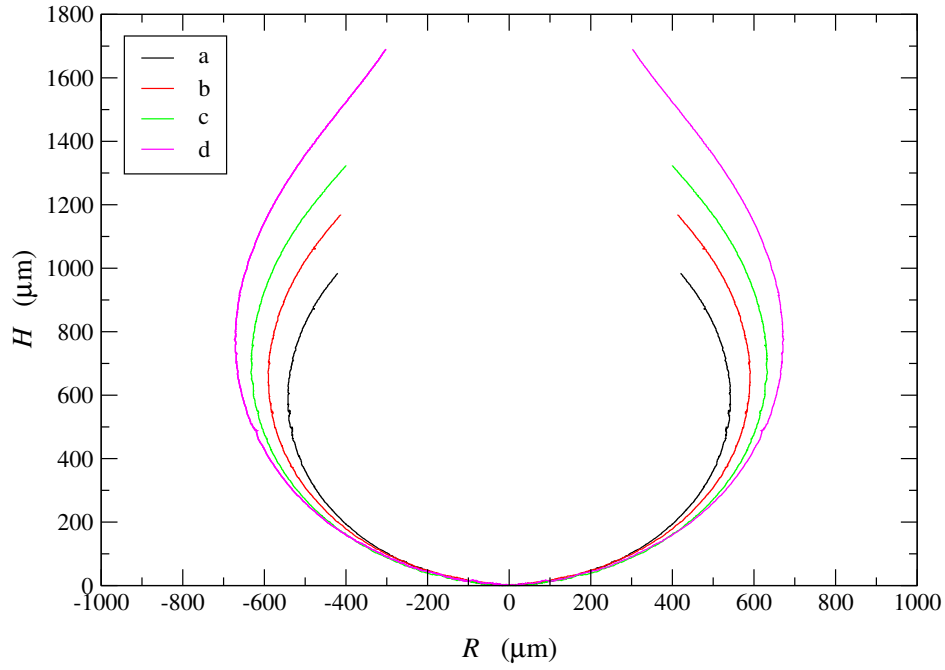

Figure 4.8: Contours of four shaped droplets in Cartesian coordinate system

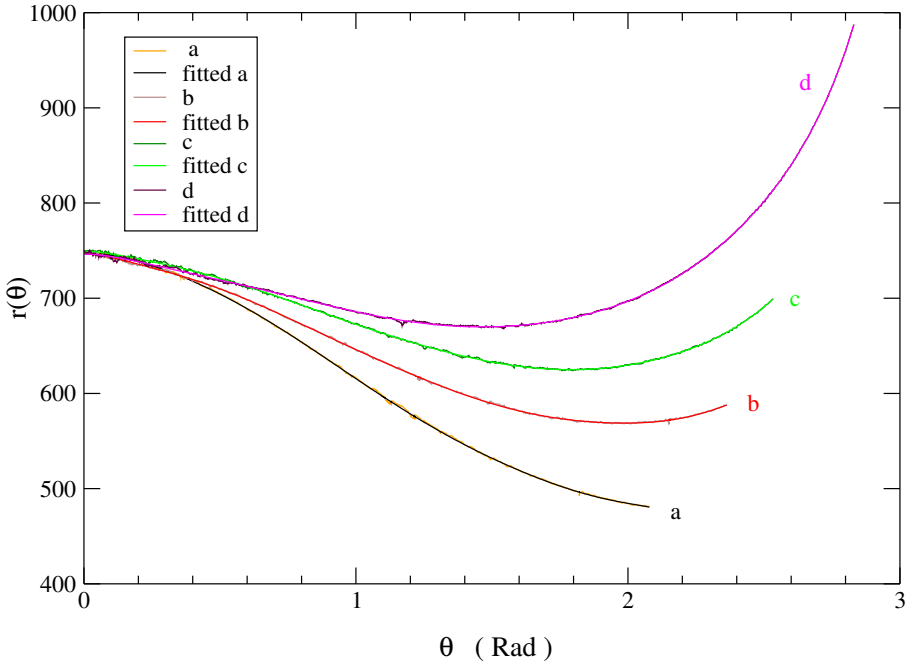

Figure 4.9: Profiles of four shaped droplets in polar coordinate system

Table 4.1: Coefficients of the 10^{th} degree polynomials for four shaped droplets.

droplet / a_k	**a**	**b**	**c**	**d**
a_0	747.61034	746.74061	749.39186	746.30693
a_1	0.00000	0.00000	0.00000	0.00000
a_2	−300.51350	−600.45388	−394.08289	−335.16810
a_3	495.96190	2635.31007	1498.96476	893.25823
a_4	−764.50390	−6710.34842	−3468.01254	−1285.61301
a_5	789.41741	9924.94844	4699.33362	956.98845
a_6	−609.26943	−8995.44061	−3895.36553	−275.10620
a_7	416.37338	5091.00818	2012.15253	−73.21056
a_8	−216.69211	−1755.25708	−631.88414	77.67261
a_9	65.29246	337.17146	110.32663	−21.37277
a_{10}	−8.12220	−27.65446	−8.20556	2.07795

4.2.3 Three dimensional coordinates of a droplet

In order to intuitively describe the smooth surface of droplets, the profile $r(\theta)$ is expressed in Cartesian coordinate system. If Cartesian coordinates (X, Z) are used (X in the horizontal direction and Z in the vertical upwards direction) and its origin O is located at the bottom of the droplet. The fitted droplet profile can be expressed as:

$$\begin{aligned} x(r(\theta), \theta) &= r(\theta) \sin\theta \\ z(r(\theta), \theta) &= z_C - r(\theta) \cos\theta \end{aligned} \tag{4.4}$$

The pendent droplet is assumed to be axisymmetric around vertical axis Z with the angle $\varphi \in [-180°, 180°]$ and the angle $\theta \in [0°, 180°]$. Let $r(x, y, z)$ be any point of the droplet profile defined by $(\theta, \varphi, r(\theta))$. Let plane $P' = (X', Z)$ with the axis X' obtained by rotation of X around Z of angle φ. Point M is on the plane P', which can be expressed in Cartesian coordinates (X, Y, Z):

$$\begin{aligned} x(\theta, \varphi, r(\theta)) &= r(\theta) \sin\theta \cos\varphi \\ y(\theta, \varphi, r(\theta)) &= r(\theta) \sin\theta \sin\varphi \\ z(\theta, \varphi, r(\theta)) &= z_C - r(\theta) \cos\theta \end{aligned} \tag{4.5}$$

Accordingly, any point on the droplet surface can be expressed by Eq. (4.5) in spherical coordinate system, which can be used to investigate the properties of shaped droplets and their scattering intensity distributions.

4.3 Interaction of a plane wave with a droplet

The determination of the interaction point of a photon (or ray) with the droplet surface is an essential task in the calculation of SVCRM. To prepare the numerical simulation of light scattering of a pendent droplet, we give a detailed description of the procedure to determine the interaction point of a photon with droplet surface and calculate the related properties of the droplet surface, such as the curvature radii, the normal of the surface.

4.3.1 Light source

In SVCRM, all waves are described by large number of photons. The photons are generated randomly on the surface. Our source is much larger than the size of the droplet and it is considered as a plane wave in the simulation.

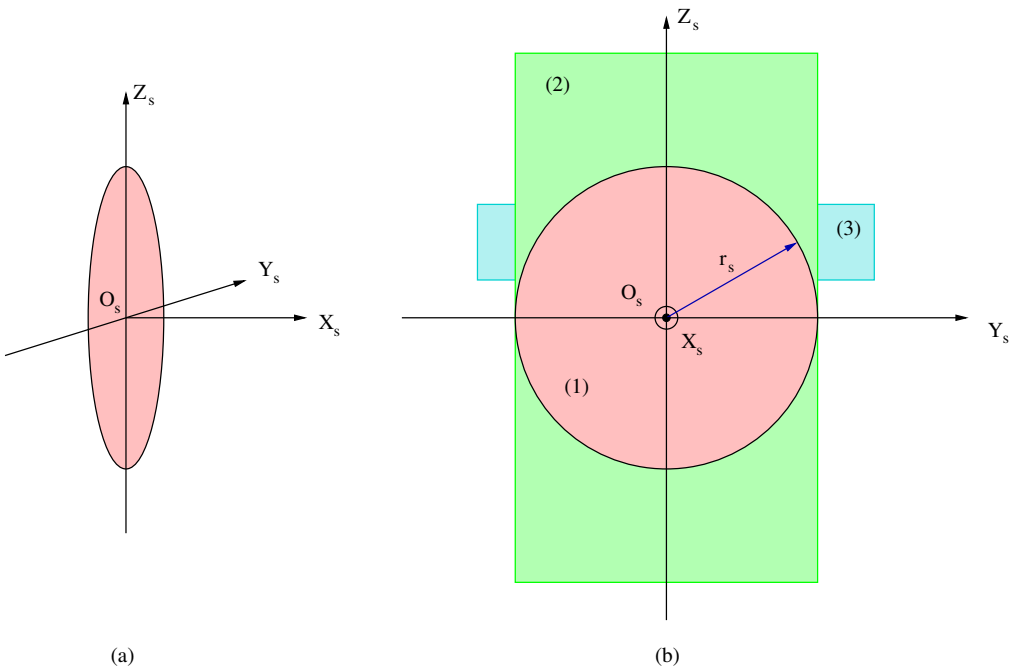

Figure 4.10: Coordinate system of laser source

The pendent droplet can be more or less long. For the droplet to be entirely illuminated, the light source is a rectangle disk of two semi-axes adjustable. Suppose that the light propagate along x axis and the center of the elliptical section is at O_s (see Fig. 4.10(a)).

The position of any photon (x_s, y_s, z_s) can be expressed in the source coordinate system:

$$\begin{aligned} x_s &= 0 \\ y_s &= a_y r_s \left[2 \text{ rand}() - 1\right] \\ z_s &= a_z r_s \left[2 \text{ rand}() - 1\right] \end{aligned} \tag{4.6}$$

where `rand()` is a function which generates a homogeneously distributed random number between 0 and 1. r_s is the radius of the round light source, shown in Fig. 4.10(b)(1). The coefficients a_y and a_z vary according to the shape of the droplet. Fig. 4.10(b)(2) illustrates the source region with $a_y = 1$ and $a_z > 1$ with $r_s = R_e$, which is used for the droplet of the height H greater than the radius of the droplet at the equatorial plane R_e. Fig. 4.10(b)(3) shows the source region with $a_y = 1$ and $a_z < 1$, which is used for the scattering patterns of a partially illuminated droplet. In our simulation, the height of the pendent droplet H is generally bigger than its radius in the equatorial plane R_e, the value of r_s is taken to be equal to R_e and $a_y = 1$.

If the center of the source O_s located at point (x_c, y_c, z_c) in the droplet coordinate system, the starting position of a photon in the droplet coordinate system (x_0, y_0, z_0)

can be calculated by:

$$\begin{aligned} x_0 &= x_c + x_s \\ y_0 &= y_c + y_s \\ z_0 &= z_c + z_s \end{aligned} \tag{4.7}$$

The incident plane wave with vertical polarisation can be expressed in the droplet coordinate system by photons of amplitude components $a_y = 0$ along y axis and $a_z = 1.0$ along z axis. The propagation direction $\hat{\boldsymbol{k}}$ of the incident wave is along x axis. Since the phase of the plane wave is a constant, the phase of a photon is defined as zero in our calculation.

4.3.2 Intersection of a ray with droplet surface

In the simulation with SVCRM, an essential task consists of finding the intersection of a ray with the surface of the droplet: it consists in the solution of the intersection of a line with a 3D surface.

At first, it is necessary for us to determine the position of the intersection point of a ray with the droplet surface.

A ray starting from $M_0(x_0, y_0, z_0)$ propagating in the direction $\hat{\boldsymbol{k}}$ is described by a vector $l\hat{\boldsymbol{k}}$ (l being the propagation distance along this direction). The droplet surface is described by a three-dimensional function $\boldsymbol{r}(x, y, z)$. Then, the intersection point $M(x, y, z)$ of the ray with the droplet surface is the solution of the equation:

$$\boldsymbol{r}(x_0, y_0, z_0) + l\hat{\boldsymbol{k}} = \boldsymbol{r}(x, y, z) \tag{4.8}$$

which can be expressed in the Cartesian coordinate system in scalar form:

$$\begin{aligned} x &= x_0 + lk_x \\ y &= y_0 + lk_y \\ z &= z_0 + lk_z \end{aligned} \tag{4.9}$$

The intersection point $M(x, y, z)$ belongs to the droplet and is expressed in the spherical coordinate system by:

$$\begin{aligned} x &= r(\theta)\sin\theta\cos\varphi \\ y &= r(\theta)\sin\theta\sin\varphi \\ z &= z_C - r(\theta)\cos\theta \end{aligned} \tag{4.10}$$

By inserting Eq. (4.10) into Eq. (4.9), we obtain following relations:

$$\begin{aligned} r(\theta)\sin\theta\cos\varphi &= x_0 + lk_x \\ r(\theta)\sin\theta\sin\varphi &= y_0 + lk_y \end{aligned} \tag{4.11}$$

$$z_C - r(\theta)\cos\theta = z_0 + lk_z \tag{4.12}$$

The propagation distance l can be extracted from Eq. (4.12):

$$l = \frac{z_C - z_0 - r(\theta)\cos\theta}{k_z} \tag{4.13}$$

and the angle φ can be extracted from Eq.(4.11):

$$\begin{aligned} \cos\varphi &= \frac{x_0 + lk_x}{r(\theta)\sin\theta} \\ \sin\varphi &= \frac{y_0 + lk_y}{r(\theta)\sin\theta} \end{aligned} \tag{4.14}$$

Because $\sin^2\varphi + \cos^2\varphi = 1$, we can obtain:

$$(x_0 + lk_x)^2 + (y_0 + lk_y)^2 = r^2(\theta)\sin^2\theta \tag{4.15}$$

Insertion of Eq. (4.13) into Eq. (4.15) yields

$$\left(x_0 + \frac{z_C - z_0 - r(\theta)\cos\theta}{k_z}k_x\right)^2 + \left(y_0 + \frac{z_C - z_0 - r(\theta)\cos\theta}{k_z}k_y\right)^2 = r^2(\theta)\sin^2\theta \tag{4.16}$$

which is

$$\begin{aligned} & \left[k_z x_0 + (z_C - z_0 - r(\theta)\cos\theta)\,k_x\right]^2 \\ + \;& \left[k_z y_0 + (z_C - z_0 - r(\theta)\cos\theta)\,k_y\right]^2 \\ - \;& k_z^2 r^2(\theta)\sin^2\theta = 0 \end{aligned} \tag{4.17}$$

The only unknown in this equation is θ which can be solved numerically by a standard algorithm for a non-linear equation. Once the value of θ of the interaction point is found, the propagation distance l can be determined by Eq. (4.13). In the case of the ray parallel to x-axis (the incident rays for example, Eq. (4.15) must be used instead since k_y and k_z are zero. Finally, the coordinates of the new interaction point are calculated by Eq. (4.10).

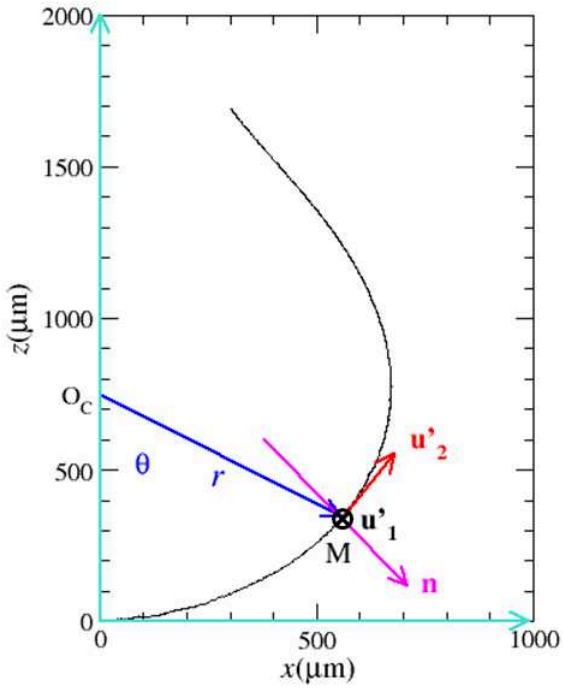

Figure 4.11: Definition of the normal vector and principal directions of the pendent droplet

4.3.3 Curvature of the droplet surface

Next, the curvatures, the principal directions and the normal vector of the droplet surface at the interaction point are to be calculated.

Firstly, the expressions of the two principal directions and the normal vector of the droplet surface at the interaction point are derived. The position of any point on the droplet profile can be defined in polar coordinates by $M(\theta,\, r(\theta))$ (see Eq. (4.4)). The vector $\boldsymbol{u}_2$ tangent to the particle surface in xz plane (Fig 4.11) is given by:

$$\boldsymbol{u_2'} = \begin{bmatrix} x'(r(\theta),\theta) \\ 0 \\ z'(r(\theta),\theta) \end{bmatrix} \tag{4.18}$$

Let the curve $r(\theta)$ rotates around $z-$axis of an angle φ. The vector $\boldsymbol{u_2}$ is then given by:

$$\boldsymbol{u_2} = \begin{bmatrix} x'(r(\theta),\theta)\cos\varphi \\ x'(r(\theta),\theta)\sin\varphi \\ z'(r(\theta),\theta)\sin\theta \end{bmatrix} \tag{4.19}$$

its normalized vector $\hat{\boldsymbol{e}}_{\boldsymbol{2}}$ is:

$$\hat{\boldsymbol{e}}_{\boldsymbol{2}} = \frac{\boldsymbol{u_2}}{\|\boldsymbol{u_2}\|} \tag{4.20}$$

The normal vector of the particle surface is obtained by a $\pi/2$ rotation of $\boldsymbol{u}'_{\boldsymbol{2}}$ in a clockwise direction and is expressed:

$$\boldsymbol{n} = \begin{bmatrix} -z'(r(\theta),\theta)\cos\varphi \\ -z'(r(\theta),\theta)\sin\varphi \\ x'(r(\theta),\theta) \end{bmatrix} \tag{4.21}$$

and the normalized vector:

$$\hat{\boldsymbol{n}} = \frac{\boldsymbol{n}}{\|\boldsymbol{n}\|} \tag{4.22}$$

And the third unit vector $\boldsymbol{u_1}$ of the base is defined simply by:

$$\hat{\boldsymbol{u}}_1 = \hat{\boldsymbol{u}}_2 \times \hat{\boldsymbol{n}} \tag{4.23}$$

which gives:

$$\hat{\boldsymbol{e}}_{\boldsymbol{1}} = \begin{bmatrix} \sin\varphi \\ -\cos\varphi \\ 0 \end{bmatrix} \tag{4.24}$$

Now, we derive the curvatures of the droplet surface given in polynomial function. The two curvatures along the principal direction $\boldsymbol{u_1}$ and $\boldsymbol{u_2}$ will be noted respectively by κ_1 and κ_2.

The analytical description of the droplet profile in xz plane has been expressed by Eq. (4.4) in polar coordinate system. The first derivatives of the coordinates x and z relative to θ are:

$$\begin{aligned} \frac{dx}{d\theta} &= x'(\theta) = r'(\theta)\sin\theta + r(\theta)\cos\theta \\ \frac{dz}{d\theta} &= z'(\theta) = -r'(\theta)\cos\theta + r(\theta)\sin\theta \end{aligned} \tag{4.25}$$

Their second derivatives are:

$$\begin{aligned} x''(\theta) &= r''(\theta)\sin\theta + 2r'(\theta)\cos\theta - r(\theta)\sin\theta \\ z''(\theta) &= -r''(\theta)\cos\theta + 2r'(\theta)\sin\theta + r(\theta)\cos\theta \end{aligned} \tag{4.26}$$

Thus, the curvatures of the surface by rotation of a curve at a point can be expressed as [63]:

$$\begin{aligned}\kappa_1 &= \frac{-x''(\theta)z'(\theta) + x'(\theta)z''(\theta)}{\left[x^2(\theta) + z^2(\theta)\right]^{3/2}} \\ \kappa_2 &= \frac{z'(\theta)/x(\theta)}{\left[x^2(\theta) + z^2(\theta)\right]^{1/2}}\end{aligned} \tag{4.27}$$

By the insertion of the expressions of the coordinates x and z given in Eq. (4.4), their first and second derivatives Eqs. (4.26) and (4.26) into Eq. (4.27), we obtain the principal curvatures of the droplet:

$$\begin{aligned}\kappa_1 &= \frac{2r'^2(\theta) + r^2(\theta) - r(\theta)r''(\theta)}{\left[r'^2(\theta) + r^2(\theta)\right]^{3/2}} \\ \kappa_2 &= \frac{1}{\left[r'^2(\theta) + r^2(\theta)\right]^{1/2}}\left[1 - \frac{r'(\theta)}{r(\theta)\tan\theta}\right]\end{aligned} \tag{4.28}$$

Their corresponding principal curvature radii are respectively:

$$\begin{aligned}\rho_1 &= \frac{\left[r'^2(\theta) + r^2(\theta)\right]^{3/2}}{2r'^2(\theta) + r^2(\theta) - r(\theta)r''(\theta)} \\ \rho_2 &= \frac{\left[r'^2(\theta) + r^2(\theta)\right]^{1/2}}{1 - r'(\theta)/r(\theta)\tan\theta}\end{aligned} \tag{4.29}$$

The principal directions, the curvatures and the corresponding curvature radii as well as the normal vector at a interaction point of a ray with the droplet surface are derived. Thanks to the axis-symmetry of the droplet, the curvatures (equally the curvature radii) depends only on θ. The dependance of the principal directions and the normal vector on the azimuth angle φ is also very simple - just only the projection functions $\sin\varphi$ and $\cos\varphi$.

4.4 Equatorial plane

The equatorial plane of a pendent droplet, for example, plays a special role in our simulation and analysis. The rays on this plane remain always in this plane if the incident direction is also in this plane. The scattering of the light on or near the equatorial plane is very similar to a spheroidal particle. These particularities play a critical role in the validation of our code, and in the analysis of the scattering phenomena.

We have mentioned in the first section of this chapter that the choice of the origin of the polar coordinate system O_C to describe the profile of the droplet is somewhat

arbitrary. It is therefore not necessarily on the equatorial plane. We will discuss in the following their relation.

The tangent plane on a point in equatorial plane of the droplet is vertical, i.e. $dz/dx = \infty$ or $dx/dz = 0$. According to the expression of the profile in the Cartesian coordinates Eq. (4.4) and their first derivatives Eq. (4.25), we have:

$$\frac{dx}{dz} = \frac{r'(\theta)\sin\theta + r(\theta)\cos\theta}{r'(\theta)\cos\theta + r(\theta)\sin\theta} = 0 \tag{4.30}$$

That is

$$r'(\theta)\sin\theta + r(\theta)\cos\theta = 0 \tag{4.31}$$

The solution of Eq. (4.31) θ_e is the location of the equatorial plane in polar coordinate system. The position on z axis of the equatorial plane z_e is therefore:

$$z_e = z_C - r(\theta_e)\cos\theta_e \tag{4.32}$$

4.5 Detection direction

For the description of the profile of the droplet, we have chosen the symmetric axis as z axis, x axis as the direction of the incident wave and the angle θ toward the negative direction of the z axis (so that the top of the droplet is at $\theta = 0$). These choices are not coincident to the conventional definition of the scattering coordinates. So it is necessary to make clear the relation between different coordinates used in the discussion of the scattering results.

Here again, the particularity of the equatorial plane will be considered. We want the forward direction is still the origin of direction angles of observation, i.e. at $\theta_d = 0$ and $\phi_d = 0$ and the z axis is still in the vertical direction and coincident with the droplet axis. The incident direction is along x axis. So the relation between the angles (θ, φ) and the observation direction angles (θ_d, ϕ_d).

$$\begin{aligned} \theta_d &= \frac{\pi}{2} - \arccos\left(\hat{\boldsymbol{k}} \cdot \hat{\boldsymbol{z}}\right) = \theta - 90^\circ \\ \phi_d &= \operatorname{atan2}\left(k_y, k_x\right) = \varphi \end{aligned} \tag{4.33}$$

The observation is in far field, the origin of the coordinate system (at O_e or O_C) does not influences the definition of the direction angles.

To calculate the summation of all the emergent photons arriving in the same direction (small box in the SVCRM), the vectorial electric field of each photon should be projected in the common basis. Here we choose the two conventional directions: $\boldsymbol{e}_\parallel$ in the scattering plane and $\boldsymbol{e}_\perp$ perpendicular to the scattering plane, as shown in Fig. 4.12.

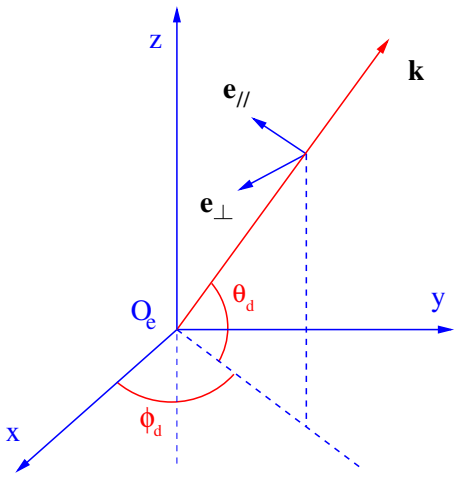

Figure 4.12: Definition of the detection angle used in SVCRM

Finally, we compile in Tab. 4.2 the parameters of the four droplets in Fig. 4.3 describing by the polynomials with the coefficients in Tab. 4.1. The size of a droplet is characterized by its height H, its radius R_e in the equatorial plane and its two principal curvature radii on the equatorial plane ρ_1, ρ_2 (calculated by Eq. (4.29)) as well as the position of its equatorial plane. These parameters will be used in the next chapter for the simulation of the scattering patterns.

Table 4.2: Parameters of the four droplets in Fig. 4.3.

droplet / parameters	**a**	**b**	**c**	**d**
$R_e(\mu\text{m})$	541.15	589.83	631.45	671.16
$H(\mu\text{m})$	989.86	1173.53	1332.83	1707.68
$Z_e(\mu\text{m})$	592.54	652.42	695.39	774.43
$\rho_1(\mu\text{m})$	541.15	589.83	631.45	671.16
$\rho_2(\mu\text{m})$	1634.36	3502.12	3773.51	2815.08
ρ_2/ρ_1	3.0202	5.9375	5.9759	4.1944

4.6 Conclusion

In this chapter, the droplet profile, shaped waves, intersection of droplet with rays as well as the detection of outgoing rays expressed in SVCRM are introduced, which prepare for the simulations in next chapter.

Chapter 5

Simulation of scattering patterns

The principle and algorithm of the SVCRM have been presented in Chapter 3. The mathematical functions and parameters describing the profiles of four typical pendent droplets have been obtained from the experimental images in the last chapter. We will now simulate the scattering patterns of the pendent droplets with our code of SVCRM. The results will be compared to the experimental scattering patterns to validate the code and to investigate the scattering mechanism. Different parameters for the numerical simulation will be examined.

The initial version of the code SVCRM has been developed by professor Claude Rozé and is for the simulation of the scattering patterns of an incoherent plane wave by a pendant droplet. The phase of the rays was not taken into account, so there was no interference. The light wave is presented by photons having the same properties of rays in VCRM and the total scattered intensity is calculated statistically by summation of intensity of all photons arriving in the same box in a given direction.

The main contribution of this thesis is to include the phase of the rays in order to be able to predict the interference, i.e. the fine structure in the scattering patterns. A code SVCRM taking into account the phase has been developed in Fortran, which can be run as a serial or a parallel program on a personal computer or a computing center according to the compilation options.

The 118 scattering patterns in this chapter have been calculated with this code in the *Centre Régional Informatique et d'Applications Numériques de Normandie* (CRIANN). Almost all the results in this chapter have been obtained by parallel calculation with 16 processors and 3 Go memory(maximum memory) for each process with the Myria calculator, which is an ATOS BULL solution with a power of 419 TFlops Xeon, 327 TFlops GPU and 27 TFlops Xeon Phi KNL. All the scattering diagrams with SVCRM have been simulated with a 64−bit Linux operating system (CentOS 7.6) and with Slurm to submit works under the development environment: Intel 2017 and 2019 compilers, Gnu 4.8.5 Fortran, C, C++ (OpenMP support), Intel MPI 2017 and 2019 libraries

(MPI-3 support) and Makefiles. For each simulation, the maximum number of photons is 2×10^9 (this number is reduced to 10^7 or 10^8 for some test cases). The computation time is about 7 hours for each case.

This chapter is organized as follows:

Firstly, we will give a brief description of the simulation procedure and the parameters used in the simulation.

Then, preliminary simulations will be done with the developed code in order to detect the influence of different parameters in the simulation.

We will investigate particularly the influence of the number of emitted photons, the size of the collection box (i.e. the steps on the detection angles).

Finally, the scattering patterns of the four droplets near the rainbow angles and in the forward directions will be given and analysed. The scattering patterns of a partially illuminated droplet are also provided which permit to investigate the scattering mechanism.

5.1 Simulation procedure and parameters

Before the simulation, we give here a brief description of the simulation procedure and the definition of the parameters used in the simulation.

5.1.1 Simulation procedure

The geometric parameters of the four droplets have been obtained and given in the previous chapter.

For a given droplet, we chose the size and the center position of the light source and define the zone of illumination (full or partial). The photons are generated with a standard random number generator (in Fortran) in simulation and the photons are supposed distributed homogeneously on the light source area.

All photons propagate along x-axis and interact with the droplet. The amplitude, the direction, the phase, the polarization and the curvatures of each photon are calculated step by step with SVCRM. The emergent photons are collected by small boxes $\Delta\theta \cdot \Delta\phi \cdot \sin\theta$ in far filed in a given direction (θ, ϕ).

The total scattered intensity are calculated statistically in two manners:

- **without interference:** Total scattered intensity is calculated by the summation of the squares of the amplitude of each photon arriving in the same box (Eq. (3.78)).
- **with interference:** The total complex amplitude is calculated by the summation of the complex amplitude of all the photons arriving in the same box and the total scattered intensity is the square of the total complex amplitude (Eqs. (3.75) and (3.77)).

The scattering patterns without interference provide a global intensity distribution permitting identification of the arriving zones of photons while the scattering patterns with interference give details in the scattering which correspond directly to the scattering patterns registered in the experiment. All the scattering patterns are presented in level brightness: red for high intensity and black for weak intensity.

5.1.2 Definition of parameters of the simulations

The parameters of the light source, the geometry of the droplet and the collection direction used in our simulations are defined as follows and illustrated in Fig. 5.1 :

- The global geometry of the droplet is characterized by its height H and its diameter $2R_e$. Its relative refractive index m is taken to be 1.333.
- The general coordinate system $(O; x, y, z)$ is used in the calculation of all the parameters.
- The light source is a circular zone of radius r_s. The light propagates in x direction and the beam center is located at (x_c, y_c, z_c) in the general coordinate system $(O; x, y, z)$.
- The equatorial plane of the droplet is located at O_e on the z-axis z_e.
- The scattered light is observed in the direction defined by (θ, ϕ) with $\theta \in [-90°, 90°]$ the angle relative to the horizontal plane and $\phi \in [-180°, 180°]$ the azimuth angle relative to xz plane. Two unit vectors $\hat{\boldsymbol{e}}_{\parallel}$ and $\hat{\boldsymbol{e}}_{\perp}$ are used to calculate the two components of the complex amplitudes (parallel polarization and perpendicular polarization).
- The total number of photons emitted from the source for one simulation is N.
- The detection steps $C_\theta = \Delta\theta$ and $C_\phi = \Delta\phi$ define the size of the collection boxes. $\Delta\theta$ and $\Delta\phi$ correspond respectively the steps of the two angles (θ and ϕ) indicating the scattering direction.
- Order of ray p.

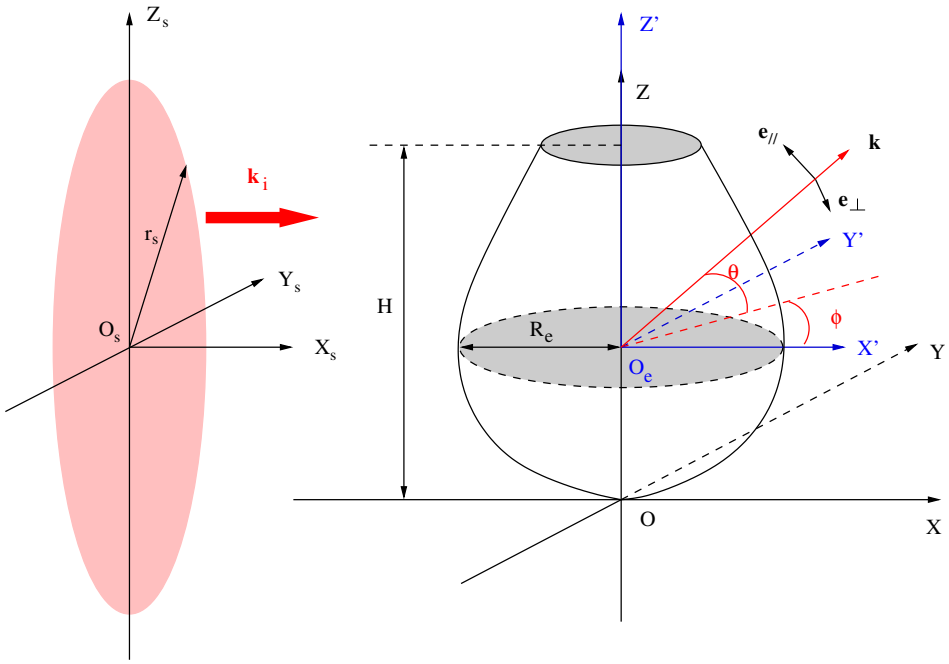

Figure 5.1: Definition of the coordinate systems used in SVCRM

5.2 Preliminary simulations

We present here the first simulation results which permit to observe the scattering characteristics of a pendent droplet and to detect the influence of different parameters which will be examined later in details.

5.2.1 First simulation results

The droplet **a** and the droplet **d** (see Fig. 4.3 and Tab. 4.2) are two very typical droplets: the first is the less deformed (nearly a sphere) and the second is the most deformed. They will be used to illustrate the typical scattering properties and to test the code. We will be interested particularly in the intensity distribution around the rainbow angles because it is the most sensible to the deformation of the particle.

We show in Fig. 5.2 the scattering patterns of the two pendent droplets **a** and **d** with the number of emitted photons $N = 4 \times 10^7$. The intensity distributions with and without interference by the same droplet are very similar under the same conditions. The droplet **a** is almost spherical and the rainbows are similar to that of a sphere: the first order rainbow ($p = 2$) and the second order rainbow ($p = 3$) are almost parallel (Fig. 5.2(a) and Fig. 5.2(b)). On the contrary, the two rainbows of the droplet **d** are very different, the second order rainbow of the droplet **d** is completely twisted (Fig. 5.2(c) and Fig. 5.2(d)) while the first order rainbow remains similar to the droplet

a because the droplet **d** is much more deformed.

We find that the scattering patterns with interference is stronger than those without interference. This can be explained by the interference enhancement of rays in terms of physics and the square of a summation of a series of quantities may be much greater the summation of the square of individual quantity of the series in terms of mathematics.

Table 5.1: Parameters for the preliminary simulation of the scattering intensities with and without interference.

Parameters	**Values**	
$\lambda(\mu\text{m})$	0.6328	
m	1.333	
$(x_c, y_c, z_c)(\mu\text{m})$	$(-5000, 0, 0)$	
$z_s(\mu\text{m})$	$[0, H]$	
$y_s(\mu\text{m})$	$[-R_e, R_e]$	
θ	$[-15°, 15°]$	
ϕ	$[120°, 150°]$	
(C_ϕ, C_θ)	$(0.2°, 0.2°)$	
p	$2, 3$	
N	4×10^7	4×10^8

Unexpectedly, the interference phenomenon is not visible in the intensity distributions with interference in Fig. 5.2(b) and Fig. 5.2(d) whether the droplet is similar to a sphere or not. In the statistical simulation, we think first that may be caused by the insufficient number of photons. In order to investigate the effect of the number of emitted photons, we multiply the number of emitted photons by ten, i.e. $N = 4 \times 10^8$ and the results are shown in Fig. 5.3.

By comparing Fig. 5.3(b) and Fig. 5.3(d) to Fig. 5.2(b) and Fig. 5.2(d), we find that the scattering patterns with interference remain unchanged. We have also done the calculation with other number of emitted photons. It can be concluded that the number of emitted photons is not of great importance in this circumstance, notably for the detection angular steps.

The very possible problem may come from the calculation of the phase since the interference is caused just by the phase difference between different photons. We have checked very carefully the calculation of all kinds of phase shifts involved in the SVCRM. We found finally that the detection steps (box size) plays a crucial rule in the interference phenomenon.

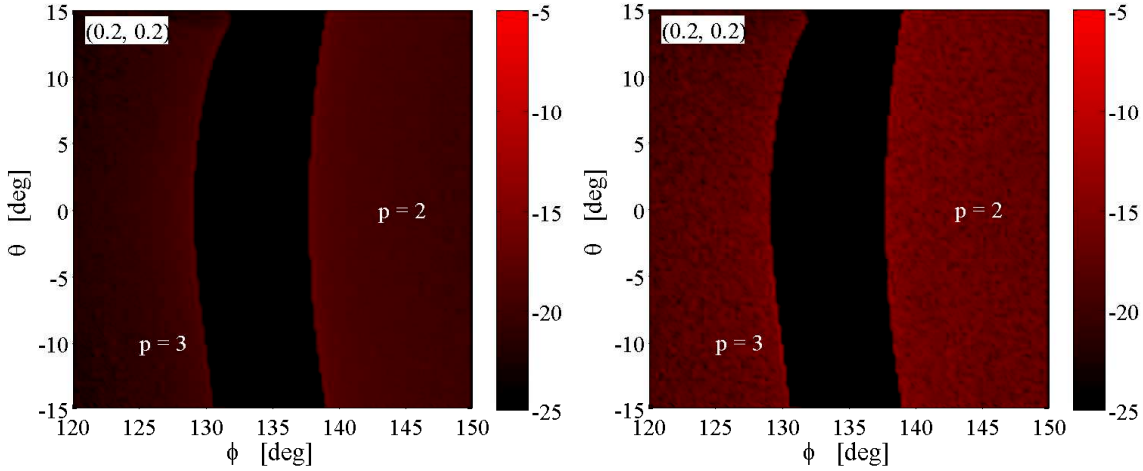

(a) Droplet **a** without interference.

(b) Droplet **a** with interference.

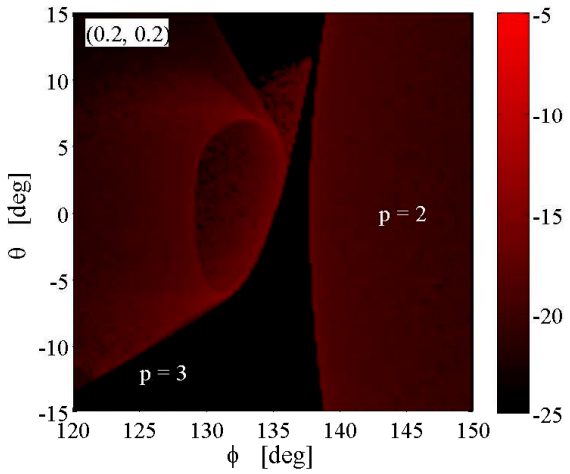

(c) Droplet **d** without interference.

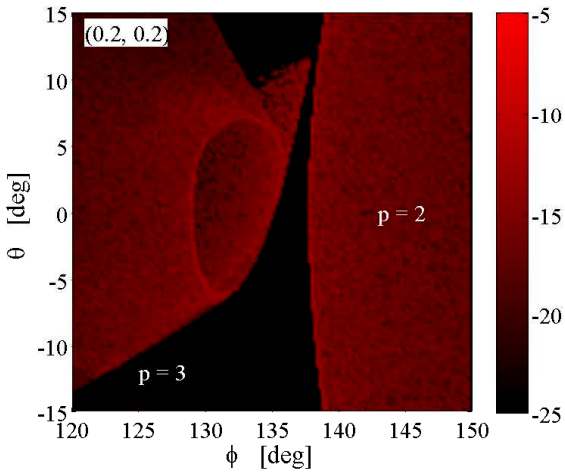

(d) Droplet **d** with interference.

Figure 5.2: Scattering patterns of a pendent droplet near rainbow angles simulated by SVCRM with the parameters in Tab. 5.1 and the number of emitted photons $N = 4 \times 10^7$.

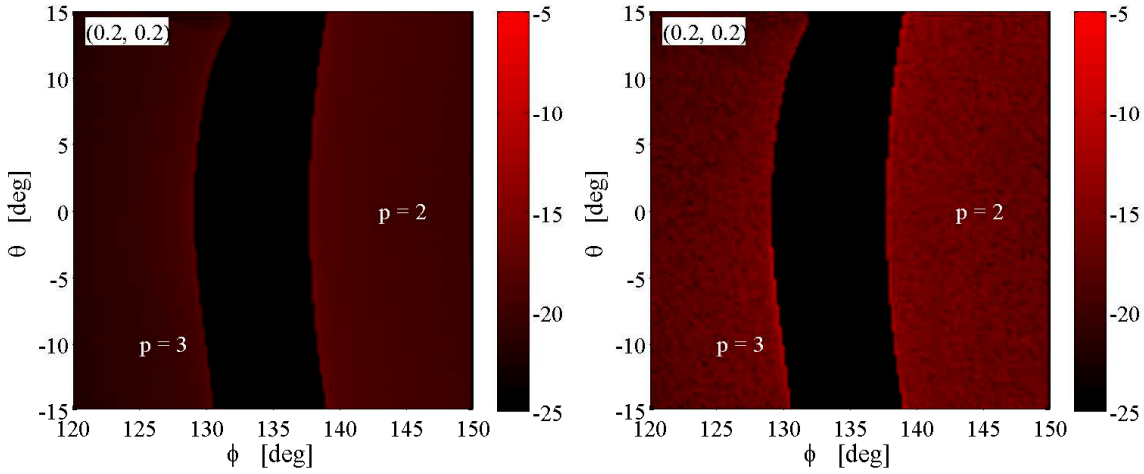

(a) Droplet **a** without interference.

(b) Droplet **a** with interference.

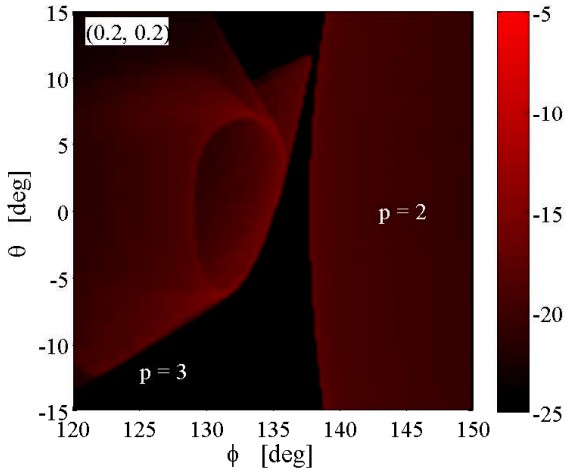

(c) Droplet **d** without interference.

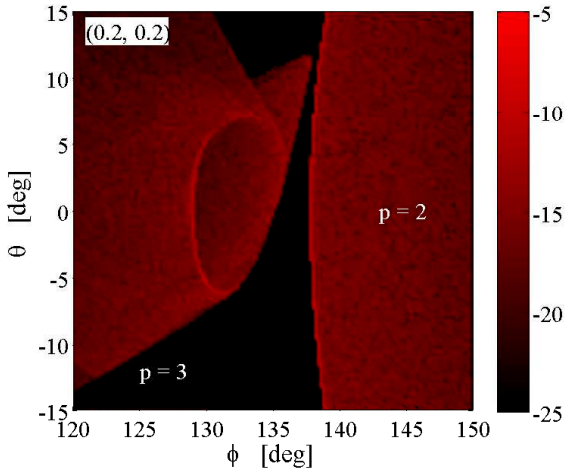

(d) Droplet **d** with interference.

Figure 5.3: Same parameter as Fig. 5.2 except the number of emitted photons $N = 4 \times 10^8$.

5.2.2 Influence of detection steps on the interference

To investigate the influence of the detection steps on the interference, we simplify here the pendent droplet to a sphere of radius R_e (Fig. 5.4(a)) and to an ellipsoid of two semi-axes a, c (Fig. 5.4(b)) which has the same curvature radii in the equatorial plane as the droplet.

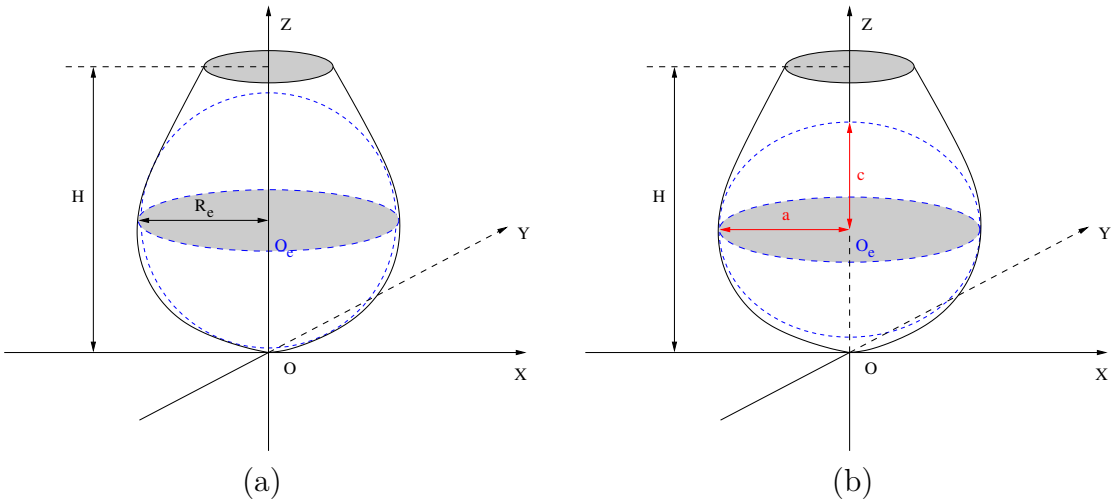

Figure 5.4: Pendent droplet simplified to a sphere or an ellipsoid.

We have calculated the scattering diagrams of the equivalent sphere and ellipsoid by the software VCRMEll2D for the droplet **a** and the droplet **d**. The scattering diagrams around the rainbow angles of a sphere are shown in Fig. 5.5. In this calculation, to avoid the high frequency due to the interference between different orders, only the rays of order $p = 2$ and 3 are considered. We find that the scattered intensity varies very fast with the scattering angle ϕ, especially in the range between 140° and 145°. This can be used to estimate the angular resolution C_ϕ. We count the number of the periods and the angle range $\delta\phi$; then we can calculate the average period of the oscillation. The average period obtained in such way is about 0.25°. That means the phase difference varies 2π in about each 0.25°. In the calculation by SVCRM, the phases of the photons arriving in the same box must be almost constant. That requires that the size of the box must be much smaller than the angle interval of a period. To satisfy this condition, tenth of the period is a conventional value in the numerical simulation. With this method, the detection angle steps are estimated with the sphere is 0.025° and given in Tab. 5.2.

To take into account the influence of the shape of the droplet in the determination of the detection steps, an equivalent ellipsoid has also been considered for the droplet **a** and droplet **d** . The scattering diagrams are also calculated with the software VCRMEll2D (Fig. (5.6). With the same procedure as above, the detection steps C_ϕ are found for the droplet **a** and droplet **d** and given in Tab. 5.2.

Comparing the detection steps, the angular resolution C_ϕ for the simulations of the intensity distributions near the equatorial plane of the droplet **a** and the droplet **d** should

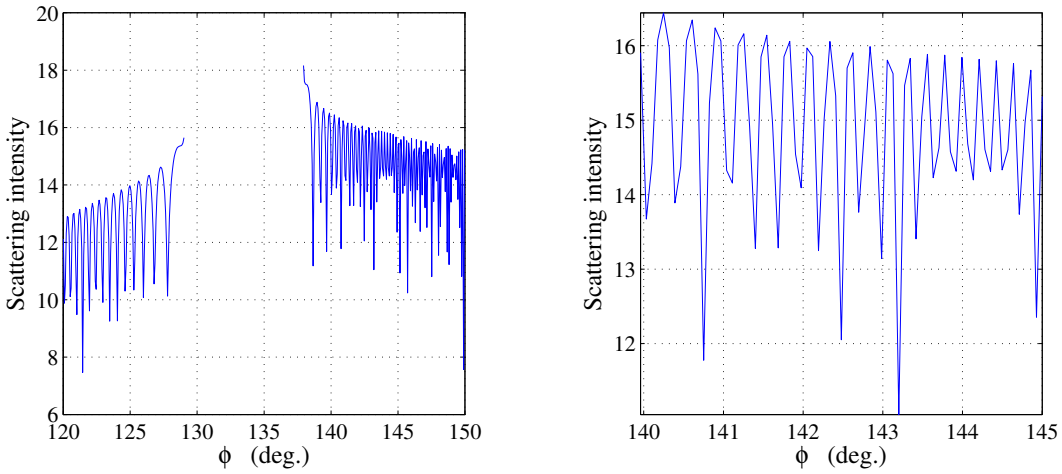

(a) Scattering diagrams of a sphere with the radius of droplet **a** .

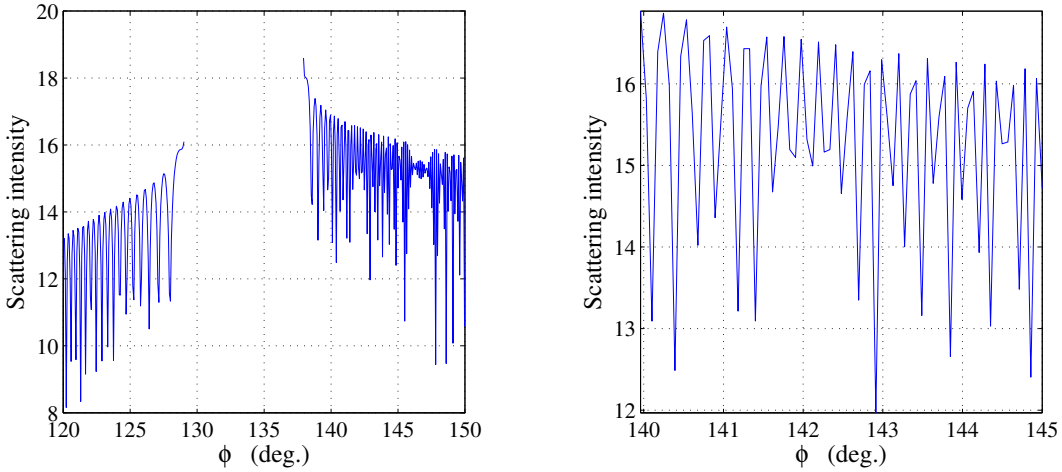

(b) Scattering diagrams of a sphere with the radius of droplet **d** .

Figure 5.5: Scattering diagrams of a sphere with the same radius as a pendent droplet calculated by software VCRMll2D. The figures on the right are just a zoom on the first order rainbow in the figure on the left.

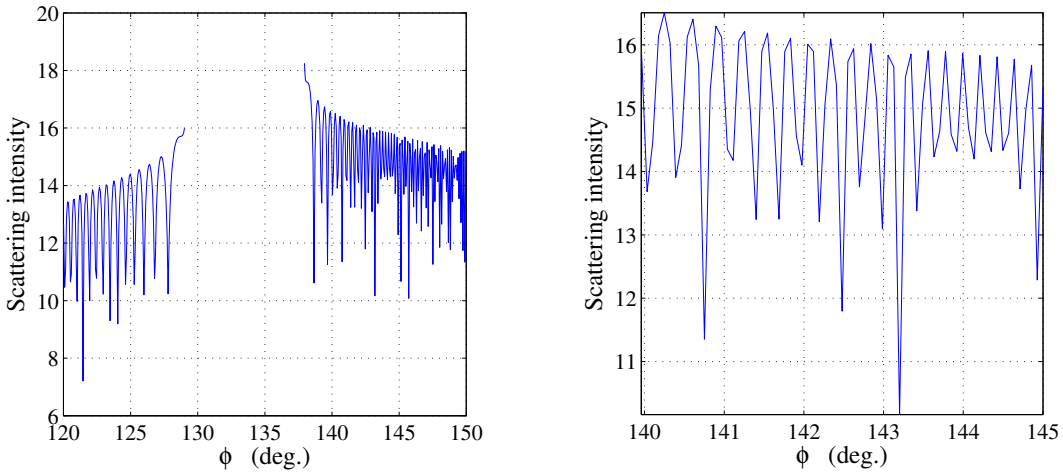

(a) Scattering diagrams of an ellipsoid with the semi-axes (a, c) of droplet **a** .

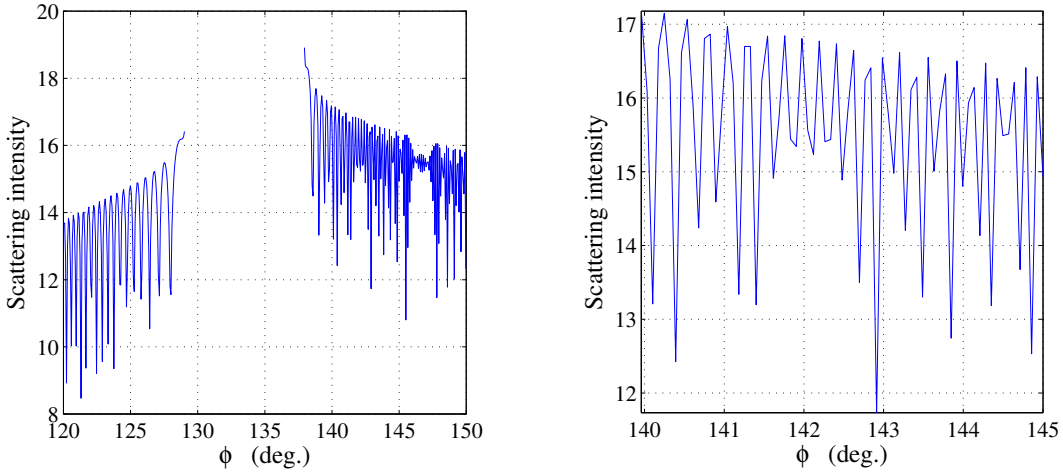

(d) Scattering diagrams of an ellipsoid with the semi-axes (a, c) of droplet **d** .

Figure 5.6: Scattering diagrams of a ellipsoid with the same semi-axes of a pendent droplet calculated by software VCRMll2D. The figures on the right are just a zoom on the first order rainbow in the figure on the left.

be better than 0.02°. Evidently, the steps of 0.2° for θ and ϕ in Fig. 5.2 and Fig. 5.3 are too large. This explains why the interference is not observed.

Table 5.2: Detection steps of angle ϕ for the sphere and the ellipsoid simplified from the droplet **a** and the droplet **d**.

Parameters	**droplet a**		**droplet d**	
	sphere	**ellipsoid**	**sphere**	**ellipsoid**
$a(\mu\text{m})$	541.15	541.15	671.16	671.16
$c(\mu\text{m})$	541.15	1634.36	671.16	2815.08
c/a	1.0000	3.0202	1.0000	4.1944
$C_\phi(°)$	0.025	0.025	0.025	0.0208
ϕ	$[140°, 145°]$			
p	$2, 3$			

Once the angular resolution C_ϕ is determined, the angular resolution C_θ needs to considered also. For the scattering patterns near the equatorial plane and around the rainbow angles, the variation of the intensity in θ direction is much slower, especially for the droplet **a** and the first order rainbow of the droplet **d**. The step on θ may be larger. However, this detection step can not be estimated with the same manner as for ϕ since we have no means to calculate the scattering diagrams in this direction.

To determine the angular resolution C_θ, we do directly the simulation of the scattering patterns with our code SVCRM with different steps on θ. To reduce the calculation time and focus on the problem, we illuminate the droplet with a rectangular piece of light: the height of illuminated region is only 10% of the equatorial radius of the droplet. Tab. 5.3 compiles the simulation parameters.

Fig. 5.7 and Fig. 5.8 show the scattering patterns of the droplet **a** respectively in the cases of with and without interference calculated with 4 different steps $C_\theta = 1.0°, 0.5°, 0.2°$ and $0.1°$. We can see that when the interference is not taken into account (Fig. 5.7), if the step on θ is sufficiently small ($C_\theta = 0.2°$ and $0.1°$, two images at the bottom of Fig. 5.7) we can see clearly in the first order rainbow (right part) the return of the rays. But if the step is too big, $C_\theta = 1°$ top-left image, the return of the rays can not be identified.

When the interference is taken into account, even for a large step on θ ($C_\theta = 1°$ for example) the fringes in the two rainbows are clearly visible (Fig. 5.8). The refinement of the resolution on θ improves little the fringes. However, if we examine attentively the first order rainbow (right part of the images), we do not find fringes near the up and bottom borders of the first order rainbow, because the rays of order $p = 2$ arrive

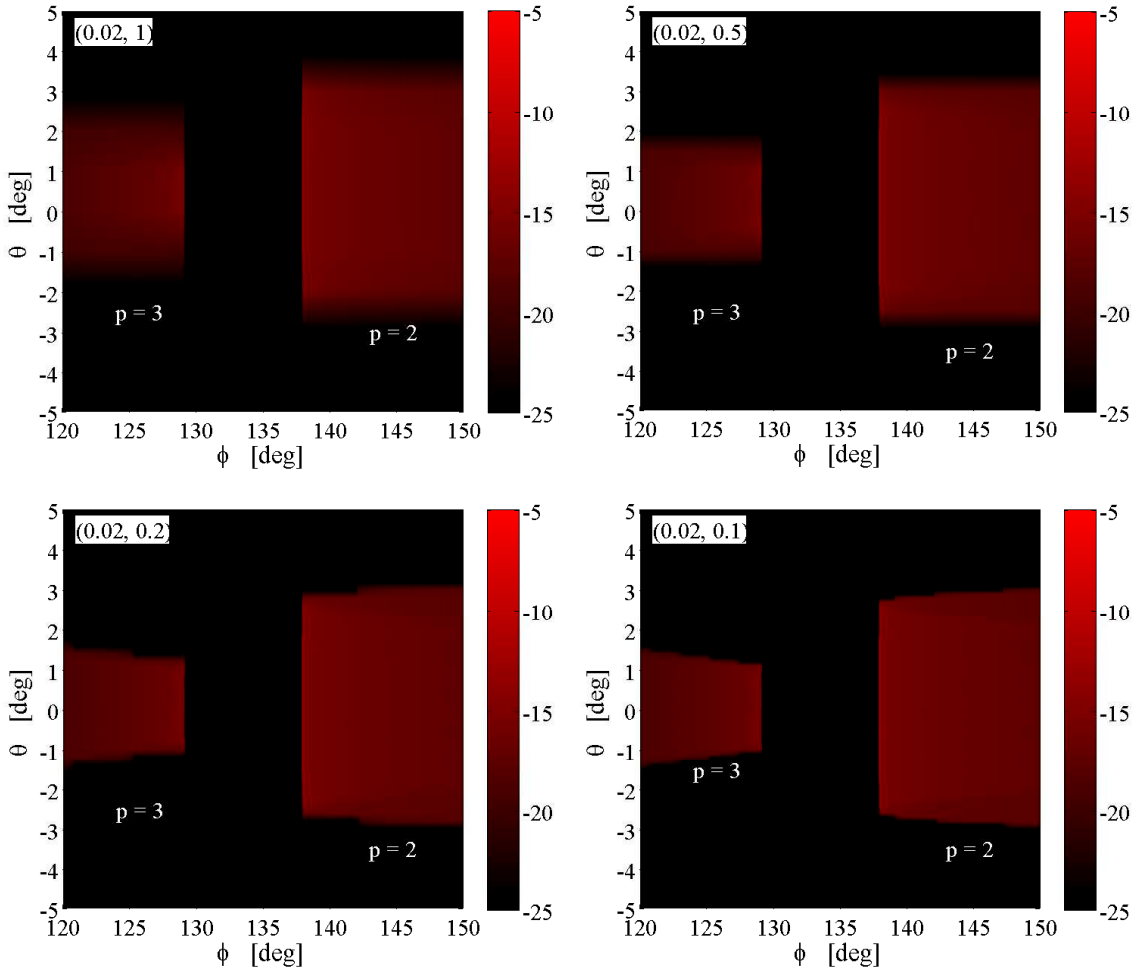

Figure 5.7: Influence of detection steps on the scattering patterns **without interference** near the equatorial plane of the pendent droplet **a** with the parameters in Tab. 5.3 with $Z_e = 592.54$.

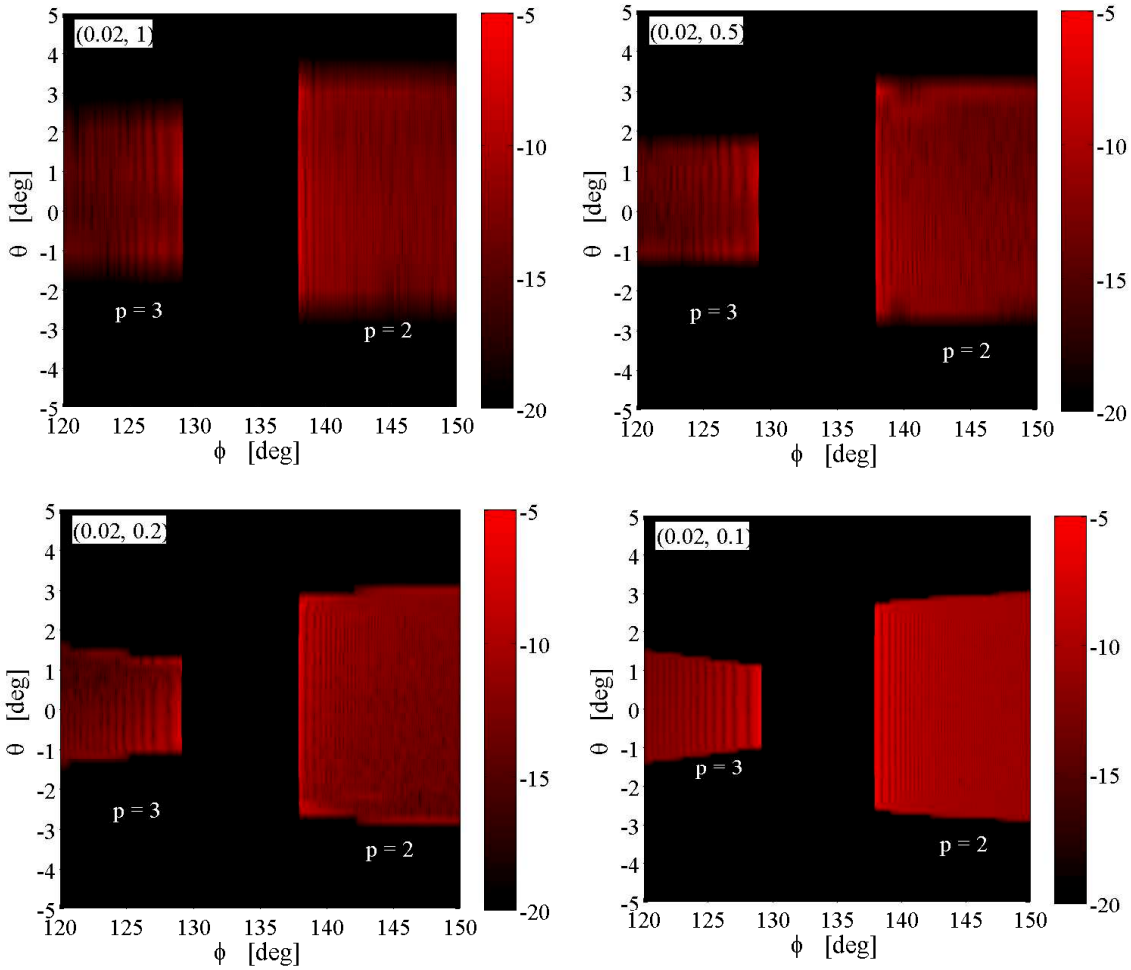

Figure 5.8: Same as Fig. 5.7 but **with interference**.

Table 5.3: Parameters for the scattering intensity near the equatorial plane of droplet

parameters	**Values**			
$\lambda(\mu\text{m})$	0.6328			
m	1.333			
$(x_c, y_c, z_c)(\mu\text{m})$	$(-5000, 0, Z_e)$			
$z_s(\mu\text{m})$	$[-0.05R_e, 0.05R_e]$			
$y_s(\mu\text{m})$	$[-R_e, R_e]$			
θ	$[-5°, 5°]$			
ϕ	$[120°, 150°]$			
C_ϕ	$0.02°$			
C_θ	$1.0°$	$0.5°$	$0.2°$	$0.1°$
p	$2, 3$			
N	4×10^8			

only once in this region.

We would note also that the height of the first order rainbow is about two times larger than the second order rainbow. This can be explained by the fact that the rays of order $p = 3$ experience one internal reflection more than the rays of order $p = 2$, so they are more converged than the rays of the first order rainbow.

The same simulation has been done for the droplet **d** and the scattering patterns are shown in Fig. 5.9 and Fig. 5.10, respectively for the case with and without interference. Similar comments can be done except that the height of the first order rainbow is about three times larger than the second order rainbow instead of two times for the droplet **a**. This can be explained by the fact that the vertical curvature of the droplet **d** is smaller (larger curvature radius). The exploitation of the mechanism of scattering by the decomposition of the scattering patterns in the section 5.4 may help better understanding.

5.3 Effect of detection steps and number of photons

Now we simulate the scattering patterns in the real experimental condition and compare them to those obtained by experiment. A plane wave illuminates the whole droplet and we observe the scattering in the region of the first order and second order rainbows.

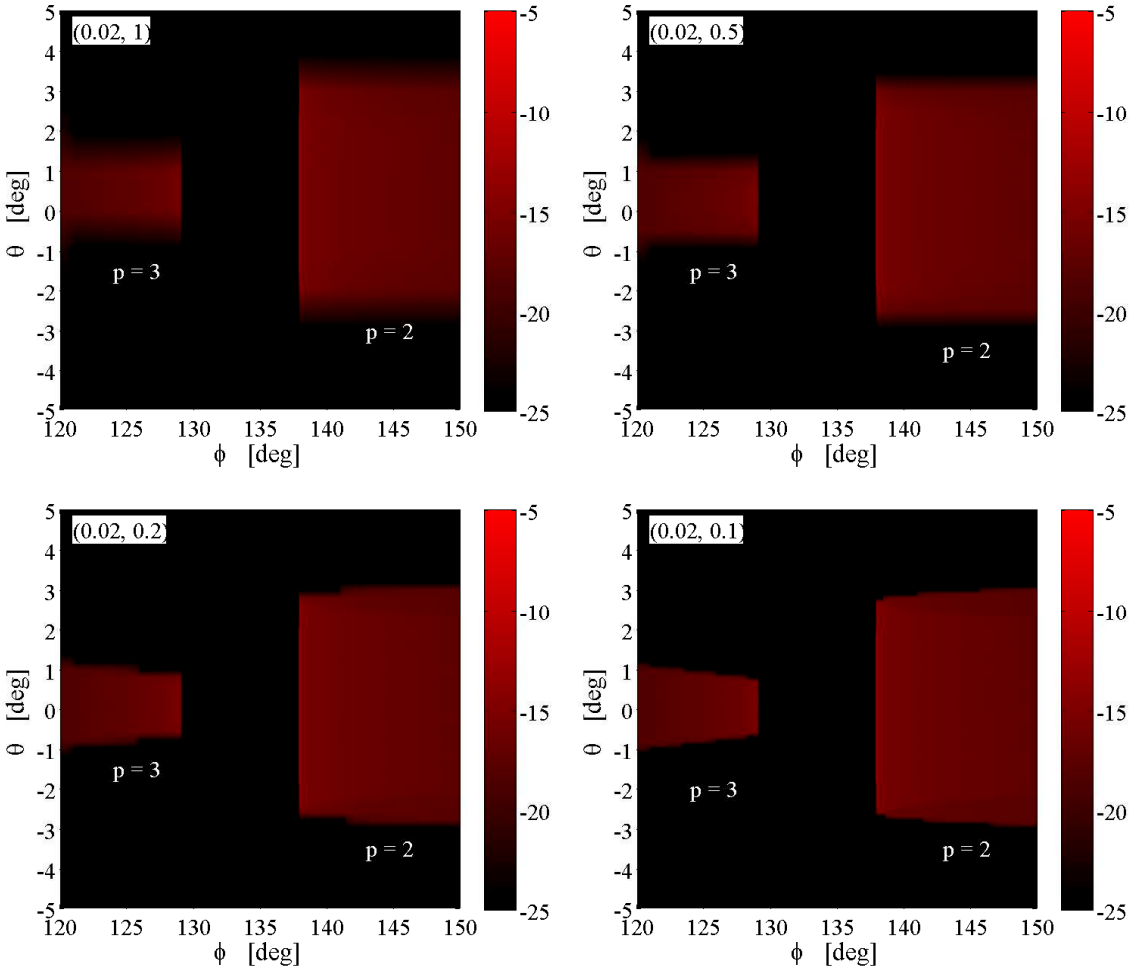

Figure 5.9: Same as Fig. 5.7 but for droplet **d** .

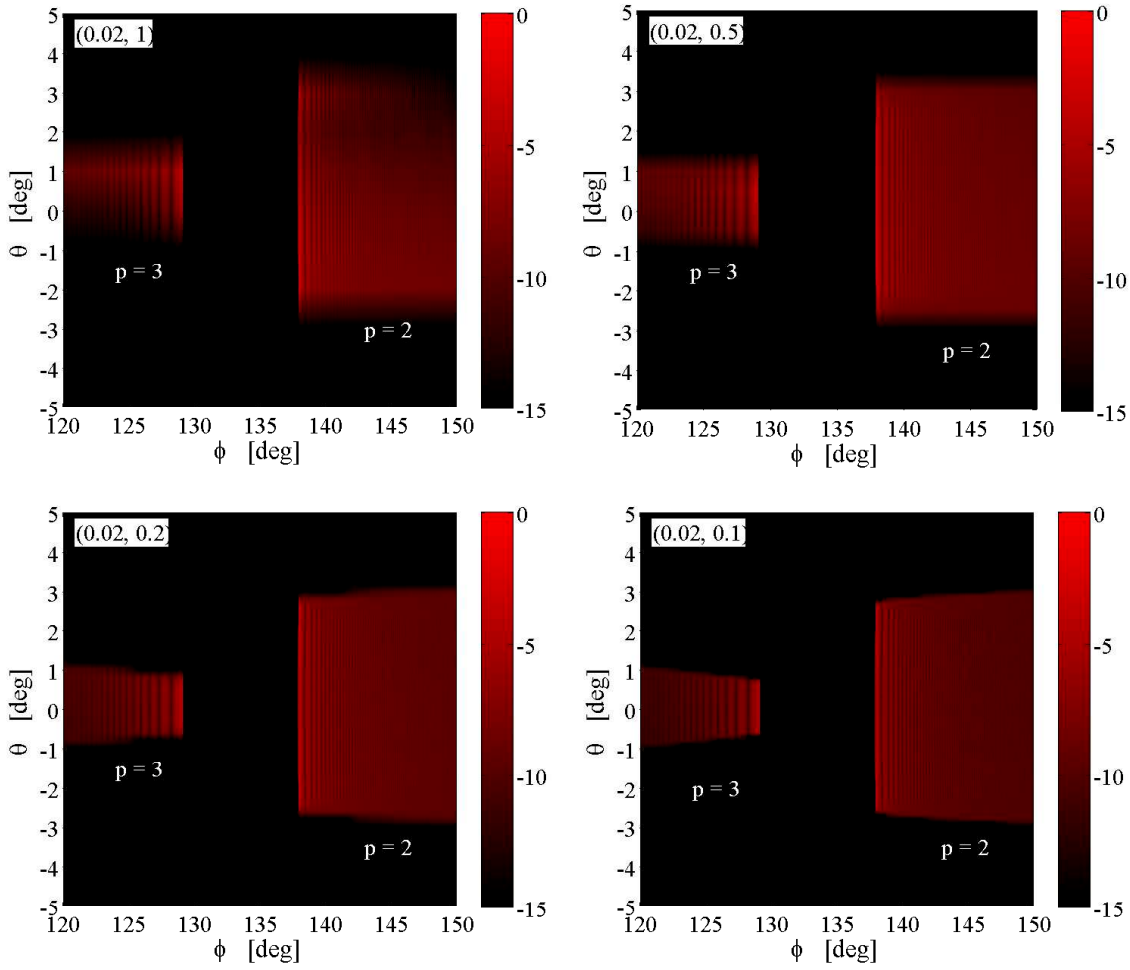

Figure 5.10: Same as Fig. 5.9 but **with interference**.

The simulations have been done with different detections steps C_θ and C_ϕ. The simulated scattering patterns for the droplet **a** and the droplet **d** are shown in Figs. 5.11-5.14. In each figure nine images are given for 9 pairs of the detection steps in Tab. 5.4. The other parameters for the simulation are compiled in Tab. 5.5.

Table 5.4: Various detection steps for the scattering patterns of droplet around the rainbow angles with the same emitted photons.

C_ϕ	C_θ
0.02°	0.1°
	0.05°
	0.02°
0.01°	0.1°
	0.05°
	0.02°
0.005°	0.1°
	0.05°
	0.02°

Table 5.5: Parameters for the scattering patterns around the rainbow angles with different detection steps.

Parameters	**Values**
$\lambda(\mu\text{m})$	0.6328
m	1.333
$(x_c, y_c, z_c)(\mu\text{m})$	$(-5000, 0, 0)$
$z_s(\mu\text{m})$	$[0, H]$
$y_s(\mu\text{m})$	$[-R_e, R_e]$
θ	$[-15^\circ, 15^\circ]$
ϕ	$[120^\circ, 150^\circ]$
p	$2, 3$
N	8×10^8

By simple comparison of the simulated scattering patterns in these four figures with

those obtained experimentally (droplets **a** and **d** in Fig. 4.3), we find that their skeletons correspond fairly good. The two-order rainbows of the droplet **a** are almost parallel and slightly deformed compared to that of a sphere. The first order rainbow of the droplet **d** remains almost the same as the droplet **a** but its second order rainbow is twisted as that found in the experiment. However the bright trait going from the center to the bottom right in the experimental pattern is not found or so remarkable in the simulated pattern. The reason is to be examined.

If there is no interference, the 9 images in Fig. 5.11 are almost the same. When the interference is considered (Fig. 5.12), we find that only the vertical part of the fringes are visible if C_θ (step on θ) is relatively big (0.1° in the left column). When C_θ is sufficiently small (0.05° in the middle column), whole fringe patterns are clear. But when both C_ϕ and C_θ are small, the fringes are no longer clear (see the image on bottom right for example). This is because the number of emitted photons in each box is not sufficient. To support this reasoning, we give a rough estimate on the number of emitted photons in each box. For a big particle, the great part of scattered light is concentrated in a small angle in the forward direction. We may suppose that 5% of photons arrive in the region of the image ($30^\circ \times 30^\circ$). If the whole droplet is illuminated with 8×10^8 photons, the average number of photons in each box is $8 \times 10^8/9 \times 10^6 \sim 5$ photons. This is evidently too few.

Similar comments can be made for Figs. 5.13 and 5.14. The rule of the step C_θ is more remarkable. By comparison of the scattering patterns calculated with $C_\theta = 0.1^\circ$ and 0.05° (left and middle columns in Fig. 5.14), we find that the fringes in the up and bottom parts of the circle in the second order rainbow are better for a small C_θ.

To examine the effect of the number of emitted photons we show in Fig. 5.15 the scattering patterns calculated with $N = 2 \times 10^9$. The two images on the right column are obtained with the same steps (C_ϕ, C_θ) as the last two images in the bottom of Fig. 5.14. It is clear that the scattering patterns with 2×10^9 photons are better than those simulated with 8×10^8 photons.

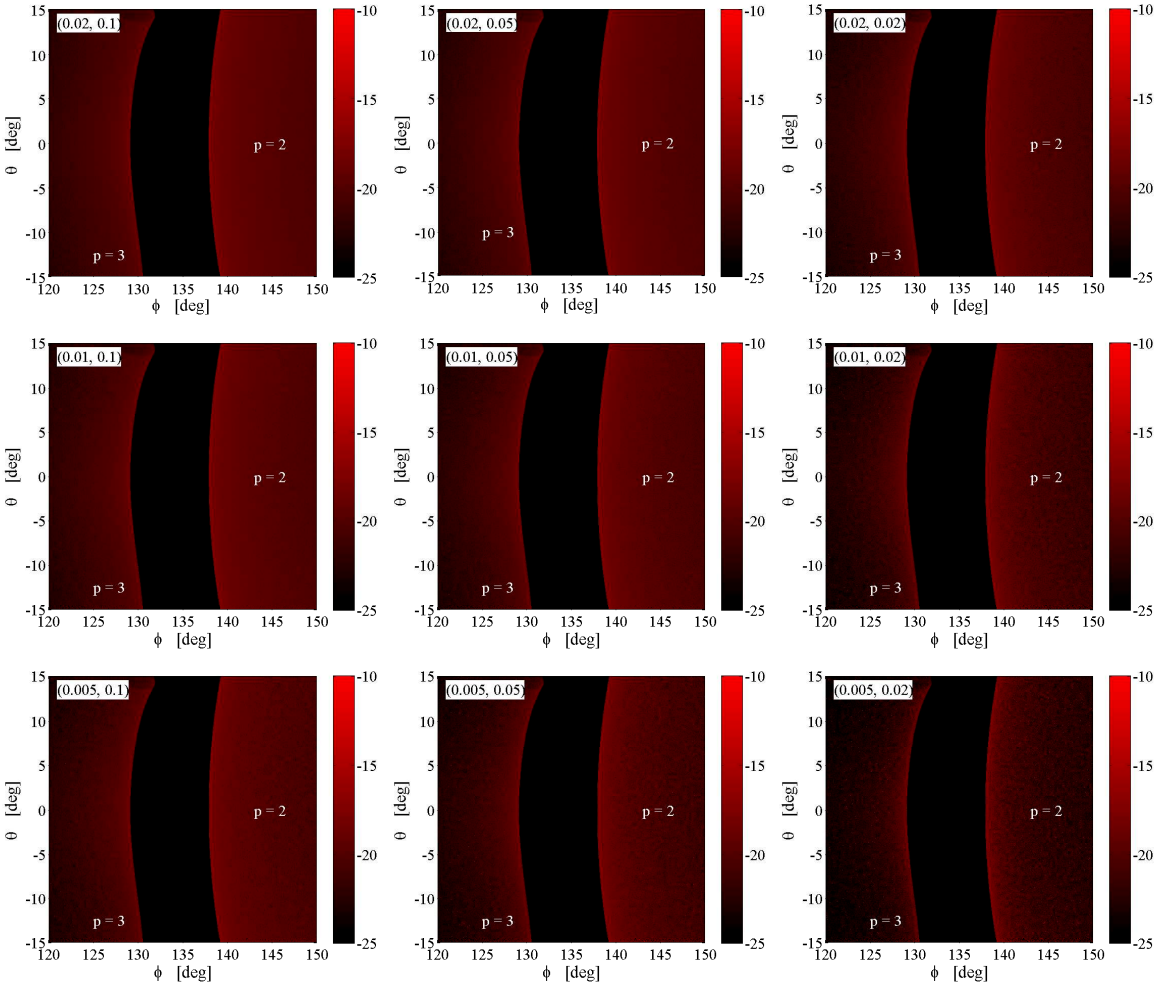

Figure 5.11: Scattering patterns **without interference** of the pendent droplet **a** with parameters given in Tab. 5.4 and $R_e = 541.15$ μm, $H = 989.86$ μm. The 9 images correspond to the simulation with 9 pairs of detection steps (C_ϕ, C_θ) given in Tab. 5.4

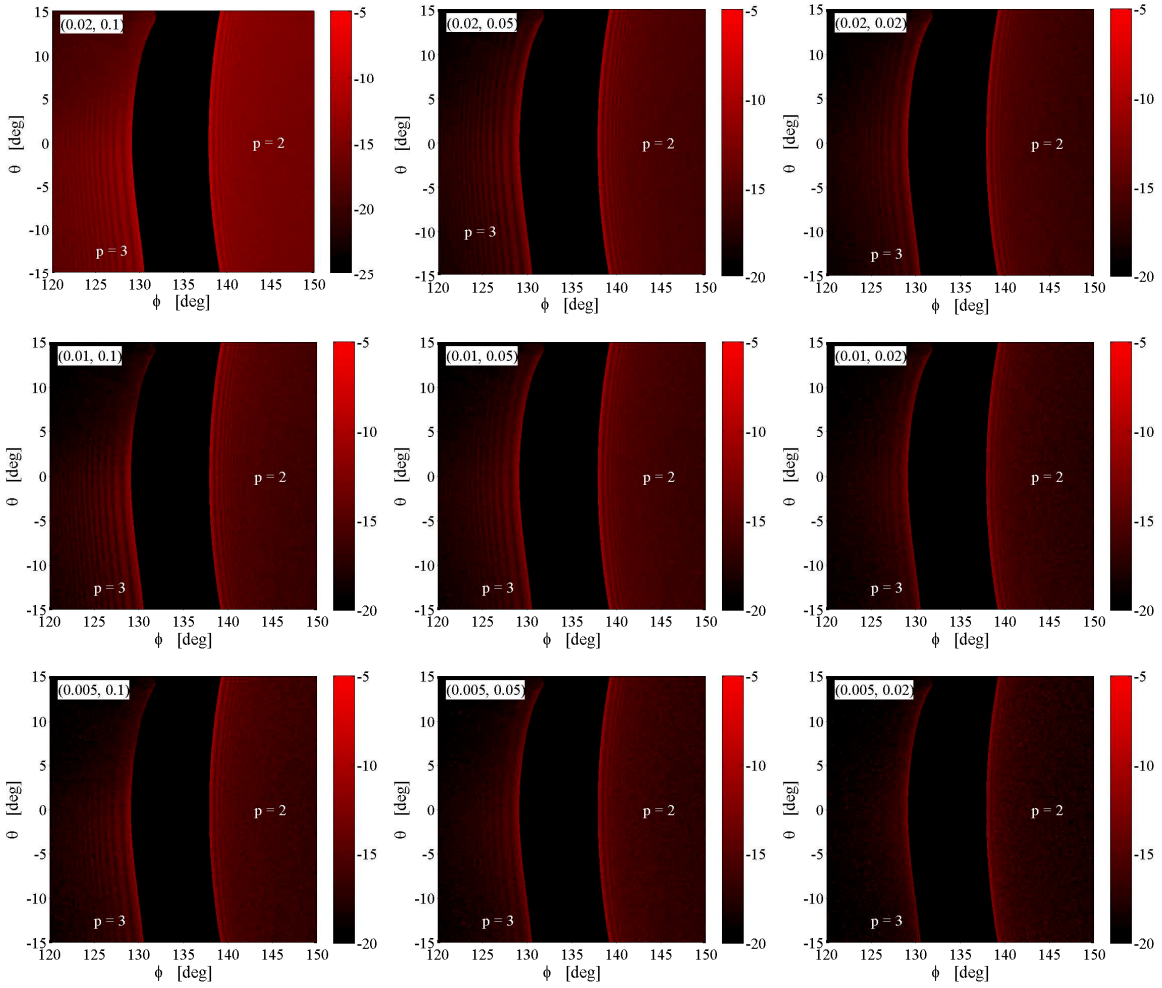

Figure 5.12: Same as Fig. 5.11 but with interference.

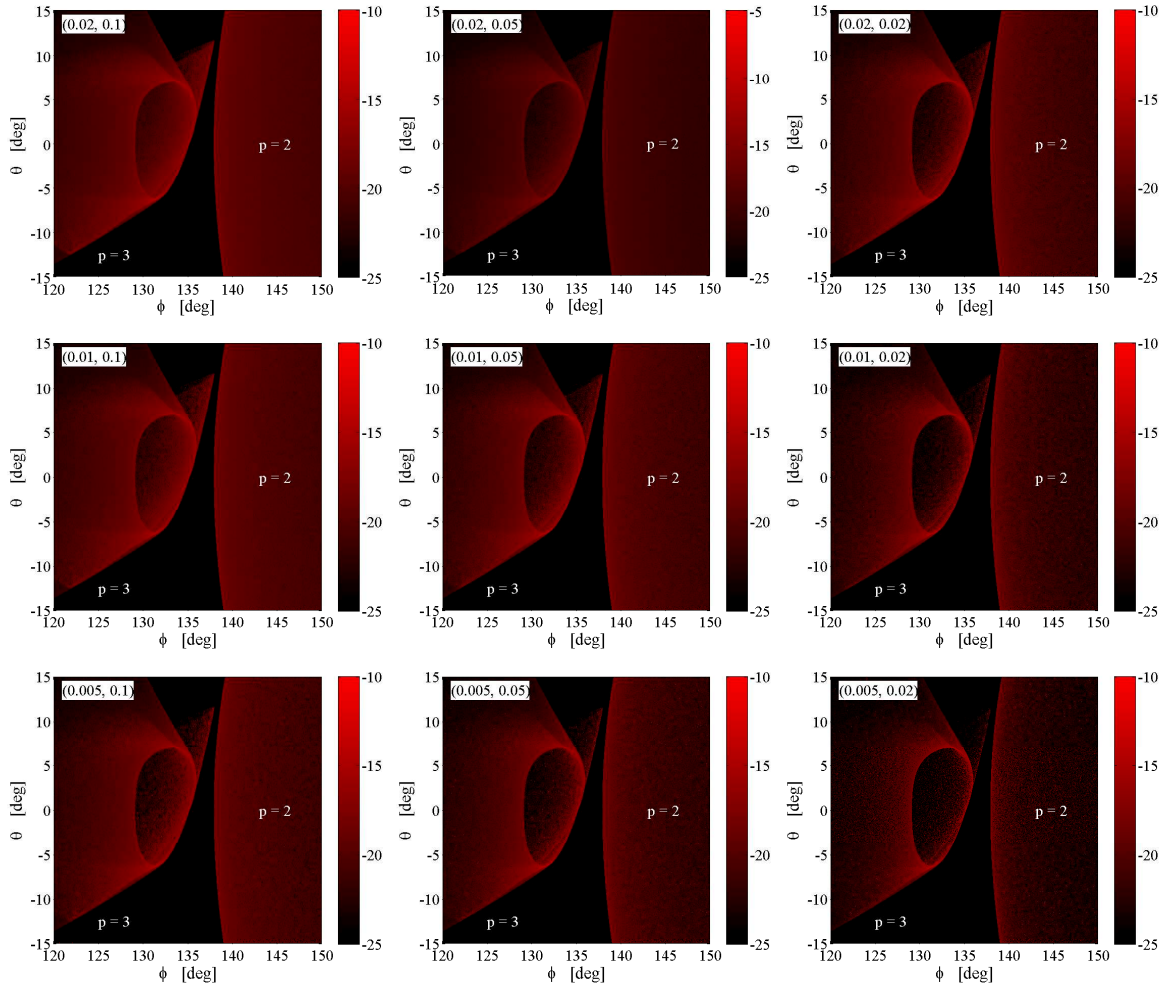

Figure 5.13: Same as Fig. 5.11 but for the droplet **d** with $R_e = 671.16$ μm and $H = 1707.68$ μm

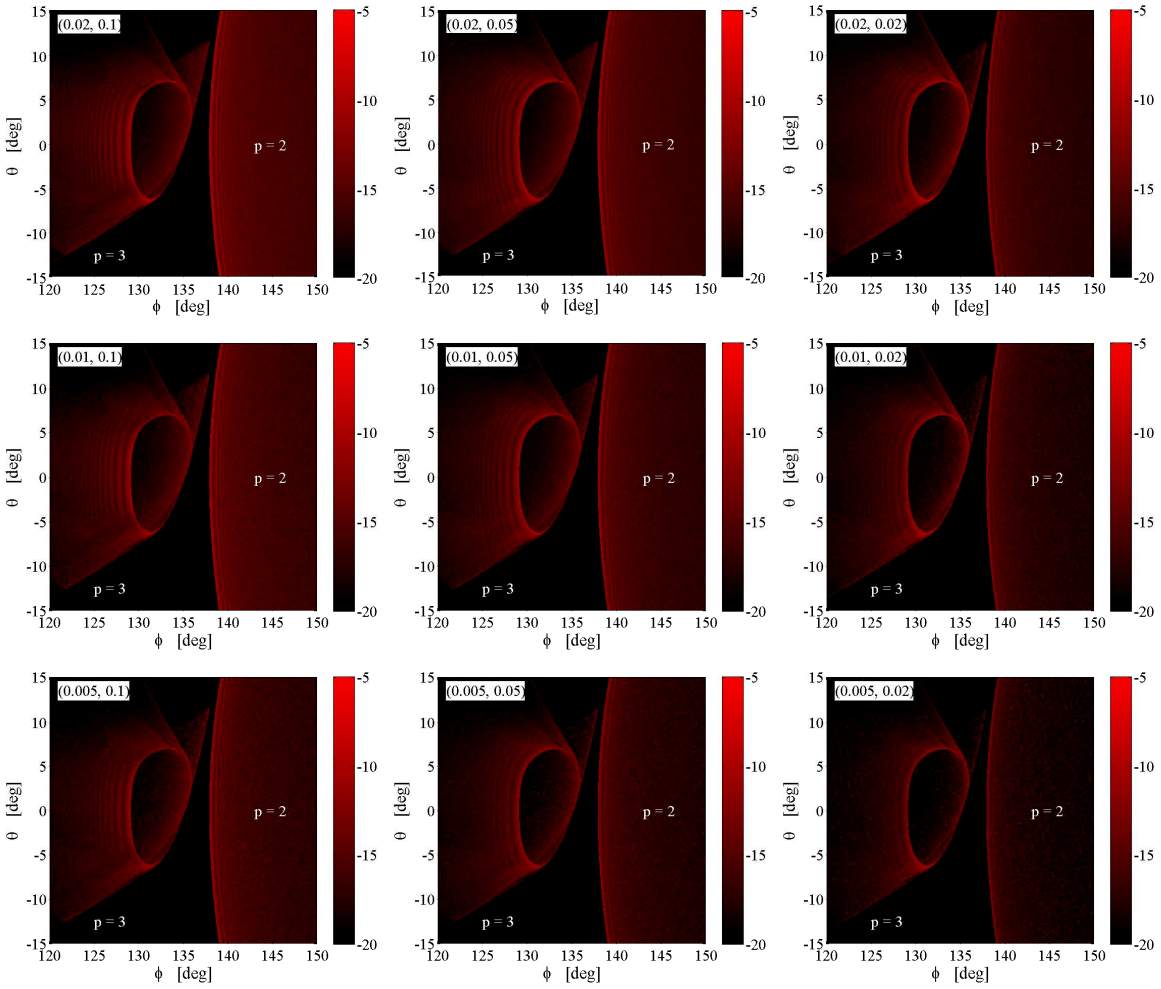

Figure 5.14: Same as Fig. 5.13 but with interference.

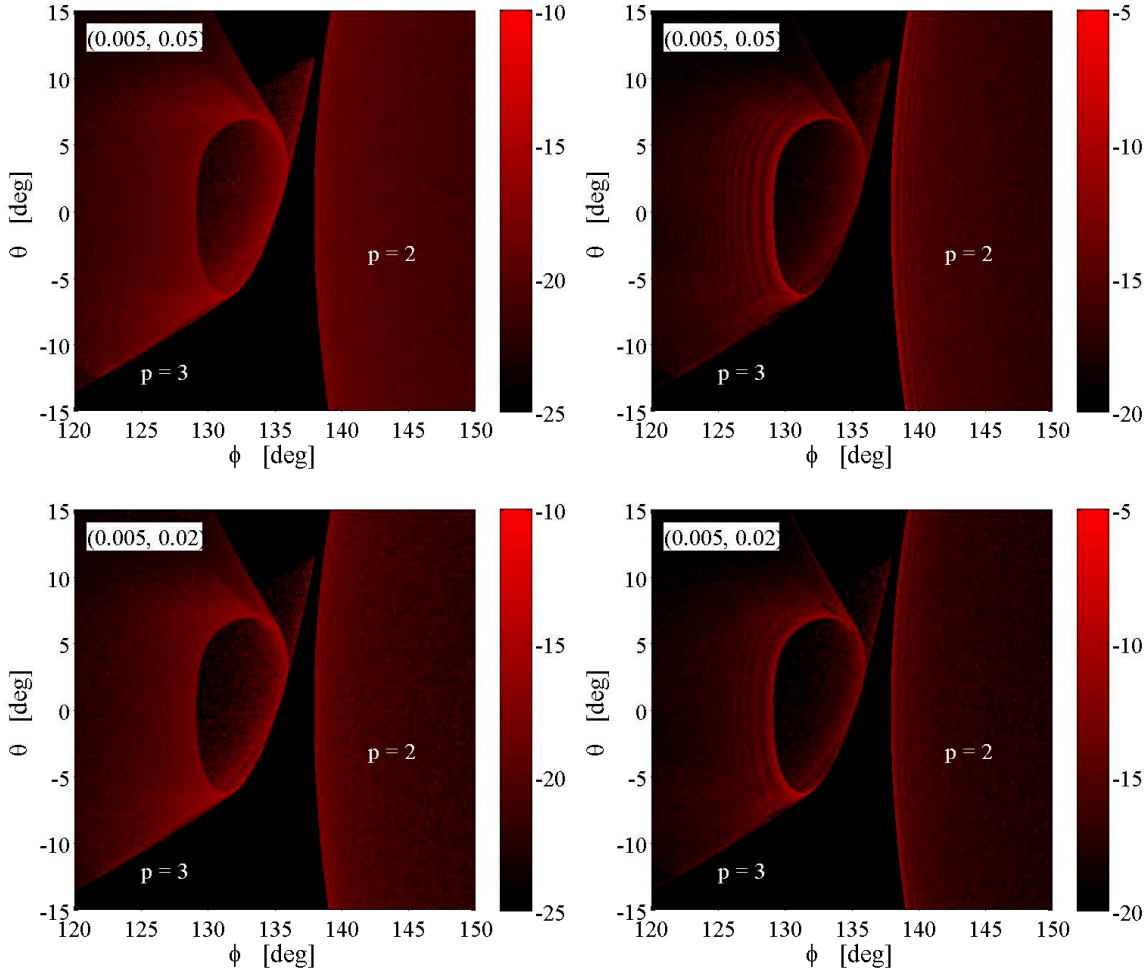

Figure 5.15: Same parameters as the last images in Fig. 5.14 but the number of emitted photons is $N = 2 \times 10^9$.

Finally, to examine the effect of the detection steps and the number of emitted photons, we reduce proportionally the size of the droplet, i.e. with the same geometry but divide the height H and the radius R_e of the droplet **d** by 10. The variation of the phase will be much slower and the fringes will be larger. The simulated scattering patterns with parameters given in Tab. 5.6 are shown in Fig. 5.16. It is clear that the interference fringes are much larger and discernable with even larger steps.

Table 5.6: Parameters for the calculation of the scattering patterns of the **reduced droplets**.

Droplet / **Parameters**	**a**	**d**
$R_e(\mu\text{m})$	54.115	67.116
$H(\mu\text{m})$	98.986	170.768
(C_ϕ, C_θ)	$(0.1^\circ, 0.01^\circ)$	
p	$2, 3$	
N	2×10^9	

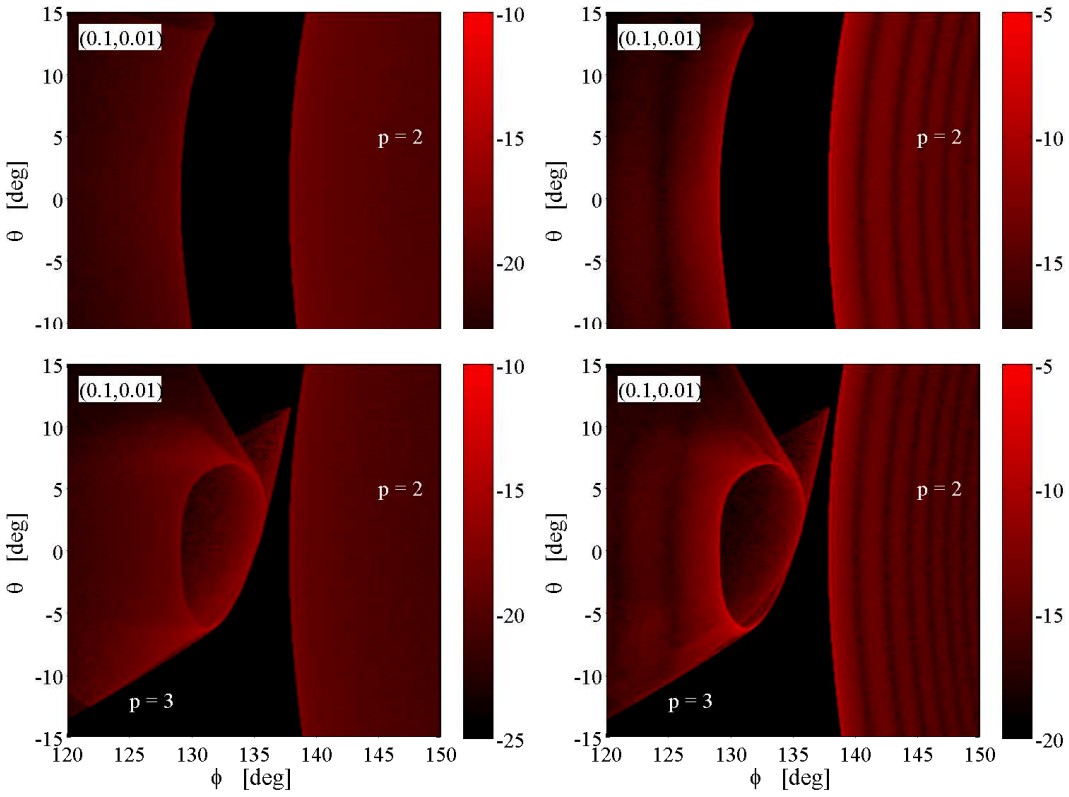

Figure 5.16: Scattering patterns of the reduced droplets **a** (top) and **d** (bottom) with the parameters in Tab. 5.6.

5.4 Decomposition of scattering patterns

To reveal the scattering mechanism and identify the contribution of the rays from different parts of the droplet, we illuminate the droplet by a thin rectangular top-hat beam and observe the scattering pattern. In our simulation, the droplets **a** and **d** are divided into 8 horizontal areas. Each area has the same height equal to 1/8 of the droplet height, i.e. $H/8$ (Fig. 5.17). The scattering patterns of the two droplets simulated with the parameters in Tab. 5.7 are shown in Figs. 5.18-5.21.

For the droplet **a**, the area 5 is the area including the equatorial plane and the equatorial plane of the droplet **d** is in the area 4. There is no scattered light in the areas 1 and 2 for the droplet **a** (in Figs. 5.18 and 5.19) because the light from these regions do not contribute to the first and the second rainbows. When we move the illuminated area, the first order rainbow and the second order rainbow move in the opposite direction. When the illuminated area is relatively far from the equatorial plane (areas 1, 2, 7, and 8 in Figs. 5.20 and 5.21), the scattering patterns of the droplet **d** is much complicated than that for the droplet **a**.

Table 5.7: Parameters for the calculation of the scattering patterns of partially illuminated droplets.

Areas	**Area** i $(i = 1 - 8)$
$z_c(\mu\text{m})$	$(2i-1)H/16$
$(x_c, y_c)(\mu\text{m})$	$(-5000, 0)$
$z_s(\mu\text{m})$	$[-H/16, H/16]$
$y_s(\mu\text{m})$	$[-R_e, R_e]$
N	2×10^9
θ	$[-15^\circ, 15^\circ]$
ϕ	$[120^\circ, 150^\circ]$
C_ϕ	0.02°

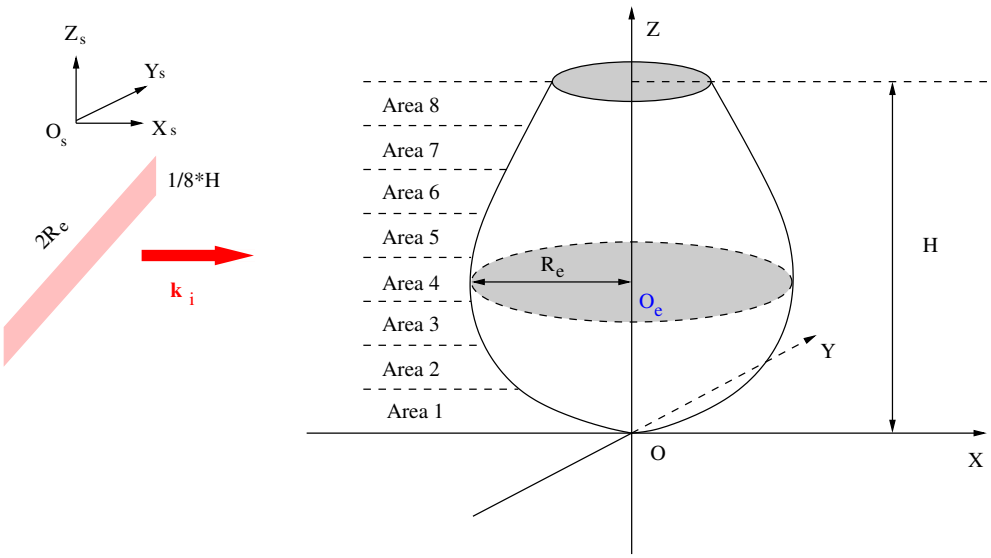

Figure 5.17: A schematic to show a droplet is illuminated by a rectangular top-hat beam in 8 different regions.

Finally, we show in Figs. 5.22 and 5.23 the scattering patterns near the rainbow angles for the four droplets described in Chapter 4. The simulation is done with the parameters in Tab. 5.8. These four scattering patterns correspond well those obtained experimentally (Fig. 4.3).

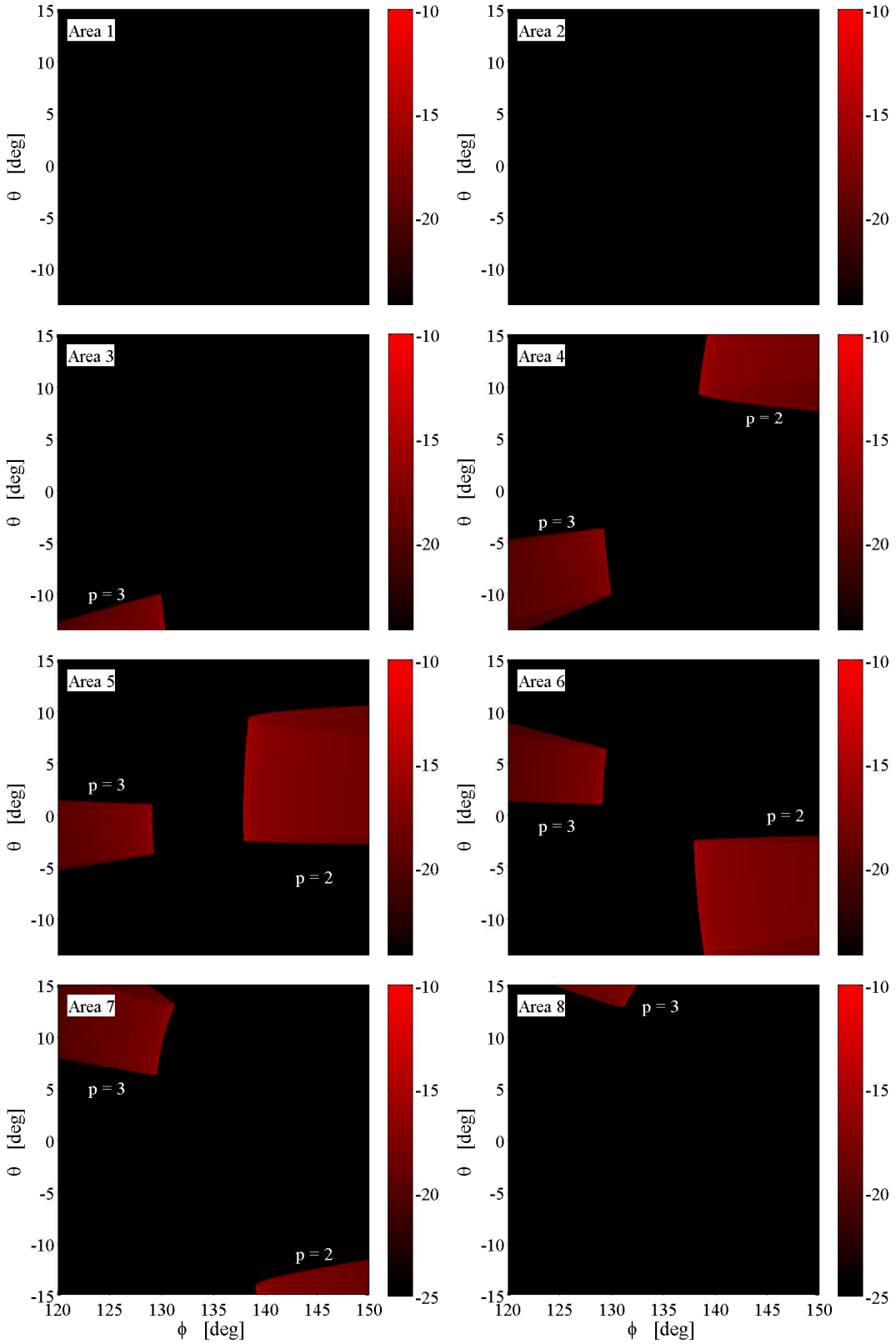

Figure 5.18: Scattering patterns **without interference** when the **droplet a** is illuminated by a thin rectangular to-hat beam at different. The detection step $C_\theta = 0.05$ and the other parameters are given in Tab. 5.7.

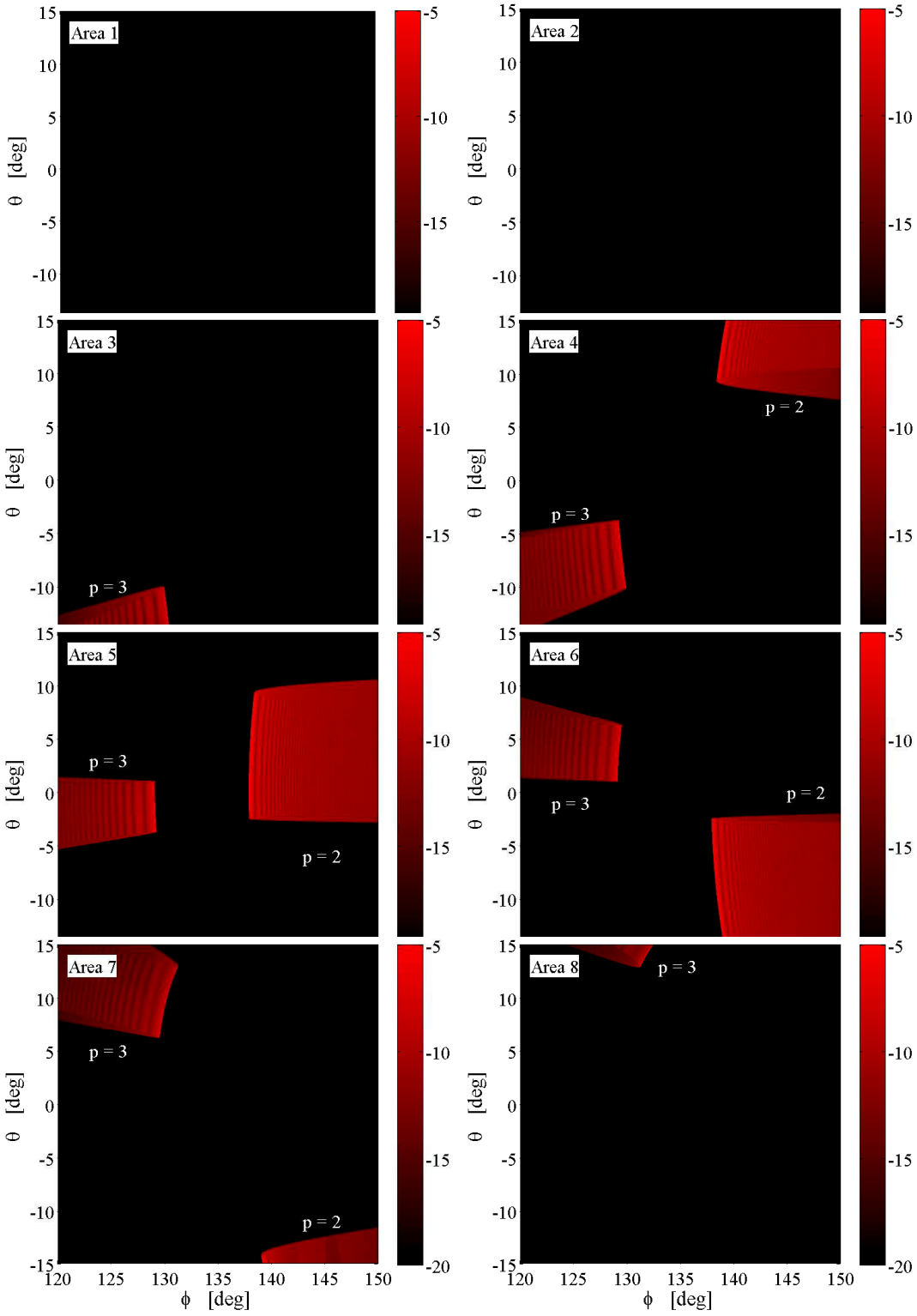

Figure 5.19: Same as Fig. 5.18 but **with interference**.

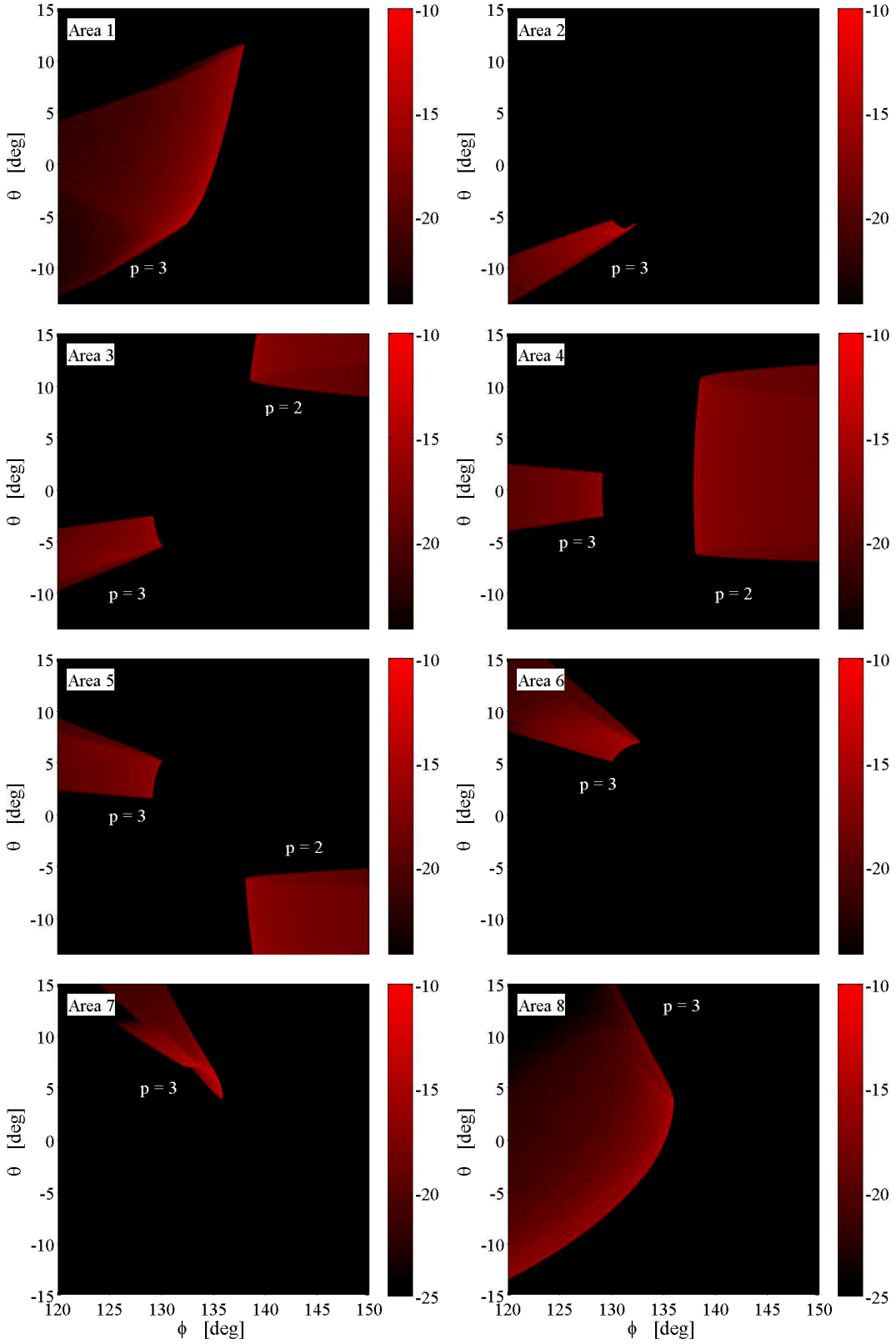

Figure 5.20: Same as Fig. 5.18 but for **droplet d**.

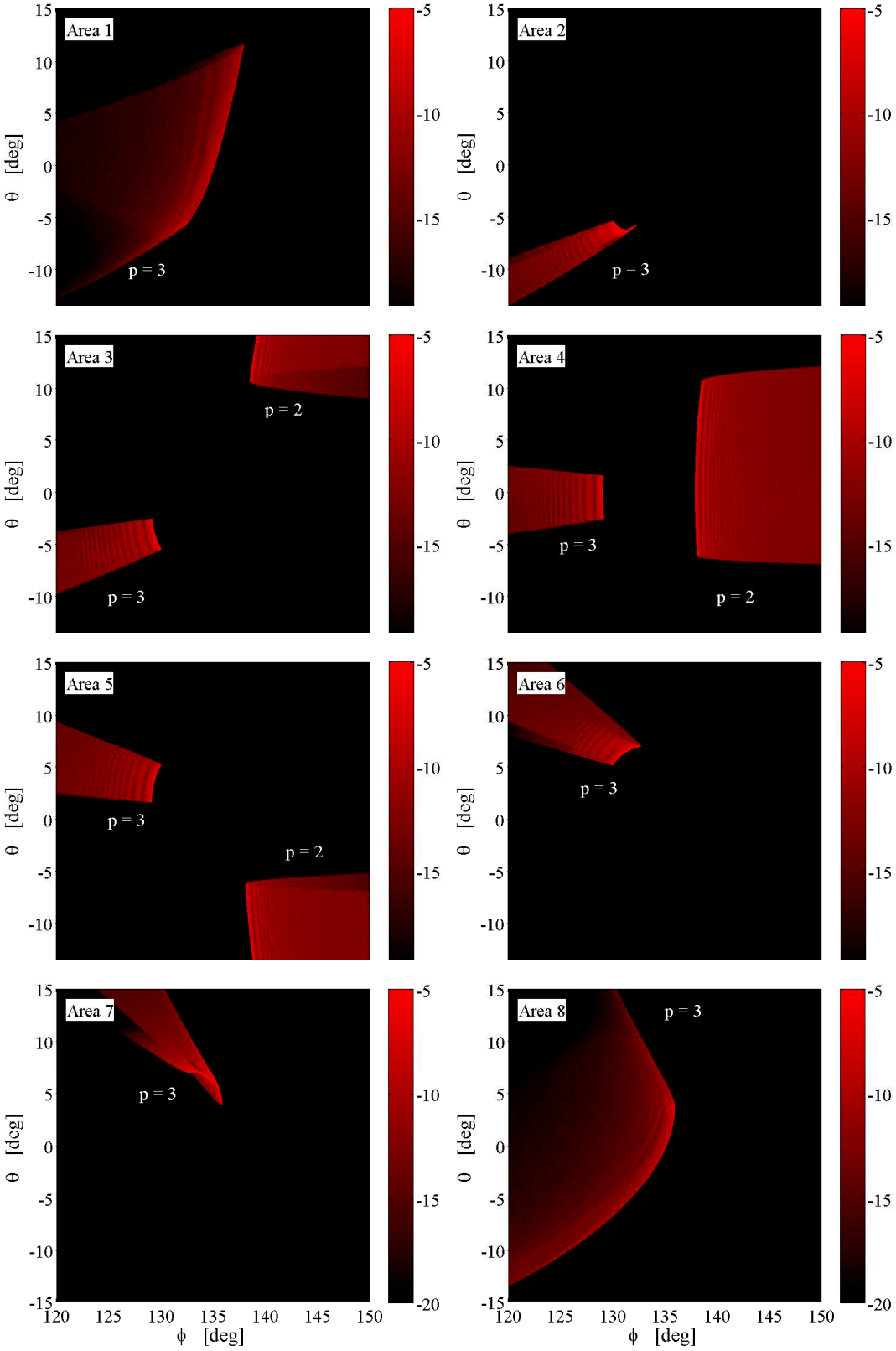

Figure 5.21: Same as Fig.5.18 but **with interference**.

Table 5.8: Parameters for the simulation of scattering patterns around the rainbow angles of the 4 droplets.

Droplet / **Parameters**	**a**	**b**	**c**	**d**
$R_e(\mu\text{m})$	541.15	589.83	631.45	671.16
$H(\mu\text{m})$	989.86	1173.53	1332.83	1707.68
$\lambda(\mu\text{m})$	0.6328			
m	1.333			
$(x_c, y_c, z_c)(\mu\text{m})$	$(-5000, 0, Z_e)$			
$z_s(\mu\text{m})$	$[0, H]$			
$y_s(\mu\text{m})$	$[-R_e, R_e]$			
θ	$[-15°, 15°]$			
ϕ	$[120°, 150°]$			
(C_ϕ, C_θ)	$(0.02°, 0.02°)$			
p	$2, 3$			
N	2×10^9			

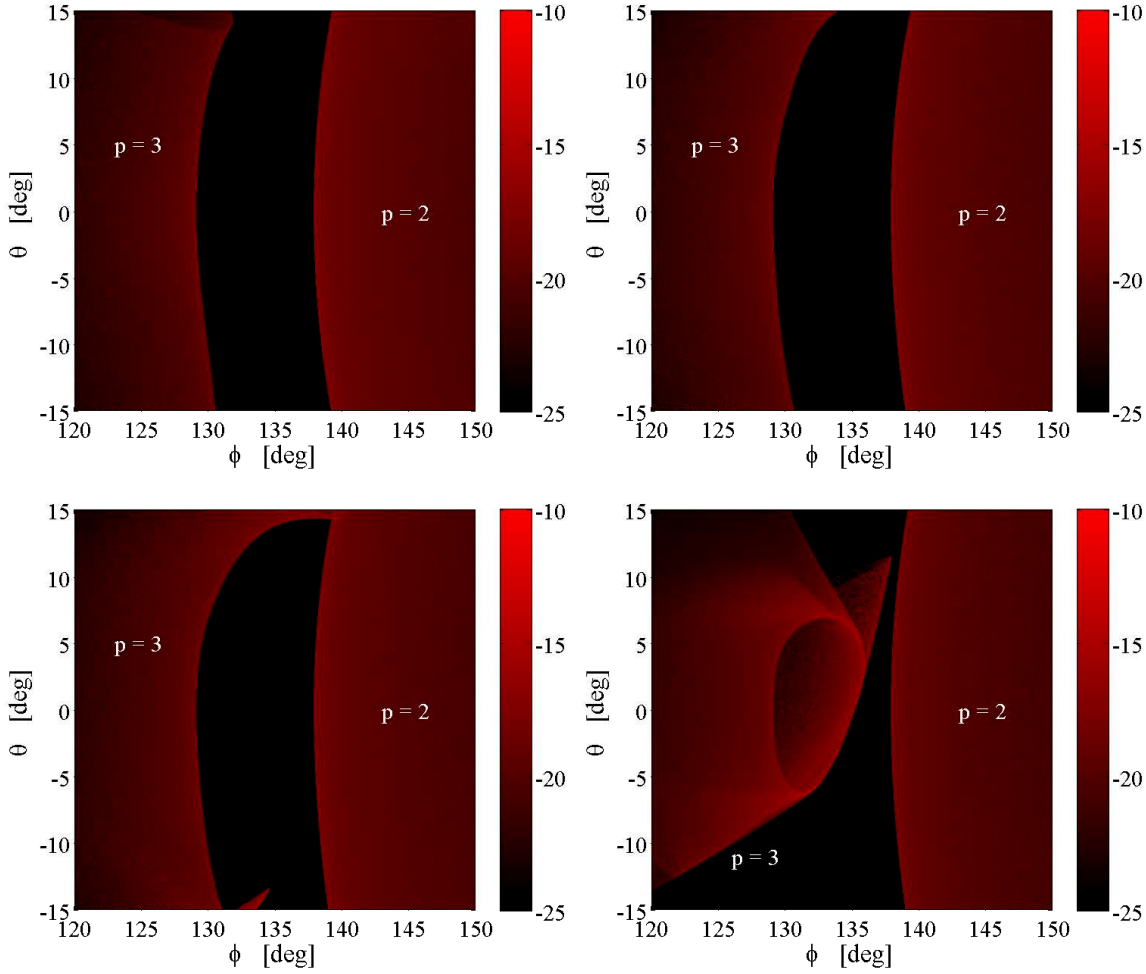

Figure 5.22: Scattering patterns **without interference** around the rainbow angles of the 4 droplets with the parameters in Tab. 5.8.

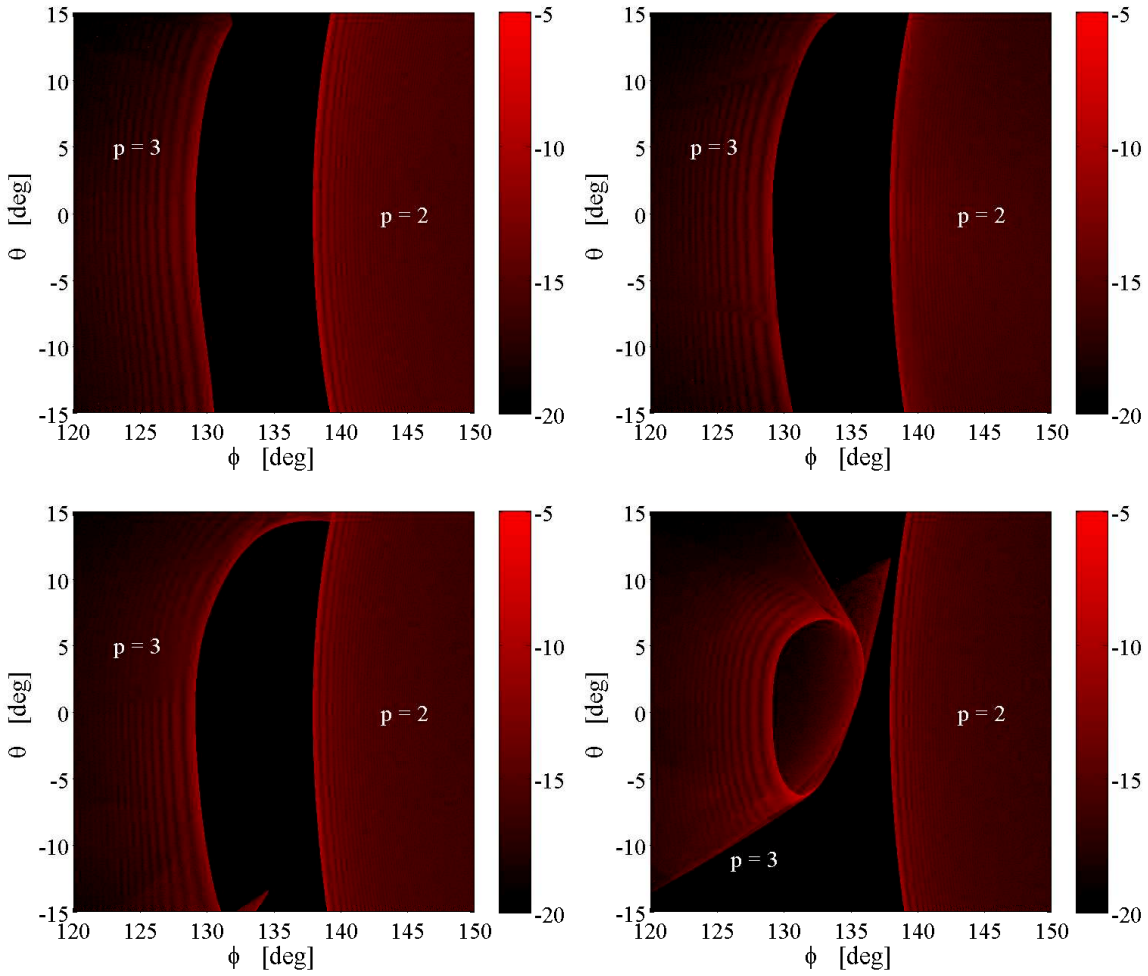

Figure 5.23: Same as Fig. 5.22 but **with interference**.

5.5 Scattering patterns in the forward direction

Now we show in Fig. 5.24 and Fig. 5.25 the scattering patterns of the 4 droplets in the forward direction simulated with the parameters given in Tab. 5.9. Whether the droplet is similar to a sphere or not, the intensity distribution without interference (shown in Fig. 5.24) is continuous along both θ and along ϕ while that with interference (seen in Fig. 5.25) is not, maybe it is caused by interference cancellation.

However, we have identified that the curved part in the lower part is due to the first order rays $p = 1$. More the droplet is deformed, more the bow is curved.

Furthermore, we observe clearly the Airy-like bows [59] in the curved part. But they are not visible for 4 droplets in Fig. 5.25 because of the resolution of the image. If we zoom in the bow of the droplet **d**, we can see clearly the Airy-like bows (Fig. 5.26).

Table 5.9: Parameters for the calculation of the scattering patterns droplets in the forward direction.

droplet / parameters	**a, b, c, d**
θ	$[-45°, 45°]$
ϕ	$[-45°, 45°]$
(C_ϕ, C_θ)	$(0.05°, 0.01°)$
p	$0, 1$
N	$2{\times}10^9$

5.6 Conclusion

In this chapter, the scattering patterns under different conditions are analyzed. The effect of detection steps, number of emitted photons, incident area of the wave as well as the shapes of droplets on scattered intensity distribution are investigated to valid the code of SVCRM, which can deal with the scattering problem of large irregular particles with a smooth surface in three dimensions.

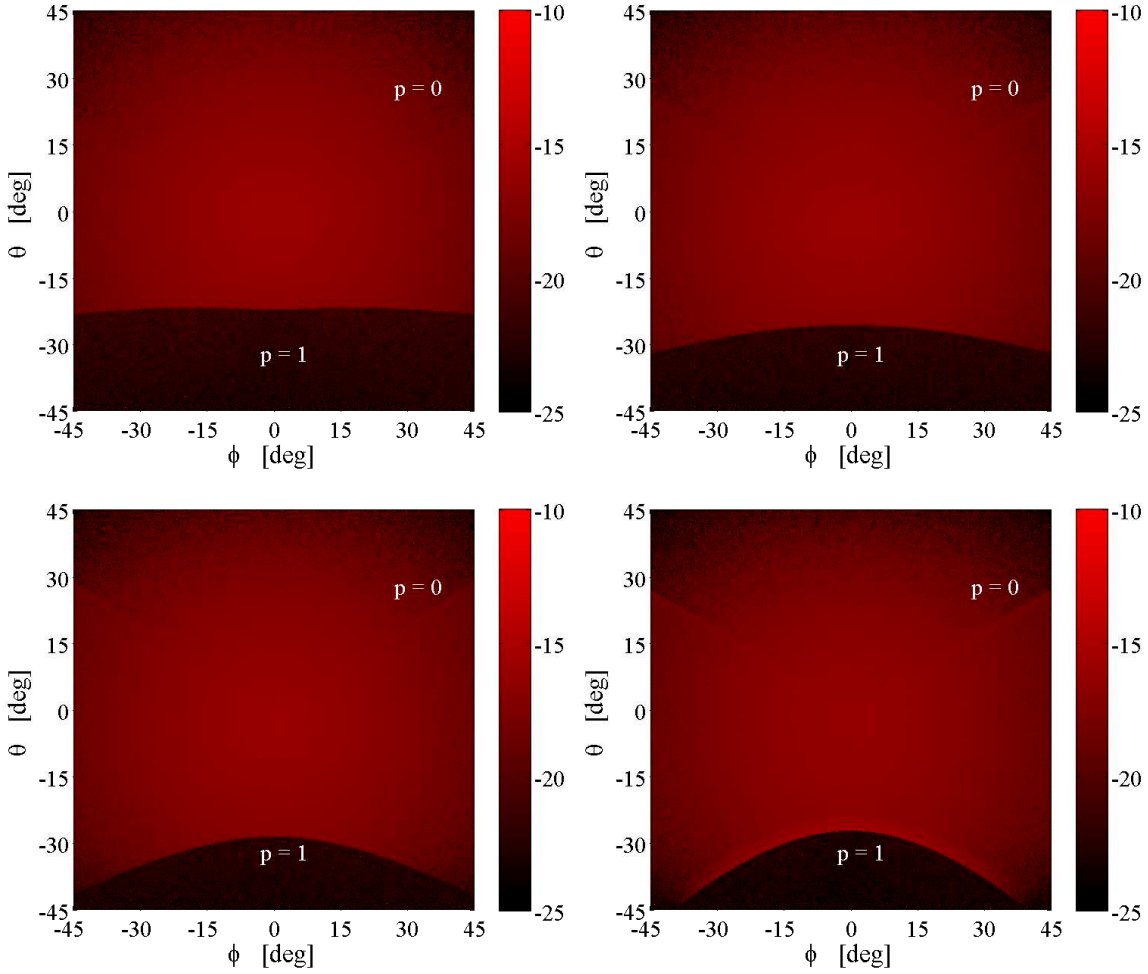

Figure 5.24: Scattering patterns **without interference** in forward direction of the 4 droplets with the parameters in Tab. 5.9.

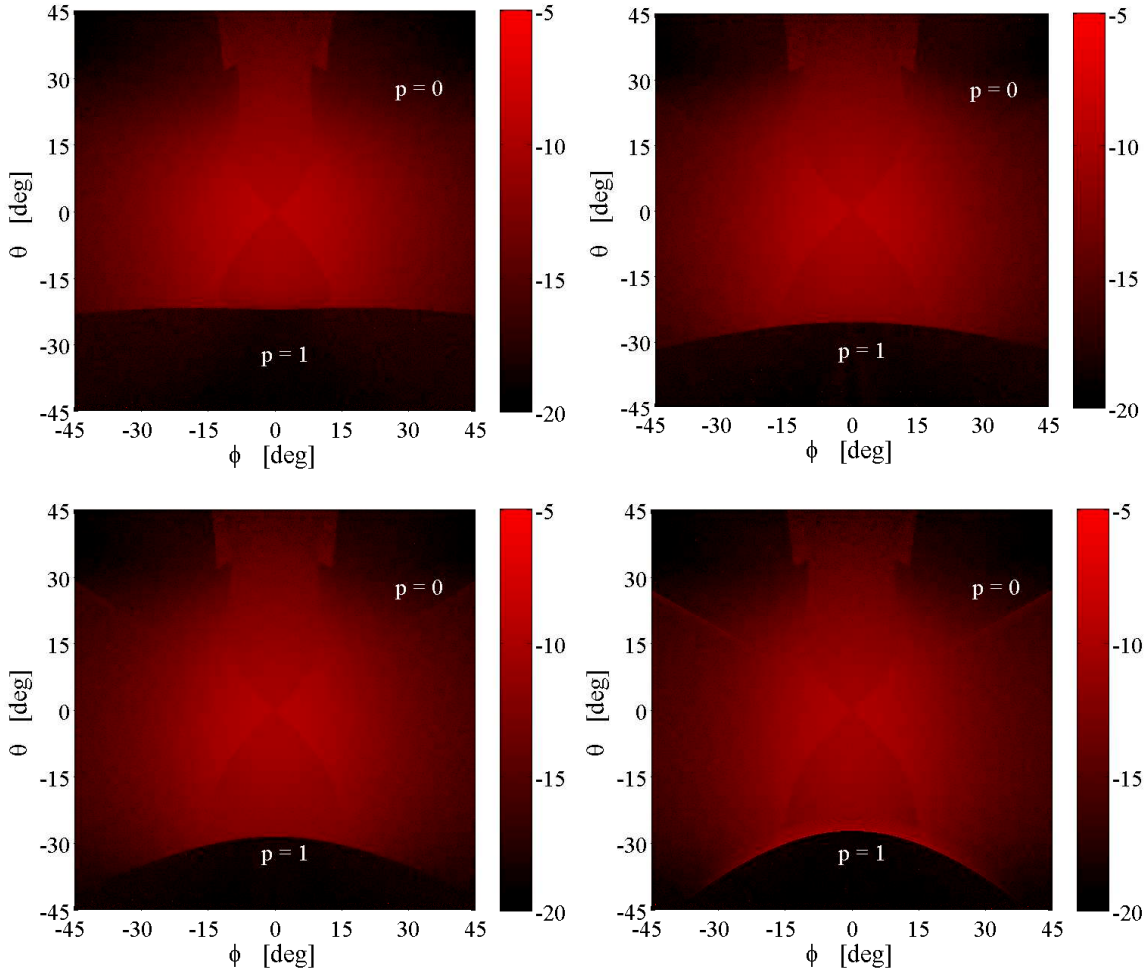

Figure 5.25: Scattering patterns **with interference** in forward direction of the 4 droplets with the parameters in Tab. 5.9.

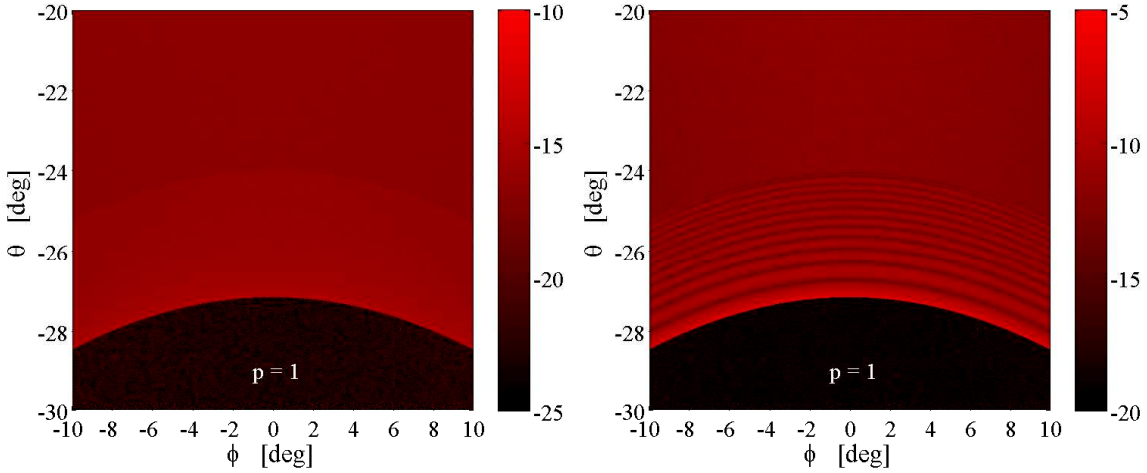

Figure 5.26: Scattering patterns **without interference** (left) and **with interference** (right) in the forward direction of the droplet **d**. The detection region is $\phi \in [-10°, 10°]$ and $\theta \in [-30°, -20°]$.

Chapter 6

Conclusions and perspectives

This thesis is devoted to the development of the Statistic Vectorial Complex Ray Model (SVCRM) to investigate the interaction of a light beam with a large particle of any shape. The simulations have been validated by comparing the results with the scattering diagram of a pendent droplet by a plane wave in three dimensions. In this chapter, the conclusions of presented work are summarized and some perspectives in further research are given.

6.1 Conclusions

The light scattering is omnipresent in our life: such as rainbow, sunset, colorful clouds, in order to explain optical phenomena in our life, we need to study the relation of targets characteristics with the properties of the scattered light. In industry, such as combustion, spray of perfume, spray in motor, in order to measure these processes accurately, optical metrology is used to retrieve the properties of the scattered light and those of the scatterers. Thus, it is very important to research the scattering of light by particles. However, the particles in industry and in our life are irregular. Therefore, it is more important to study the interaction between light/wave and irregular particles.

Various theories and models that are available for dealing with the light scattering of light by particles have been well developed in optical metrology. Geometrical Optics (GO), for example, an approximate method, deals with the interaction of light with particles when the light wavelength is much smaller than the dimension of the particles. By comparison of the scattering diagrams calculated by GO with Lorenz-Mie theory (LMT), we have shown that the GO permits to deal with the scattering of large particles (diameter larger than about 50 times the wavelength) and the precision is sufficiently good in general.

However, the formalism of GO for the scattering of a sphere can not be extended to

a non-spherical particle. For an irregularly shaped particle, the incident angle (so the refraction angle) and the curvature of the particle surface change at each interaction. The Fresnel coefficients are to be calculated at each interaction point. And especially, it is very difficult to take into account the divergence/convergence of a wave on the particle surface.

After a brief recall of the fundamentals of GO for dealing with the light scattering on a sphere, the general principle of the VRCM is presented to investigate the scattering of an irregular particle with smooth surface. VRCM introduces new properties attached to the ray, which allows to obtain the interferences in the scattering diagram. If the model is very efficient to compute the scattering diagram in 2D, the 3D extension of VRCM needs complex interpolation and the work is in progress.

In theories, the SVCRM for the scattering by a plane wave is a variant of VCRM, in which we avoid doing an 2D interpolation by using a statistical approach. In this thesis, the model has been described in details: Four coordinate basis are defined to depict the properties of the wave and the particle surface at a given interaction point; Wave front equation with curvature matrix and projection matrix indicates the relation between the wave front curvatures of the wave before and after interaction on the particle surface; The phase of a ray is calculated including initial phase of the ray and its phase shifts induced by focal lines, optical path and the Fresnel coefficients, which is the crucial factor to studying the interference phenomenon in the light scattering of a large non-spherical particle with SVCRM. The analytical expressions of the scattered intensity with and without interference in a plane wave are derived in SVCRM.

Next, the generation of the pendent droplet by experiment is introduced and some interesting scattering patterns around the rainbow angles are obtained at the same time, which are the reference to compare with the simulation results. Conclusions shows that SVCRM is valid to deal with the scattering of large irregular particles taking the interference phenomenon into consideration.

Finally, the effect of detection steps, the number of emitted photons, size of droplets as well as the incident area of photons on the scattered intensity distribution around the rainbow angle are investigated. We can conclude according to the analysis about the influencing factors of the intensity distribution: 1. For the light scattering of a droplet, the intensity distribution without interference can be used to investigate the scattering mechanism of different order rays or of different incident areas. The scattering patterns without interference around the rainbow angles is less sensitive to the number of emitted photons and the detection steps than that with interference; 2. Contrary to the intensity distribution without interference, the intensity distribution with interference has a high requirements about the number of emitted photons and the detection steps. If the detection steps are not suitable, the interference phenomenon is not obvious or even disappears although the number of emitted photons is extremely large. With a appropriate set of detection steps, the interference fringes are more clearly with a larger number of emitted photons; 3. For the scattered intensity distribution

around the rainbow angles with the same detection steps and the same number of emitted photons, the larger the particle size, the denser the interference fringes, which rises from the phase shift induced by optical path.

By the comparison of the scattering diagrams calculated by SVCRM with by experiment, we conclude that the SVCRM is valid to deal with the scattering of the large irregular particles in three dimensions, which can be used to predict the characteristics of light scattering around the rainbow angles under different conditions.

6.2 Perspectives

In this thesis, SVCRM has been developed to study the scattering of large irregular particles by a plane wave taking the interference phenomenon into consideration and the simulated scattering patterns around the rainbow angles agree well with the skeletons of the images obtained experimentally.

It is worth mentioning that simulation results in forward direction for the pendent droplet: the distributions of scattered intensity without interference for different droplets are all continuous whether it changes with θ or ϕ. However, the distributions of scattered intensity with interference for different droplets in some detection areas are discontinuous. Further effort is required to understand and better explain the scattering patterns in forward direction.

In addition, the effect of the order of ray, polarization of the plane wave and the absorption factor on the scattered intensity distribution with SVCRM remain to be explored and future work will also focus on the scattering of shaped beams by large irregular particles with SVCRM.

In fact, particle with a smooth surface and with rotational symmetry is one limitation of SVCRM. An extension of SVCRM is necessary to overcome this obstacle.

Finally, the aim is to have a model which would be able to compute interaction of light with any large transparent or low absorbing transparent structure: liquid drop, liquid jet, etc. It opens the way to make the complete simulation of the optical diagnostic on realistic liquid structure computed by CFD: light source, interaction with liquid structure, detection. By changing the liquid structure, statistical relations between detected optical signal and some characteristics of the liquid can be deduced. The same relations can then be applied on experimental configurations.

Appendices

Appendix A

Least Squares Fitting

In SVCRM, the profile of pendent droplet $r(\theta)$ is approximated by a polynomial. A least squares method is used to compute the coefficients of the polynomial.

For general case, let (θ_i, r_i) be the experimental points to be approximated by polynomial $r(\theta) = a_0 + a_1\theta + a_2\theta^2 + \cdots + a_k\theta^k$. The residual is given by

$$R^2 = \sum_{i=1}^{n} \left[r_i - \left(a_0 + a_1\theta + a_1\theta_i^2 + \cdots + a_k\theta_i^k \right) \right] \tag{A.1}$$

The partial derivatives (again dropping superscripts) are

$$\frac{\partial\left(R^2\right)}{\partial a_1} = -2\sum_{i=1}^{n} \left[r_i - \left(a_0 + a_1\theta + a_1\theta_i^2 + \cdots + a_k\theta_i^k \right) \right] = 0$$

$$\frac{\partial\left(R^2\right)}{\partial a_0} = -2\sum_{i=1}^{n} \left[r_i - \left(a_0 + a_1\theta + a_1\theta_i^2 + \cdots + a_k\theta_i^k \right) \right] \theta_i = 0$$

And so on. For coefficient a_k:

$$\frac{\partial\left(R^2\right)}{\partial a_k} = -2\sum_{i=1}^{n} \left[r_i - \left(a_0 + a_1\theta + a_1\theta_i^2 + \cdots + a_k\theta_i^k \right) \right] \theta_i^k = 0$$

which leads to the system of equations in matrix form:

$$\begin{bmatrix} n & \sum_{i=1}^{n}\theta_i & \sum_{i=1}^{n}\theta_i^2 & \cdots & \sum_{i=1}^{n}\theta_i^k \\ \sum_{i=1}^{n}\theta_i & \sum_{i=1}^{n}\theta_i^2 & \sum_{i=1}^{n}\theta_i^3 & \cdots & \sum_{i=1}^{n}\theta_i^{k+1} \\ \sum_{i=1}^{n}\theta_i^2 & \sum_{i=1}^{n}\theta_i^3 & \sum_{i=1}^{n}\theta_i^4 & \cdots & \sum_{i=1}^{n}\theta_i^{k+2} \\ \vdots & \vdots & \vdots & \vdots & \vdots \\ \sum_{i=1}^{n}\theta_i^k & \sum_{i=1}^{n}\theta_i^{k+1} & \sum_{i=1}^{n}\theta_i^{k+2} & \cdots & \sum_{i=1}^{n}\theta_i^{2k} \end{bmatrix} \begin{bmatrix} a_0 \\ a_1 \\ a_2 \\ \vdots \\ a_k \end{bmatrix} = \begin{bmatrix} \sum_{i=1}^{n} r_i \\ \sum_{i=1}^{n}\theta_i r_i \\ \sum_{i=1}^{n}\theta_i^2 r_i \\ \vdots \\ \sum_{i=1}^{n}\theta_i^k r_i \end{bmatrix}$$

In fact, the derivative of $r(\theta)$ is zero at $\theta = 0$. That is to say $r^{'}(\theta = 0) = 0$. If derivative at $x = 0$ is zero, then

$$\frac{dr}{d\theta} = a_1 + 2a_1\theta + \cdots + ka_k\theta^{k-1} = 0$$

We can deduces that $a_1 = 0$. The system of equations is then:

$$\begin{bmatrix} n & \sum_{i=1}^{n}\theta_i & \sum_{i=1}^{n}\theta_i^2 & \cdots & \sum_{i=1}^{n}\theta_i^k \\ \sum_{i=1}^{n}\theta_i^2 & \sum_{i=1}^{n}\theta_i^3 & \sum_{i=1}^{n}\theta_i^4 & \cdots & \sum_{i=1}^{n}\theta_i^{k+2} \\ \sum_{i=1}^{n}\theta_i^3 & \sum_{i=1}^{n}\theta_i^4 & \sum_{i=1}^{n}\theta_i^4 & \cdots & \sum_{i=1}^{n}\theta_i^{k+3} \\ \vdots & \vdots & \vdots & \vdots & \vdots \\ \sum_{i=1}^{n}\theta_i^k & \sum_{i=1}^{n}\theta_i^{k+1} & \sum_{i=1}^{n}\theta_i^{k+2} & \cdots & \sum_{i=1}^{n}\theta_i^{2k} \end{bmatrix} \begin{bmatrix} a_0 \\ a_2 \\ a_3 \\ \vdots \\ a_k \end{bmatrix} = \begin{bmatrix} \sum_{i=1}^{n} r_i \\ \sum_{i=1}^{n}\theta_i r_i \\ \sum_{i=1}^{n}\theta_i^2 r_i \\ \vdots \\ \sum_{i=1}^{n}\theta_i^k r_i \end{bmatrix}$$

which is solved to obtain coefficients a_0, a_2,$\cdots$, a_k.

Appendix B

Conversion of matrices

This thesis is devoted to Statistic Vectorial Complex Ray Model (SVCRM) for plane wave scattering by a pendent droplet. As given in Chapter 3, we define four normalized orthogonal bases to describe the properties of rays before and after interaction as well as the particle surface at a given interaction point. For each interaction point, the incident plane defined by the propagation vector of the incident ray and the normal to the particle surface is unique, therefore, the incident planes adjacent to each interaction point are not in the same plane. For example, the refracted ray at the first interaction point is also the incident ray at the second interaction point. The reflected ray at the second interaction point is also the incident ray at the third interaction point. Thus, it is necessary to discuss the expressions of the curvature matrix in different bases. In a word, it is a crucial operation that the mutual transformation of curvature matrices from its principal base to another base in SVCRM.

B.1 From principal base to general base

In this part, we derive the transforming function of curvature matrix from its principal base to another base at a reference point. Let $\mathbf{Q}$ be a curvature matrix defined in the reference of the principal directions $\boldsymbol{B} = (\hat{\boldsymbol{x}}_{\mathbf{1}}, \hat{\boldsymbol{x}}_{\mathbf{2}})$. It is necessarily diagonal. Let us note it

$$\mathbf{Q} = \begin{bmatrix} k_1 & 0 \\ 0 & k_2 \end{bmatrix} \tag{B.1}$$

Let $\boldsymbol{B}'$ be the basis $\boldsymbol{B}' = (\hat{\boldsymbol{x}}_{\mathbf{1}}', \hat{\boldsymbol{x}}_{\mathbf{2}}')$, whose axes are defined by :

$$\begin{aligned} \hat{\boldsymbol{x}}_{\mathbf{1}}' &= \cos\delta\hat{\boldsymbol{x}}_{\mathbf{1}} - \sin\delta\hat{\boldsymbol{x}}_{\mathbf{2}} \\ \hat{\boldsymbol{x}}_{\mathbf{2}}' &= \sin\delta\hat{\boldsymbol{x}}_{\mathbf{1}} + \cos\delta\hat{\boldsymbol{x}}_{\mathbf{2}} \end{aligned} \tag{B.2}$$

or

$$\begin{aligned} \hat{\boldsymbol{x}}_{\mathbf{1}} &= \cos\delta\hat{\boldsymbol{x}}_{\mathbf{1}}^{'} + \sin\delta\hat{\boldsymbol{x}}_{\mathbf{2}}^{'} \\ \hat{\boldsymbol{x}}_{\mathbf{2}} &= -\sin\delta\hat{\boldsymbol{x}}_{\mathbf{1}}^{'} + \cos\delta\hat{\boldsymbol{x}}_{\mathbf{2}}^{'} \end{aligned} \tag{B.3}$$

The rotation angle δ is calculated by

$$\begin{cases} \cos\delta = \hat{\boldsymbol{x}}_{\mathbf{1}} \cdot \hat{\boldsymbol{x}}_{\mathbf{1}}^{'} \\ \sin\delta = \hat{\boldsymbol{x}}_{\mathbf{1}} \cdot \hat{\boldsymbol{x}}_{\mathbf{2}}^{'} \end{cases} \tag{B.4}$$

The change of coordinates is done by:

$$\begin{aligned} x_1\hat{\boldsymbol{x}}_{\mathbf{1}} + x_2\hat{\boldsymbol{x}}_{\mathbf{2}} &= x_1\left(\cos\delta\hat{\boldsymbol{x}}_{\mathbf{1}}^{'} + \sin\delta\hat{\boldsymbol{x}}_{\mathbf{2}}^{'}\right) + x_2\left(-\sin\delta\hat{\boldsymbol{x}}_{\mathbf{1}}^{'} + \cos\delta\hat{\boldsymbol{x}}_{\mathbf{2}}^{'}\right) \\ &= \left(x_1\cos\delta - x_2\sin\delta\right)\hat{\boldsymbol{x}}_{\mathbf{1}}^{'} + \left(x_1\sin\delta + x_2\cos\delta\right)\hat{\boldsymbol{x}}_{\mathbf{2}}^{'} \\ &= x_1^{'}\hat{\boldsymbol{x}}_{\mathbf{1}}^{'} + x_2^{'}\hat{\boldsymbol{x}}_{\mathbf{2}}^{'} \end{aligned} \tag{B.5}$$

Similarly,

$$\begin{aligned} x_1^{'}\hat{\boldsymbol{x}}_{\mathbf{1}}^{'} + x_2^{'}\hat{\boldsymbol{x}}_{\mathbf{2}}^{'} &= x_1^{'}\left(\cos\delta\hat{\boldsymbol{x}}_{\mathbf{1}} - \sin\delta\hat{\boldsymbol{x}}_{\mathbf{2}}\right) + x_2^{'}\left(\sin\delta\hat{\boldsymbol{x}}_{\mathbf{1}} + \cos\delta\hat{\boldsymbol{x}}_{\mathbf{2}}\right) \\ &= \left(x_1^{'}\cos\delta + x_2^{'}\sin\delta\right)\hat{\boldsymbol{x}}_{\mathbf{1}} + \left(-x_1^{'}\sin\delta + x_2^{'}\cos\delta\right)\hat{\boldsymbol{x}}_{\mathbf{2}} \\ &= x_1\hat{\boldsymbol{x}}_{\mathbf{1}} + x_2\hat{\boldsymbol{x}}_{\mathbf{2}} \end{aligned} \tag{B.6}$$

which defines the matrix $\mathbf{P}$:

$$\begin{bmatrix} x_1 \\ x_2 \end{bmatrix}_{\boldsymbol{B}} = \begin{bmatrix} \cos\delta & \sin\delta \\ -\sin\delta & \cos\delta \end{bmatrix} \begin{bmatrix} x_1^{'} \\ x_2^{'} \end{bmatrix}_{\boldsymbol{B'}} = \mathbf{P} \begin{bmatrix} x_1^{'} \\ x_2^{'} \end{bmatrix}_{\boldsymbol{B'}} \tag{B.7}$$

In other words:

$$\mathbf{X}_{\boldsymbol{B}} = \mathbf{P}^{-\mathbf{1}}\mathbf{X}_{\boldsymbol{B'}} \tag{B.8}$$

and its inverse $\mathbf{P}^{-\mathbf{1}}$

$$\begin{bmatrix} x_1^{'} \\ x_2^{'} \end{bmatrix}_{\boldsymbol{B'}} = \begin{bmatrix} \cos\delta & -\sin\delta \\ \sin\delta & \cos\delta \end{bmatrix} \begin{bmatrix} x_1 \\ x_2 \end{bmatrix}_{\boldsymbol{B}} = \mathbf{P}^{-\mathbf{1}} \begin{bmatrix} x_1 \\ x_2 \end{bmatrix}_{\boldsymbol{B}} \tag{B.9}$$

In other words:

$$\mathbf{X}_{\boldsymbol{B'}} = \mathbf{P}^{-\mathbf{1}}\mathbf{X}_{\boldsymbol{B}} \tag{B.10}$$

Thus, the components of the electric field (E_1', E_2') are written in the basis $\boldsymbol{B'}$ as a function of their expression (E_1, E_2) in the basis $\boldsymbol{B}$:

$$\begin{cases} E_1' = \cos\delta E_1 - \sin\delta E_2 \\ E_2' = \sin\delta E_1 + \cos\delta E_2 \end{cases} \tag{B.11}$$

Moreover, the matrix $\mathbf{Q}$ of curvatures is characteristic of the linear mapping transforming the vector $\mathbf{X_B}$ and $\mathbf{Y_B}$:

$$\mathbf{Y_B} = \mathbf{Q_B X_B} \tag{B.12}$$

The same vector can be represented in basis $\boldsymbol{B'}$:

$$\mathbf{Y_B} = \mathbf{P X_{B'}} \tag{B.13}$$

and we can deduce that

$$\mathbf{P Y_{B'}} = \mathbf{Y_B} = \mathbf{Q_B X_B} = \mathbf{Q_B P X_{B'}} \tag{B.14}$$

and

$$\mathbf{Y_{B'}} = \mathbf{Q_{B'} X B'} = \mathbf{P^{-1} Q_B P X_{B'}} \tag{B.15}$$

Therefore, $\mathbf{Q_{B'}}$ can be expressed as

$$\begin{aligned} \mathbf{Q_{B'}} &= \mathbf{P^{-1} Q_B P} \\ &= \begin{bmatrix} \cos\delta & -\sin\delta \\ \sin\delta & \cos\delta \end{bmatrix} \begin{bmatrix} \kappa_1 & 0 \\ 0 & \kappa_2 \end{bmatrix} \begin{bmatrix} \cos\delta & \sin\delta \\ -\sin\delta & \cos\delta \end{bmatrix} \\ &= \begin{bmatrix} \cos\delta & -\sin\delta \\ \sin\delta & \cos\delta \end{bmatrix} \begin{bmatrix} \kappa_1\cos\delta & \kappa_1\sin\delta \\ -\kappa_2\sin\delta & \kappa_1\cos\delta \end{bmatrix} \\ &= \begin{bmatrix} \kappa_1\cos^2\delta + \kappa_2\sin^2\delta & (\kappa_1-\kappa_2)\sin\delta\cos\delta \\ (\kappa_1-\kappa_2)\sin\delta\cos\delta & \kappa_1\sin^2\delta + \kappa_2\cos^2\delta \end{bmatrix} \end{aligned} \tag{B.16}$$

That is to say that the matrix of curvatures in the basis $\boldsymbol{B'}$ is written:

$$\mathbf{Q_{B'}} = \begin{bmatrix} \kappa_1\cos^2\delta + \kappa_2\sin^2\delta & (\kappa_1-\kappa_2)\sin\delta\cos\delta \\ (\kappa_1-\kappa_2)\sin\delta\cos\delta & \kappa_1\sin^2\delta + \kappa_2\cos^2\delta \end{bmatrix} \tag{B.17}$$

In particular, if $\kappa_1^{(i)}$ and $\kappa_2^{(i)}$ are the radii of curvature of the incident photon in the proper directions $\hat{\boldsymbol{x}}_\mathbf{1}$ and $\hat{\boldsymbol{x}}_\mathbf{2}$, The curvature matrix in the incident reference frame $(\hat{\boldsymbol{e}}_\boldsymbol{i}^{(\boldsymbol{i})}, \hat{\boldsymbol{e}}_\boldsymbol{j}^{(\boldsymbol{i})}, \boldsymbol{k}^{(\boldsymbol{i})})$ is :

$$\mathbf{Q_{B'}} = \begin{bmatrix} \kappa_{ii}^{(i)} & \kappa_{ij}^{(i)} \\ \kappa_{ij}^{(i)} & \kappa_{jj}^{(i)} \end{bmatrix} \tag{B.18}$$

with

$$\begin{cases} \kappa_{ii}^{(i)} = \kappa_1^{(i)} \cos^2\delta + \kappa_2^{(i)} \sin^2\delta \\ \kappa_{jj}^{(i)} = \kappa_1^{(i)} \sin^2\delta + \kappa_2^{(i)} \cos^2\delta \\ \kappa_{ij}^{(i)} = \left(\kappa_1^{(i)} - \kappa_2^{(i)}\right) \sin\delta\cos\delta \end{cases} \tag{B.19}$$

Similarly, let $\kappa_1^{(s)}$ and $\kappa_2^{(s)}$ are the radii of curvature of the particle surface along its proper directions $\boldsymbol{x_1^{(s)}}$ and $\boldsymbol{x_2^{(s)}}$, The curvature matrix in the particle surface reference frame $(\hat{\boldsymbol{e}}_{\boldsymbol{i}}^{(\boldsymbol{s})}, \hat{\boldsymbol{e}}_{\boldsymbol{j}}^{(\boldsymbol{s})}, \boldsymbol{n})$, with $\hat{\boldsymbol{e}}_{\boldsymbol{j}}^{(\boldsymbol{s})} = \hat{\boldsymbol{e}}_{\boldsymbol{j}}^{(\boldsymbol{i})}$, and $\hat{\boldsymbol{e}}_{\boldsymbol{i}}^{(\boldsymbol{s})} = \hat{\boldsymbol{e}}_{\boldsymbol{j}}^{(\boldsymbol{s})} \times \boldsymbol{n}$. In this case,

$$\mathbf{Q}_{\boldsymbol{B'}} = \begin{bmatrix} \kappa_{ii}^{(s)} & \kappa_{ij}^{(s)} \\ \kappa_{ij}^{(s)} & \kappa_{jj}^{(s)} \end{bmatrix}. \tag{B.20}$$

with

$$\begin{cases} \kappa_{ii}^{(s)} = \kappa_1^{(s)} \cos^2\delta + \kappa_2^{(s)} \sin^2\delta \\ \kappa_{jj}^{(s)} = \kappa_1^{(s)} \sin^2\delta + \kappa_2^{(s)} \cos^2\delta \\ \kappa_{ij}^{(s)} = \left(\kappa_1^{(s)} - \kappa_2^{(s)}\right) \sin\delta\cos\delta \end{cases} \tag{B.21}$$

B.2 Diagonalization of curvature matrices

Consider the matrix $\mathbf{Q}_{\boldsymbol{B'}}$:

$$\mathbf{Q}_{\boldsymbol{B'}} = \begin{bmatrix} \kappa_{ii}^{(i)} & \kappa_{ij}^{(i)} \\ \kappa_{ij}^{(i)} & \kappa_{jj}^{(i)} \end{bmatrix}. \tag{B.22}$$

and look for the rotation matrix $\mathbf{P^{-1}}$:

$$\mathbf{P^{-1}} = \begin{bmatrix} \cos\delta & -\sin\delta \\ \sin\delta & \cos\delta \end{bmatrix}. \tag{B.23}$$

To diagonalize the matrix $\mathbf{Q}^{'}$:

$$\begin{aligned}
\mathbf{PQ_{B'}P^{-1}} &= \begin{bmatrix} \cos\delta & \sin\delta \\ -\sin\delta & \cos\delta \end{bmatrix} \begin{bmatrix} \kappa_{ii}^{(i)} & \kappa_{ij}^{(i)} \\ \kappa_{ij}^{(i)} & \kappa_{jj}^{(i)} \end{bmatrix} \begin{bmatrix} \cos\delta & -\sin\delta \\ \sin\delta & \cos\delta \end{bmatrix} \\
&= \begin{bmatrix} \cos\delta & \sin\delta \\ -\sin\delta & \cos\delta \end{bmatrix} \begin{bmatrix} \kappa_{ii}^{(i)}\cos\delta + \kappa_{ij}^{(i)}\sin\delta & -\kappa_{ii}^{(i)}\sin\delta + \kappa_{ij}^{(i)}\cos\delta \\ \kappa_{ij}^{(i)}\cos\delta + \kappa_{jj}^{(i)}\sin\delta & -\kappa_{ij}^{(i)}\sin\delta + \kappa_{jj}^{(i)}\cos\delta \end{bmatrix} \\
&= \begin{bmatrix} \kappa_{11}^{(i)} & \kappa_{12}^{(i)} \\ \kappa_{21}^{(i)} & \kappa_{22}^{(i)} \end{bmatrix} \\
&= \begin{bmatrix} \kappa_{1}^{(i)} & 0 \\ 0 & \kappa_{2}^{(i)} \end{bmatrix}
\end{aligned} \tag{B.24}$$

with

$$\kappa_{11}^{(i)} = \kappa_{ii}^{(i)}\cos^2\delta + 2\kappa_{ij}^{(i)}\sin\delta\cos\delta + \kappa_{jj}^{(i)}\sin^2\delta == \kappa_1^{(i)} \tag{B.25}$$

$$\kappa_{12}^{(i)} = (\kappa_{jj}^{(i)} - \kappa_{ii}^{(i)})\sin\delta\cos\delta + \kappa_{ij}^{(i)}(\cos^2\delta - \sin^{12}\delta) = 0 \tag{B.26}$$

$$\kappa_{22}^{(i)} = \kappa_{ii}^{(i)}\sin^2\delta - 2\kappa_{ij}^{(i)}\sin\delta\cos\delta + \kappa_{jj}^{(i)}\cos^2\delta = \kappa_2^{(i)} \tag{B.27}$$

In order to obtain the principal curvatures or directions, we need to diagonalize this matrix, and Non-diagonal components are zero for

$$\tan 2\delta = \frac{2\kappa_{ij}^{(i)}}{(\kappa_{ii}^{(i)} - \kappa_{jj}^{(i)})} \tag{B.28}$$

Then the principal curvatures are

$$\begin{cases} \kappa_1^{(i)} = \kappa_{ii}^{(i)}\cos^2\delta + 2\kappa_{ij}^{(i)}\sin\delta\cos\delta + \kappa_{jj}^{(i)}\sin^2\delta \\ \kappa_2^{(i)} = \kappa_{ii}^{(i)}\sin^2\delta - 2\kappa_{ij}^{(i)}\sin\delta\cos\delta + \kappa_{jj}^{(i)}\cos^2\delta \end{cases} \tag{B.29}$$

and the corresponding eigenvectors are:

$$\begin{cases} \hat{\boldsymbol{x}}_{\mathbf{1}} = \cos\delta\hat{\boldsymbol{x}}_{\mathbf{1}}^{'} + \sin\delta\hat{\boldsymbol{x}}_{\mathbf{2}}^{'} \\ \hat{\boldsymbol{x}}_{\mathbf{2}} = -\sin\delta\hat{\boldsymbol{x}}_{\mathbf{1}}^{'} + \cos\delta\hat{\boldsymbol{x}}_{\mathbf{2}}^{'} \end{cases} \tag{B.30}$$

Then, the components of the electric field (E_1, E_2) in the basis B can be written as $(E_1^{'}, E_2^{'})$ in the basis $B^{'}$:

$$\begin{cases} E_1 = \cos\delta E_1^{'} + \sin\delta E_2^{'} \\ E_2 = -\sin\delta E_1^{'} + \cos\delta E_2^{'} \end{cases} \tag{B.31}$$

Note: if $\kappa_{ii}^{(i)} = \kappa_{jj}^{(i)}$, then there are two possibilities:

a. $\kappa_{ij}^{(i)} = 0$, then $\kappa_1^{(i)} = \kappa_2^{(i)}$ and in this case, we are already in the principal axes of curvature.

b. $\kappa_{ij}^{(i)} \neq 0$, that is to say $\cos 2\delta = 0$. $\delta = (2k+1)\pi/4$

Bibliography

[1] Aden Meinel and Marjorie Meinel. *Sunsets, twilights, and evening skies*. CUP Archive, 1991.

[2] Gary Waldman. *Introduction to light: The physics of light, vision, and color*. Courier Corporation, 2002.

[3] H.C. van de Hulst. *Light scattering by small particles*. Dover Publications, InC. New York, 1981.

[4] Max Born and Emil Wolf. *Principles of optics: electromagnetic theory of propagation, interference, and diffraction of light*. Macmillan, 1959.

[5] Gérard Gouesbet, Bruno Maheu, and Gérard Gréhan. Light scattering from a sphere arbitrarily located in a Gaussian beam, using a Bromwich formulation. *JOSA A*, 5(9):1427–1443, 1988.

[6] D. Lebrun, S. Belaïd, C. Özkul, K. F. Ren, and G. Géhan. Enhancement of wire diameter measurements : comparison between Fraunhofer diffraction and Lorenz-Mie theory. *Optical Engineering*, 35(35):946–950, 1996.

[7] Feng Xu, Kuanfang Ren, Gérard Gouesbet, Xiaoshu Cai, and Gerard Grehan. Theoretical prediction of radiation pressure force exerted on a spheroid by an arbitrarily shaped beam. *Physical Review E*, 75(2):026613, 2007.

[8] F Onofri, G Gréhan, and G Gouesbet. Electromagnetic scattering from a multilayered sphere located in an arbitrary beam. *Applied optics*, 34(30):7113–7124, 1995.

[9] Shoji Asano and Giichi Yamamoto. Light scattering by a spheroidal particle. *Applied optics*, 14(1):29–49, 1975.

[10] James R Wait. Scattering of a plane wave from a circular dielectric cylinder at oblique incidence. *Canadian journal of physics*, 33(5):189–195, 1955.

[11] Gérard Gouesbet, Loic Mees, Gérard Gréhan, and Kuan-Fang Ren. Localized approximation for gaussian beams in elliptical cylinder coordinates. *Applied optics*, 39(6):1008–1025, 2000.

[12] Charles L Adler, James A Lock, Justin K Nash, and Kirk W Saunders. Experimental observation of rainbow scattering by a coated cylinder: twin primary rainbows and thin-film interference. *Applied optics*, 40(9):1548–1558, 2001.

[13] KF Ren, G Gréhan, and G Gouesbet. Scattering of a Gaussian beam by an infinite cylinder in the framework of generalized Lorenz–Mie theory: formulation and numerical results. *JOSA A*, 14(11):3014–3025, 1997.

[14] Peter C Waterman. Symmetry, unitarity, and geometry in electromagnetic scattering. *Physical review D*, 3(4):825, 1971.

[15] Michael I Mishchenko, Larry D Travis, and Daniel W Mackowski. T-matrix method and its applications to electromagnetic scattering by particles: A current perspective. *Journal of Quantitative Spectroscopy and Radiative Transfer*, 111(11):1700–1703, 2010.

[16] Torleif Martin. T-matrix method for closely adjacent obstacles. *Journal of Quantitative Spectroscopy and Radiative Transfer*, 2019.

[17] Elizabeth Metzler-Winslow, Geoffrey Bryden, and Neal Turner. Using the T-matrix method to quantify solar radiation forces on interplanetary dust grains. In *American Astronomical Society Meeting Abstracts# 233*, volume 233, 2019.

[18] Bruce T Draine. The discrete-dipole approximation and its application to interstellar graphite grains. *The Astrophysical Journal*, 333:848–872, 1988.

[19] Bruce T Draine and Piotr J Flatau. Discrete-dipole approximation for scattering calculations. *JOSA A*, 11(4):1491–1499, 1994.

[20] Maxim A Yurkin and Alfons G Hoekstra. The discrete dipole approximation: an overview and recent developments. *Journal of Quantitative Spectroscopy and Radiative Transfer*, 106(1-3):558–589, 2007.

[21] Kane Yee. Numerical solution of initial boundary value problems involving Maxwell's equations in isotropic media. *IEEE Transactions on antennas and propagation*, 14(3):302–307, 1966.

[22] Allen Taflove and Susan C Hagness. *Computational electrodynamics: the finite-difference time-domain method*. Artech house, 2005.

[23] Karl S Kunz and Raymond J Luebbers. *The finite difference time domain method for electromagnetics*. CRC press, 1993.

[24] Maxim A Yurkin and Alfons G Hoekstra. The discrete-dipole-approximation code ADDA: capabilities and known limitations. *Journal of Quantitative Spectroscopy and Radiative Transfer*, 112(13):2234–2247, 2011.

[25] Lord Rayleigh. V. On the incidence of aerial and electric waves upon small obstacles in the form of ellipsoids or elliptic cylinders, and on the passage of electric waves through a circular aperture in a conducting screen. *The London, Edinburgh, and Dublin Philosophical Magazine and Journal of Science*, 44(266):28–52, 1897.

[26] T Čižmár, M Šiler, and P Zemánek. An optical nanotrap array movable over a milimetre range. *Applied Physics B*, 84(1-2):197–203, 2006.

[27] HC Van de Hulst. Light Scattering by Small Particle, new york: John wiley & sons. *Inc.*, pages 114–130, 1957.

[28] Feng Xu, Kuan Fang Ren, and Xiaoshu Cai. Extension of geometrical-optics approximation to on-axis Gaussian beam scattering. I. by a spherical particle. *Applied optics*, 45(20):4990–4999, 2006.

[29] Feng Xu, Kuan Fang Ren, Xiaoshu Cai, and Jianqi Shen. Extension of geometrical-optics approximation to on-axis Gaussian beam scattering. II. by a spheroidal particle with end-on incidence. *Applied optics*, 45(20):5000–5009, 2006.

[30] Haitao Yu, Jianqi Shen, and Yuehuan Wei. Geometrical optics approximation of light scattering by large air bubbles. *Particuology*, 6(5):340–346, 2008.

[31] Edward A Hovenac and James A Lock. Assessing the contributions of surface waves and complex rays to far-field Mie scattering by use of the Debye series. *JOSA A*, 9(5):781–795, 1992.

[32] Haitao Yu, Jianqi Shen, and Yuehuan Wei. Geometrical optics approximation for light scattering by absorbing spherical particles. *Journal of Quantitative Spectroscopy and Radiative Transfer*, 110(13):1178–1189, 2009.

[33] Xiangzhen Li and Xiang'e Han. Computation of on-axis Gaussian beam scattering by nonuniform glass microbeads using a geometrical-optics approach. *Journal of Optics A: Pure and Applied Optics*, 11(10):105703, 2009.

[34] Karri Muinonen, T Nousiainen, P Fast, Kari Lumme, and JI Peltoniemi. Light scattering by Gaussian random particles: ray optics approximation. *Journal of Quantitative Spectroscopy and Radiative Transfer*, 55(5):577–601, 1996.

[35] ES Grin'ko and Yu G Shkuratov. The scattering matrix of transparent particles of random shape in the geometrical optics approximation. *Optics and Spectroscopy*, 93(6):885–893, 2002.

[36] K. F. Ren, F. Onofri, C. Rozé, and T. Girasole. Vectorial complex ray model and application to two-dimensional scattering of plane wave by a spheroidal particle. *Optics letters*, 36(3):370–372, 2011.

[37] Kuan Fang Ren and Claude Rozé. Vectorial complex ray model for light scattering of nonspherical particles, 2018.

[38] Keli Jiang. *Theoretical study of light scattering by an elliptical cylinder*. PhD thesis, Texas A&M University, USA, 2013., 2013.

[39] M. Yang, Y. Wu, X. Sheng, and K. F. Ren. Comparison of scattering diagrams of large non-spherical particles calculated by VCRM and MLFMA. *Journal of Quantitative Spectroscopy and Radiative Transfer*, 162:143–153, 2015.

[40] Fabrice RA Onofri, Kuan Fang Ren, Matthias Sentis, Quentin Gaubert, and Chantal Pelcé. Experimental validation of the vectorial complex ray model on the intercaustics scattering of oblate droplets. *Optics express*, 23(12):15768–15773, 2015.

[41] Ruiping Yang, Claude Rozé, Saïd Idlahcen, and Kuan Fang Ren. Simulation of light scattering by a pendent drop with statistic vectorial complex ray model. *Sensors & Transducers*, 226(10):71–76, 2018.

[42] AV Shavlov, VA Dzhumandzhi, and AA Yakovenko. Charge of water droplets during evaporation and condensation. *Journal of Aerosol Science*, 123:17–26, 2018.

[43] Hadi Mohammadjafari Sadeghi, Behnam Sadri, Mohammad Amin Kazemi, and Moharram Jafari. Coalescence of charged droplets in outer fluids. *Journal of Colloid and Interface Science*, 532:S002197971830907X–, 2018.

[44] S. Faraji, B. Sadri, B. Vajdi Hokmabad, N. Jadidoleslam, and E. Esmaeilzadeh. Experimental study on the role of electrical conductivity in pulsating modes of electrospraying. *Experimental Thermal & Fluid Science*, 81:327–335, 2017.

[45] Arnold Frohn and Norbert Roth. *Dynamics of droplets*. Springer Science & Business Media, 2013.

[46] R. S. Volkov, G. V. Kuznetsov, and P. A. Strizhak. Temperature and velocity fields of the gas-vapor flow near evaporating water droplets. *International Journal of Thermal Sciences*, 134:337–354, 2018.

[47] Manuel Auliano, Carlos Dorao, Maria Fernandino, and Zhang Peng. Water droplet impacting on overheated random Si nanowires. *International Journal of Heat & Mass Transfer*, 124:307–318, 2018.

[48] N. Hatta, H. Fujimoto, and T. Yokotani. Collision dynamics of a water droplet impinging on a hot solid surface. *Steel Research*, 69(10):429–437, 1998.

[49] Bong June Zhang, Kwang Jin Kim, and Young Lee Chi. Behavior of an evaporating water droplet on lubricant-impregnated nano-structured surface. *Experimental Thermal & Fluid Science*, 96:S089417771830311X, 2018.

[50] Jean C. Legros and Maxim V. Piskunov. Evaporation of water droplets with metallic inclusions. *International Journal of Multiphase Flow*, 102:S0301932217301854, 2018.

[51] Yina Yao, Li Cong, Zhenxiang Tao, Yang Rui, and Zhang Hui. Experimental and numerical study on the impact and freezing process of a water droplet on a cold surface. *Applied Thermal Engineering*, 137, 2018.

[52] P. A. Strizhak, R. S. Volkov, G. Castanet, F. Lemoine, and S. S. Sazhin. Heating and evaporation of suspended water droplets: Experimental studies and modelling. *International Journal of Heat and Mass Transfer*, 127:92–106, 2018.

[53] M. Born and E. Wolf. *Principles of optics, 7th ed.* Cambridge University Press, 1999. Pergamon Press, 3rd edition.

[54] KF Ren, C Rozé, and T Girasole. Scattering and transversal divergence of an ellipsoidal particle by using vectorial complex ray model. *Journal of Quantitative Spectroscopy and Radiative Transfer*, 113(18):2419–2423, 2012.

[55] Kuan Fang Ren, Keli Jiang, et al. Scattering of an arbitrary shaped object by using vectorial complex ray model. In *ISAPE2012*, pages 837–841. IEEE, 2012.

[56] Georges A Deschamps. Ray techniques in electromagnetics. *Proceedings of the IEEE*, 60(9):1022–1035, 1972.

[57] Keli Jiang, Xiang'e Han, and Kuan Fang Ren. Scattering of a gaussian beam by an elliptical cylinder using the vectorial complex ray model. *JOSA A*, 30(8):1548–1556, 2013.

[58] Sergey Y Yurish. *Advances in Optics Reviews 1.* Lulu. com, 2018.

[59] Zelong Ma. *Extension of vectorial complex ray model and its application to the metrology of non-spherical particles.* PhD thesis, Rouen university, 2018.

[60] ALLEAUME Romain. Etude expérimentale de diffusion de la lumière par une goutte suspendue. Technical report, CORIA, Département Optique et Lasers, 2017.

[61] ABDEDDAIM Driss. Etude du modèle de diffusion d'une goutte suspendue par mesure laser. Technical report, Ingénieur CNRS, ESITech - Université de Rouen, 2016.

[62] S. Idlahcen F. Ren, C. Roze and Z. Ma. Observation of exotic scattering patterns of suspended droplets and their theoretical prediction by vectorial complex ray model. In *ILASS – Europe 2016, 27th Annual Conference on Liquid Atomization and Spray Systems, Brighton (United Kingdom), 4-7 Sep.*, 2016.

[63] https://faculty.math.illinois.edu/ kapovich/423-14/surfacesofrevolution.pdf.

Résumé

Cette thèse est consacrée à la simulation numérique tridimensionnelle de la diffusion d'une onde plane par une gouttelette pendante à l'aide d'un modèle de Tracé de Rayons Vectoriels Complexes Statistiques (TRVCS), basé sur modèle de Tracé de Rayons Vectoriels Complexes (TRVC)précédemment mis au point par le laboratoire CORIA.

La métrologie optique est largement utilisée dans de nombreux domaines de la recherche scientifique et non intrusive. De nombreuses techniques de mesure ont été développées pour caractériser la taille, la température, ... des particules. Mais la plupart d'entre elles sont limitées aux particules de forme simple en raison de l'absence d'outils théorique ou numérique permettant de prédire la relation entre la lumière diffusée et les propriétés des diffuseurs, en particulier pour les grosses particules non sphériques.

Pour surmonter cet obstacle, TRVC a été développé. Dans ce modèle, la *courbe du front d'onde* est introduite comme une nouvelle propriété des rayons lumineux. La divergence et la convergence d'une onde sur la surface courbée de la particule peuvent être facilement prédites par l'équation du front d'onde. Ainsi, il peut être appliqué à la diffusion de la lumière par de grosses particules de forme quelconque et de surface lisse. La TRVC a été validée expérimentalement et numériquement dans les cas de diffusion dans un plan de diffusion symétrique. Afin de contourner le problème de l'interpolation 2D avec des données irrégulières, nous proposons un modèle de TRVCS. Mais le phénomène d'interférence n'est pas pris en compte dans sa version initiale.

Dans cette thèse, la méthode de calcul de la phase due au chemin optique, aux coefficients de Fresnel et aux lignes focales sont soigneusement étudiés pour une particule non sphérique dans le cadre de TRVCS. Il est ensuite appliqué à la simulation de la diffusion en trois dimensions d'une gouttelette pendante. Les figures de diffusion aux alentour des arcs-en-ciel du premier et du second ordres, dans la direction avant, sont simulées pour quatre formes typiques de gouttelettes pendantes obtenues expérimentalement. Les résultats numériques sont en bon accord avec les résultats expérimentaux. Le mécanisme de diffusion et la contribution de différents ordres de rayons sont également étudiés.

Mots-clés: diffusion de lumière, particule non-sphérique, optique géométrique, Tracé de Rayons Vectoriels Complexes, Tracé de Rayons Vectoriels Complexes Statistiques, goutte pendante

Abstract

This thesis is devoted to the numerical simulation of the scattering of plane wave by a pendent droplet in three dimensions using the Statistic Vectorial Complex Ray Model(SVCRM), which is based on the Vectorial Complex Ray Model (VCRM) developed in the laboratory CORIA.

Optical metrology is widely used in many domains of scientific research due to its advantages of being fast and non-intrusive. Numerous measurement techniques have been developed to characterize the size, the temperature, ... of the particles. But most of them are limited to the particles of simples shape because of the lack of theoretical model to predict the relation of the scattered light with the properties of the scatterers, especially for the large non-spherical particle.

To overcome this obstacle, the Vectorial Complex Ray Model (VCRM) has been developed. In this model, the *wave front curvature* is introduced as a new property of light rays. The divergence and the convergence of a wave on the curved surface of the particle can be described easily by the wave front equation. So it can be applied to the scattering of light by large particles of any shape with smooth surface. The VCRM has been validated experimentally and numerically in the cases of scattering in a symmetric plane of scatterer. In order to get over the problem of 2D interpolation with irregular data, Statistic Vectorial Complex Ray Model (SVCRM) is proposed. But the interference phenomena is not considered in its initial version.

In this thesis, the method to count the phase due to the optical path, the Fresnel coefficients and the focal liens are carefully studied for a non-spherical particle in the framework of SVCRM. It is then applied to the simulation of the three dimension scattering of a pendent droplet. The scattering patterns around the first and the second order rainbows, in the forward direction are exampled for four typical shapes of pendent droplets obtained experimentally. The results are found in good agreement with experimental scattering patterns. The scattering mechanism and the contribution of different orders of rays are also investigated.

Keywords: light scattering, non-spherical particles, geometrical optics, Vectorial Complex Ray Model, Statistic Vectorial Complex Ray Model, pendent droplet